

PERCEPTUAL DRIVEN APPROACH TO THE DESIGN OF STATICALLY FOVEATED
HEAD-MOUNTED DISPLAYS

by

Pengyinjie Lyu

Copyright © Pengyinjie Lyu 2023

A Dissertation Submitted to the Faculty of the

JAMES C. WYANT COLLEGE OF OPTICAL SCIENCES

In Partial Fulfillment of the Requirements

For the Degree of

DOCTOR OF PHILOSOPHY

In the Graduate College

THE UNIVERSITY OF ARIZONA

2023

THE UNIVERSITY OF ARIZONA
GRADUATE COLLEGE

As members of the Dissertation Committee, we certify that we have read the dissertation prepared by Pengyinjie Lyu, titled *Perceptual Driven Approach to the Design of Statically Foveated Head-Mounted Displays* and recommend that it be accepted as fulfilling the dissertation requirement for the Degree of Doctor of Philosophy.

/Hong Hua/

Professor Hong Hua

Date: Jul 17, 2023

Yuzuru Takashima

Yuzuru Takashima (Jul 17, 2023 10:12 PDT)

Professor Yuzuru Takashima

Date: Jul 17, 2023

John Koshel

John Koshel (Jul 17, 2023 09:49 PDT)

Professor R. John Koshel

Date: Jul 17, 2023

Final approval and acceptance of this dissertation is contingent upon the candidate's submission of the final copies of the dissertation to the Graduate College.

I hereby certify that I have read this dissertation prepared under my direction and recommend that it be accepted as fulfilling the dissertation requirement.

/Hong Hua/

Hong Hua (Jul 25, 2023 20:54 PDT)

Professor Hong Hua

Dissertation Committee Chair

Wyant College of Optical Sciences

Date: Jul 25, 2023

ACKNOWLEDGEMENTS

I am immensely grateful to my mentor and PhD advisor, Dr. Hong Hua. Your unwavering belief in me, especially during my transition from a physics background to optical engineering, has been truly invaluable. I am thankful for the opportunities, support, and structure you provided, which were crucial in achieving my lifelong dream. Your patience and guidance throughout my PhD journey have been instrumental in shaping my growth and success. I extend my sincere gratitude to my esteemed dissertation committee members, Dr. R. John Koshel, and Dr. Yuzuru Takashima. Their expertise and experience have been invaluable to me throughout this journey. I am grateful for their time, dedication, and invaluable contributions to the development of this work.

I would also like to express my heartfelt appreciation to all my lab colleagues. Sang Yoon Lee, Hekun Huang, Miaomiao Xu, Mohan Xu, Xuan Wang, Elliott Kwan, Jeremy Katz, Austin Wilson, Yanzhao Lu, Cheng-Ting Huang, Alisha Whitehead, Feiyi Shen, and Sihan Wu, your support and collaboration have been indispensable. The exchange of ideas, the camaraderie, and the collective effort we have shared have made this journey both enriching and enjoyable.

Additionally, I would like to acknowledge the support and encouragement I have received from other friends and colleagues who have played a part in my academic achievements. Your presence, discussions, and friendship have provided a nurturing and stimulating environment that has positively impacted my research and personal growth.

DEDICATION

To my wife Yanan Li, mom Fujun Yin, and dad Ping Lyu for their love and support.

You are the light shining and warm,
refracted on my transparent soul,
infusing my life with a radiant hue.

TABLE OF CONTENTS

LIST OF FIGURES	8
LIST OF TABLES	12
ABSTRACT.....	13
1. INTRODUCTION.....	15
1.1 DISSERTATION CONTRIBUTION	16
1.2 DISSERTATION CONTENTS	17
2. BACKGROUND.....	19
2.1 TRADE-OFF BETWEEN RESOLUTION AND FOV IN HMDS	19
2.2 HUMAN VISUAL SYSTEM	20
2.3 FOVEATION TECHNOLOGY	24
2.3.1 Categorization of foveation techniques	24
2.3.2 Limits of dynamic foveation method.....	27
3. PERCEPTUAL DRIVEN APPROACH TO STATICALLY FOVEATED HMDS.....	28
3.1 PERCEPTUAL DRIVEN APPROACH OVERVIEW.....	28
3.2 PERFORMANCES METRICS.....	31
3.3 OPTIMIZATION	34
3.3.1 Optimization process	34
3.3.2 Optimization variables.....	35
3.3.3 Example of foveation scheme.....	36
3.3.4 Discussions of the selected foveation scheme	37
3.4 EXPERIMENTAL VERIFICATION	43
3.4.1 Objective assessment and validation	44
3.4.2 Quantitative assessment and validation.....	49
4. DESIGN OF A STATICALLY FOVEATED IMMERSIVE HMD.....	52
4.1 SYSTEM OVERVIEW.....	52
4.2 OPTIMIZATION METHOD	54
4.3 PERFORMANCE ANALYSIS.....	56

4.3.1 Normal performance analysis	56
4.3.2 Perceived performance assessment through a reversed system integrated with Arizona eye model.....	57
4.3.3 Resolution distribution map.....	61
4.3.4 Tolerance analysis	63
4.4 PROTOTYPE AND PERFORMANCE EVALUATION.....	64
5. STATICALLY FOVEATED FREEFORM OST-HMD SYSTEM WITH LARGE FOV....	70
5.1 SYSTEM OVERVIEW.....	70
5.2 DESIGN AND OPTIMIZATION.....	74
5.2.1 Structure constraints	76
5.2.2 TIR condition.....	78
5.2.3 Field sample.....	79
5.2.4 Constraints for spatially varying optical power control	81
5.3 Performance evaluation.....	84
5.3.1 MTF analysis	85
5.3.2 Perceived performance with Arizona eye model.....	89
5.3.3 Distortion grid and resolution distribution map	93
5.3.4 Optical see-through path performance	94
5.4 TOLERANCE ANALYSIS	96
5.5 OPTO-MECHANICAL DESIGN.....	101
6. CONCLUSION AND FUTURE WORK.....	103
6.1 DISCUSSION	103
6.2 CONCLUSION.....	105
6.3 FUTURE WORK	106
REFERENCES	107
APPENDIX A: PERCEPTUAL-DRIVEN APPROACH TO STATICALLY FOVEATED HEAD-MOUNTED DISPLAYS	113
APPENDIX B: DESIGN OF A STATICALLY FOVEATED DISPLAY BASED ON PERCEPTUAL-DRIVEN APPROACH	139
APPENDIX C: MATLAB© CODE FOR GENERATING THE FOVEATED IMAGE BY GAUSSIAN-TYPE FILTER	154

APPENDIX D: CODEV MACRO USED FOR OPTIMIZATION OF THE FOVEATED OST-HMD	159
APPENDIX E: SURFACES' GLOBAL COORDINATE DATA AND PARAMETERS FOR FOVEATED FREEFORM OST-HMD	166

LIST OF FIGURES

Fig. 2.1 (a) The schematic illustration of a display in visual space; (b) the VA of HVS as a function of eccentricity angle.....	22
Fig. 2.2 (a) Simulated perceived image of processed Briggs Target pattern when human eye gazed at 0-degree field angle; (b) zoomed in views corresponding the field angles of 10, 30, 50, and 80 degrees, respectively. (c) Simulated perceived image of processed Briggs Target pattern when human eye gazed at 30-degree field angle; (d) zoomed in views corresponding the field angles of 10, 30, 50, and 80 degrees.	23
Fig. 3.1 (a) The schematic illustration of a continuously foveated display where its angular resolution varies as a function of the field angle θ and symmetric about the display center I; (b) Example of an angular resolution distribution function along a given direction crossing the display center I as a function of the field angle.	30
Fig. 3.2 Illustration of the perceived resolution of a foveated display with its resolution distribution function in the form of a simple Gaussian function while the eye is gazed in the direction of 40° away from the display center.	32
Fig. 3.3 Overall flowchart schematic of the optimization process.	35
Fig. 3.4 Resolution distribution for three different foveation schemes: proposed three-segment continuous foveation scheme defined by Eq. (9), a 10° dual-resolution scheme, and a 30° dual-resolution scheme.....	38
Fig. 3.5 The perceived visual acuity of three different foveation schemes shown in Fig. 3.4 as a function of field angles for the eye gaze angle of (a) 10° , (b) 20° , (c) 30° , and (d) 40° , respectively.	40
Fig. 3.6 The comparison of (a) the perceived maximum resolution and (b) volume ratio of the three foveation schemes shown in Fig. 3.4 as a function of eye gaze angles.	41
Fig. 3.7 (a) The comparison of data sampling efficiency as a function of the overall FOV for three different foveation schemes shown in Fig. 3.4; (b) The comparison of total pixel number required in a diagonal direction as a function of the overall FOV among the three foveation schemes shown in Fig. 3.4 and a single-resolution display.	42
Fig. 3.8 (a) Examples of four captured zoomed-in images corresponding to 10° , 30° , 50° , and 80° field angles; (b) effective pixel density distribution for the foveated display setup as a function of field angles.	44
Fig. 3.9 (a) Captured image of original 4K Briggs Target pattern by camera; (b) zoomed in views corresponding the viewing angle of 10, 30, 50, and 80 degrees.	45
Fig. 3.10 (a) Captured image of processed Briggs Target pattern by camera; (b) zoomed in views corresponding the viewing angle of 10, 30, 50, and 80 degrees; (c) 4 rendered images of the same	

local areas perceived by a standard observer with the eye rotated at the angles of 15, 30, 30, and 30 degrees.	47
Fig. 3.11 (a) Captured image of a foveated scene with four marked regions of interests, corresponding to 10°, 30°, 50°, and 80° fields; (b) zoomed-in images of the four marked regions captured with the original full-resolution image displayed on the monitor; (c) zoomed-in images of the four marked regions captured with the statically foveated image displayed on the monitor; (d)-(f) perceived images of the four marked regions by a 20/20 standard observer, simulated from the captured zoom-in full-resolution image for the eye gaze angle of 0°, 15°, and 30°, respectively.	48
Fig. 3.12 (a) MTF curves of foveated display in horizontal direction as a function of spatial frequencies in cycles/degree for 13 different field angles; (b) The resolution distribution of the foveated display measured in the horizontal and vertical directions.	50
Fig. 3.13 Quantitative assessment of the perceived resolution distributions as a function of field angles for four different viewing angles, 10°, 20°, 30° and 40°.	51
Fig. 4.1 The required pixel number of a foveated display as a function of the overall FOV in a given direction for three different peak resolutions of 1, 1.5, and 2 arcminutes per pixel, respectively.	53
Fig. 4.2 The layout of eyepiece for the statically foveated display.	56
Fig. 4.3 MTF plots for different eye position with 4-mm pupil size. (a) MTF plot when eye is located in the center of the eyebox. (b) MTF plot when human eye moves up 2 mm. (c) MTF plot when human eye moves down 2 mm.	57
Fig. 4.4 The layout of the reserved system with Arizona eye model: (a) eye gaze at 0°; and (b) eye gaze at 30°.	58
Fig. 4.5 MTF plots for various fields with the rotation angle of Arizona eye model part: (a) 0°; (b) 10°; (c) 20°; (d) 30°.	60
Fig. 4.6 The resolution distributions of the foveated display as the function of the field angle with the eye rotation angle of (a) 0°; (b) 10°; (c) 20°; (d) 30°, respectively.	61
Fig. 4.7 (a) The distortion grid of designed foveated display; (b) The resolution distribution in field map; (c) the resolution distribution of designed foveated display and a target foveation scheme as the function of the field along the diagonal direction; (d) the pixel number in diagonal direction as a function of the FOV for designed foveated display.	62
Fig. 4.8 The foveated display MTF tolerancing results at Nyquist frequency with 4-mm eye pupil size (a) when eye locates in center of eyebox; (b) when human eye moves up 2 mm; (c) when human eye moves down 2 mm.	64
Fig. 4.9 The schematic diagram of mount design for the design eyepiece.	65
Fig. 4.10 (a) Prototype of the static foveated display with cellphone display panel; (b) The input image displayed on the cellphone screen; (c) Zoomed sub-image for the modified USAF target.	66

Fig. 4.11 (a) Captured image by 2K camera with 8-mm focal length camera lens; Captured image by 2K camera with 50-mm focal length camera lens when the camera was towards (b) 0°, (c) -20°, and (d) -35° of the field angle of display, respectively.	67
Fig. 4.12 (a) Prototype of the static foveated display with transparent high-resolution target; (b) The captured image of high-resolution target for straight view direction.	68
Fig. 4.13 (a) MTF curves of foveated display in horizontal direction as a function of spatial frequencies in cycles/degree for 9 different field angles; (b) The resolution distribution of the foveated display measured in the horizontal direction.	69
Fig. 5.1 The schematic diagram of foveated OST-HMD for the statically foveated. The first auxiliary freeform prism is composed of S1 and S2, the main freeform prism is composed of S3, S4, S3', and S5, and the second auxiliary freeform prism is composed of S4' and S6.	74
Fig. 5.2 Optical paths of upper and lower marginal rays of maximum and minimum Y-direction field.	78
Fig. 5.3 The schematic diagram of field sampling distribution by circular grid.	81
Fig. 5.4 The YOZ plane and XOZ plane layout of virtual image optical path of statically foveated freeform OST-HMD.	85
Fig. 5.5 The MTF plots of virtual image optical path of statically foveated freeform OST-HMD for (a) fovea region, (b) parafovea region, and (c) peripheral region, respectively.....	87
Fig. 5.6 The MTF box plots of virtual image optical path of statically foveated freeform OST-HMD.	88
Fig. 5.7 The MTF plots of virtual image optical path of statically foveated freeform OST-HMD with 4-mm exit pupil mimic as human eye when the pupil is (a) at center, (b) moved 2 mm along +y direction, (c) -y direction and (d) +x direction, respectively.....	89
Fig. 5.8 The layout of the reserved system with Arizona eye model: (a) eye gaze at 0°; and (b) eye gaze at 30°.	90
Fig. 5.9 MTF plots for various fields with the rotation angle of Arizona eye model part: (a) 0°; (b) 10°; (c) 20°; (d) 30°.	91
Fig. 5.10 The resolution distributions of the foveated display as the function of the field angle with the eye rotation angle of (a) 0°; (b) 10°; (c) 20°; (d) 30° along diagonal direction, respectively.	92
Fig. 5.11 (a) The distortion grid of designed foveated display; (b) The resolution distribution in field map; (c) the resolution distribution of designed foveated display as the function of the field along the diagonal direction.....	94
Fig 5.12 The YOZ plane and XOZ plane layout of optical see-through path of statically foveated freeform OST-HMD.	95
Fig. 5.13 (a) The MTF plot and (b) the distortion grid of optical see-through path of statically foveated freeform OST-HMD.....	96

Fig. 5.14 The schematic diagram random surface deformations generated with MATLAB.	97
Fig. 5.15 Cumulative probability change of polychromatic MTF at 80% of Nyquist frequency of 21.6cycles/mm with 4-mm exit pupil.	99
Fig. 5.16 Cumulative probability change of monochromatic MTF at 80% of Nyquist frequency of 21.6cycles/mm with 4-mm exit pupil.	100
Fig. 5.17 (a) Mounting of the statically foveated freeform OST-HMD; (b) Exploded view of it.	102

LIST OF TABLES

Table 4.1 The specification of the foveated display.	54
Table 4.2 Tolerance items.	63
Table 4.3 Stock lenses data.	64
Table 4.4 Aspherical lenses data.	65
Table 5.1 The overall specifications of the system.	71
Table. 5.2 The sampling field distribution.	79
Table 5.3 Tolerance items.	97
Table 5.4 Monte Carlo tolerance analysis results I.	99
Table 5.5 Monte Carlo tolerance analysis results II.	100

ABSTRACT

Head-mounted display (HMD) technology is developing very rapidly and has been applied in a variety of applications, however it suffered from the inherent trade-off between large field of view (FOV) and high resolution. Foveated display technology has emerged as a promising solution to address this trade-off through allocating the limiting resources differently between the region of interest (ROI) and the peripheral region. Previous works have primarily focused on dual-resolution dynamic foveation schemes, which are complex and bulky due to the requirement of multiple displays, multiple optical paths, a 2D steering mechanism, and eye tracking devices.

In this dissertation, we present a novel perceptual-driven approach to the design of a statically foveated display, taking inspiration from the characteristics of human eye and head movement mechanisms. Our approach aims to provide minimal or imperceptible degradation of perceived image resolution within regions of frequent eye movements across a wide FOV, eliminating the need for eye-tracking devices and scanning mechanisms. We detailly depicted the general approach to developing the statically foveation scheme and discussed the associated performance metrics for optimization. Building upon this approach, we designed a statically foveated immersive display by carefully controlling the spatial variation of the optical power in the eyepiece system which covers an 80-degree FOV and achieves a peak resolution of 1.5 arcminutes per pixel through a display panel of 1820 by 1820 pixels. Furthermore, we established a novel method to evaluate the perceived performance and constructed a prototype that demonstrates excellent perceived performance of the display. Finally, we applied this method to design a statically foveated optical see-through (OST) optical system with three wedge-shaped freeform prisms. This system achieves

a diagonally measured FOV of approximately 80 degrees for virtual view and a peak resolution of 2 arcminutes per pixel through a display panel of 1920 by 1230 pixels. Additionally, the sandwich structure of prism group ensures an undistorted see-through view and offers vision correction capabilities.

1. INTRODUCTION

Since Ivan Sutherland's demonstration of the first graphics-driven head-mounted display (HMD) in the 1960s [1], HMD technology for virtual reality (VR) and augmented reality (AR) has experienced explosive growth, especially in the last decade, and been applied to various fields including training, education, healthcare, social communication, and entertainment [2–5]. However, the majority of HMD designs adopt the well-established rectilinear sampling method in which a limited count of pixels are spread uniformly across the full field of view (FOV), so they are restricted by the inherent trade-off between their FOV and spatial resolution. For a given number of available pixels, the larger is the FOV, the lower the angular resolution. To mitigate this trade-off, efforts have been made to develop higher-resolution display technologies to increase the pixel counts. For instance, Vieri C. et al designed and fabricated a 1443 pixels per inch (ppi) organic light-emitting diode (OLED) display for VR application [6]. Liu Z. et al reviewed the latest progress regarding the implementation of micron-light-emitting diodes (μ -LED) and quantum dot (QD) in display technology [7]. QD-based μ -LED displays make a strong appeal to 8K ultra-HD displays for AR/VR displays. However, mass production remains challenging. Another approach explored for designing uniform-resolution HMDs with large FOV and high resolution is optical tiling [8–10]. However, multiple displays and optical paths are required and noticeable artifacts at the stitched regions is inevitable.

A more desirable methodology to address the trade-off between resolution and FOV is foveation technology, which draws inspiration from the foveation properties of the human visual system (HVS). This technology focuses on allocating limited resources preferentially to a user's

region of interest (ROI) while providing lower resolution in the peripheral areas outside the ROI. Prior to our proposed method, the common method was based on a dual-resolution foveation scheme, in which a foveated region with high-resolution imagery dynamically follows the user's gaze direction steered by a 2D scanner, while the peripheral view offers a lower resolution for a sense of immersion. However, this approach resulted in systems that are inevitably complex, costly, bulky, and heavy due to the requirements for eye tracking devices, 2D steering mechanisms, and multiple displays and optical paths. Besides, the discrete perception of image quality caused by multi-resolution scheme leads to visual artifacts.

The research detailed in this dissertation focuses on establishing a new perceptual-driven approach to the design of a statically foveated HMD that aims to achieve wide FOV with the minimal degradation of the perceived image resolution within regions of frequent eye movements. The dissertation further applies this approach to the design of the statically foveated displays for both immersive and optical see-through applications.

1.1 DISSERTATION CONTRIBUTION

The overall contribution of this dissertation is the proposal and development of a new perceptual-driven approach to the design of statically foveated displays, aiming to overcome the disadvantages of a dynamically foveated display scheme. Specifically, it can be divided into three aspects.

The first aspect of the contributions is the development of a comprehensive framework of the perceptual-driven approach used to design a statically foveated display, including the human eye and head movement mechanisms, method overview, performance metrics and optimization process. The proposed foveation scheme is further validated through experimental demonstrations

using a test setup. The second aspect focuses on the design, optimization, and performance evaluation of a statically foveated display for immersive HMD based on the perceptual-driven approach. A custom-designed prototype was demonstrated experimentally, yielding excellent perceived performance without the need of eye tracker and scanner. The third part of this dissertation details the design of a statically foveated display for OST-HMDs, utilizing freeform prisms. The work highlights the optimization method and metrics employed to control the spatially varying optical power.

1.2 DISSERTATION CONTENTS

Following this chapter of INTRODUCTION, Chapter 2 BACKGROUND introduces the trade-off between resolution and FOV in detail, the HVS characteristics related to foveation technology, and an overview of the history, classification, and limitations of the existing foveation schemes.

Chapter 3 PERCEPTUAL DRIVEN APPROACH TO STATICALLY FOVEATED HMDS summarized the perceptual-driven approach fully considering the mechanisms of the human eye and head movement to realize a statically foveation scheme with wide FOV and nearly imperceptible or minimal degradation of the perceived image resolution removing eye tracking device and scanner. The performance metrics (Section 3.2), optimization process (Section 3.3), and experimental verification (Section 3.4) are demonstrated.

Chapter 4 DESIGN OF A STATICALLY FOVEATED DISPLAY FOR IMMERSIVE HMD presents the process of designing a statically foveated display for immersive HMD guided by the perceptual-driven approach, including optimization method (Section 4.2), performance evaluation and tolerance analysis (Section 4.3), and perceived performance test (Section 4.4).

Chapter 5 STATICALLY FOVEATED FREEFORM OST-HMD SYSTEM WITH LARGE FOV details the design of a statically foveated OST-HMD system with freeform prisms, including optimization method (Section 5.2), performance simulation (Section 5.3), tolerance analysis (Section 5.4) and opto-mechanical design (Section 5.5).

Chapter 6 CONCLUSION AND FUTURE WORK provides a comprehensive comparison between the dynamic dual-resolution foveation scheme and statically foveation scheme, summarizes the new method of statically foveated display design and contributions of this dissertation to the foveation technology, and outlines future work for improvement and enhancement of the foveation technology.

APPENDIX A includes a published peer-reviewed paper titled “Perceptual-driven approach to statically foveated head-mounted displays.”

APPENDIX B includes a published peer-reviewed paper titled “Perceptual-driven approach to statically foveated head-mounted displays.”

APPENDIX C provides the MATLAB© code written to generate the foveated image by gaussian-type filter.

APPENDIX D provides the CODEV macro written to optimize the foveated OST-HMD with freeform prisms.

APPENDIX E includes the global coordinates and parameters of the surfaces of the freeform prisms for the foveated OST-HMD.

2. BACKGROUND

This chapter introduces the inherent trade-off between FOV and resolution, presents the characteristics of HVS, and summarizes and classifies the existing foveation technologies. Furthermore, the limitations of the existing foveation techniques are discussed.

2.1 TRADE-OFF BETWEEN RESOLUTION AND FOV IN HMDS

Ivan Sutherland and his students proposed the first modern graphic-driven HMD prototype in the 1960s [1]. The helmet-mounted sighting system was applied on the Cobra helicopter and the Navy shot missiles in the 1960s. In 1962, Hughes Aircraft Company revealed a monocular HMD with a compact cathode-ray tube (CRT) [11]. In the 1980s, VR pioneer Jaron Lanier popularized the term "virtual reality" through his own VR company and a variety of VR devices were developed, raising awareness of VR as a concept [12]. In 1992, Tom Caudell and David Mizell of Boeing® coined the term "augmented reality" when they developed experimental AR devices to help workers with tasks such as wire harnesses, marking an important milestone in the development of AR [13]. Commercialized HMDs emerged in the 1990s, with notable examples like the Sega VR by Sega® in 1991, integrating a liquid crystal display (LCD), stereo headphones, and inertial sensors for arcade games. Forte VFX1 headgear released in 1994 by Forte Technologies®, integrated head tracking, stereoscopic 3D display, and stereo audio. In recent years, HMD commercialization soared, with notable developments in tactical and military applications and most importantly in various segments of consumer markets. In 2014, Facebook® acquired Oculus VR, stimulating competition among companies like Google®, HTC®, Samsung®, Microsoft®, and Sony® which all entered the consumer-oriented HMD market race.

Most HMD designs are based on the rectilinear sampling technique, distributing a limited number of pixels uniformly across the entire FOV. However, this approach faces inherent limitations due to the trade-off between large FOV and high spatial resolution. Expanding the FOV in HMDs with a limiting-resolution display panel allows users to perceive a larger virtual image, enhancing presence and immersion. However, it leads to a decrease in angular resolution per pixel, resulting in suboptimal optical performance and visual experience. Conversely, increasing spatial resolution uniformly with the same number of limited pixels reduces the FOV coverage. Taking an HMD with high-definition (HD) display of 1920 x 1080 pixels as an example, for a system with a 100-degree diagonal FOV, the angular resolution is about 2.73 arcminutes per pixel. If the angular resolution is set as 1 arcminute per pixel which corresponds to the visual acuity of a 20/20 standard observer, the diagonal FOV coverage of the display is only about 36°. Based on the same sampling method, simultaneously achieving both goals of 1 arcminute per pixel and 100° FOV requires a display with 6000 pixels in the diagonal direction. Nevertheless, manufacturing such displays with suitable sizes for HMD equipment poses significant challenges and results in a substantial amount of redundant data for the HVS. This redundancy arises from the fact that visual acuity degrades beyond the fovea on the retina, rendering over 92% of the data generated by the display imperceptible to the HVS.

2.2 HUMAN VISUAL SYSTEM

In the HVS, the region around the fovea provides superior resolution, contrast, and color sensitivities, which decrease rapidly with increasing angular distance away from the fovea center, known as retinal eccentricity. For convenience, a reference coordinate system, denoted as OXYZ, is established in the visual space, as depicted in Fig. 2.1 (a). The origin O is positioned at the center

of the entrance pupil of the right eye, while the Z axis aligns with the line of sight (LoS) when the eye gaze direction parallels with the head pose direction. The OXY plane is perpendicular to the Z-axis, and the Y-axis is directed upward. The virtual display plane is specified with the IX'Y'Z' reference coordinate system perpendicular to the Z-axis, where the origin I is the intersection of the Z-axis with the display plane. The X'-, Y'-, and Z'-axes are parallel to the X-, Y-, and Z-axes, respectively. As Fig. 2.1 demonstrates, the eye is gazing at a point G on the display plane in visual space. Relative to the straight-ahead gazing direction Z-axis, the eye gazing direction ϕ_G is the rotation angle of human eye, which can be decomposed into two orthogonal components, (ϕ_{Gx}, ϕ_{Gy}) , for eye rotation angle along the horizontal and vertical directions, respectively. The relative visual acuity (VA) of the HVS (denoted as VA_{HVS}) characterizes the resolution distribution as a function of the eccentricity angle of a target visual field away from the eye gaze direction. It is defined as the normalized reciprocal of the angular resolution in minutes of arc and can be formulated according to [14, 15],

$$VA_{HVS}(\theta_x, \theta_y, \phi_{Gx}, \phi_{Gy}) = e_2 / (e_2 + \sqrt{(\theta_x - \phi_{Gx})^2 + (\theta_y - \phi_{Gy})^2}), \quad (1)$$

Where e_2 represents the retinal eccentricity at which the spatial resolution drops to half of the peak value, approximately equal to 2.3° , and the eccentricity angles (e_x, e_y) of the target field from the fovea center are defined as $e_x = \theta_x - \phi_{Gx}$ and $e_y = \theta_y - \phi_{Gy}$ in the horizontal and vertical directions, respectively. All the above angle values are in degrees.

To demonstrate the perceived effects for different eye gazing directions, this dissertation showcases the simulated perceived images of a processed Briggs Target pattern in Fig. 2.2 (a) and

(c) for a gaze angle of 0° and 30° , respectively. These images, along with the Briggs Target pattern and the simulated method, will be further discussed in Section 3.4. Additionally, Figures 2.2 (b) and (d) provide zoomed-in views of regions corresponding to field angles of 10° , 30° , 50° , and 80° for the two simulated perceived images. It is evident that the foveal region along the gaze direction exhibits high resolution, while the resolution decreases rapidly as the field eccentricity angle increases.

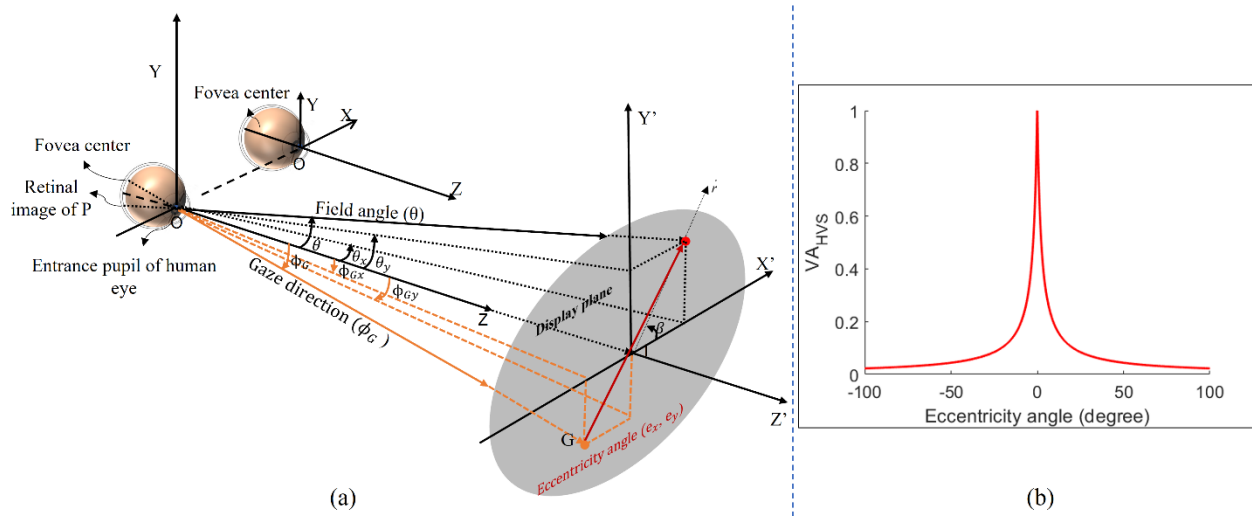


Fig. 2.1 (a) The schematic illustration of a display in visual space; (b) the VA of HVS as a function of eccentricity angle.

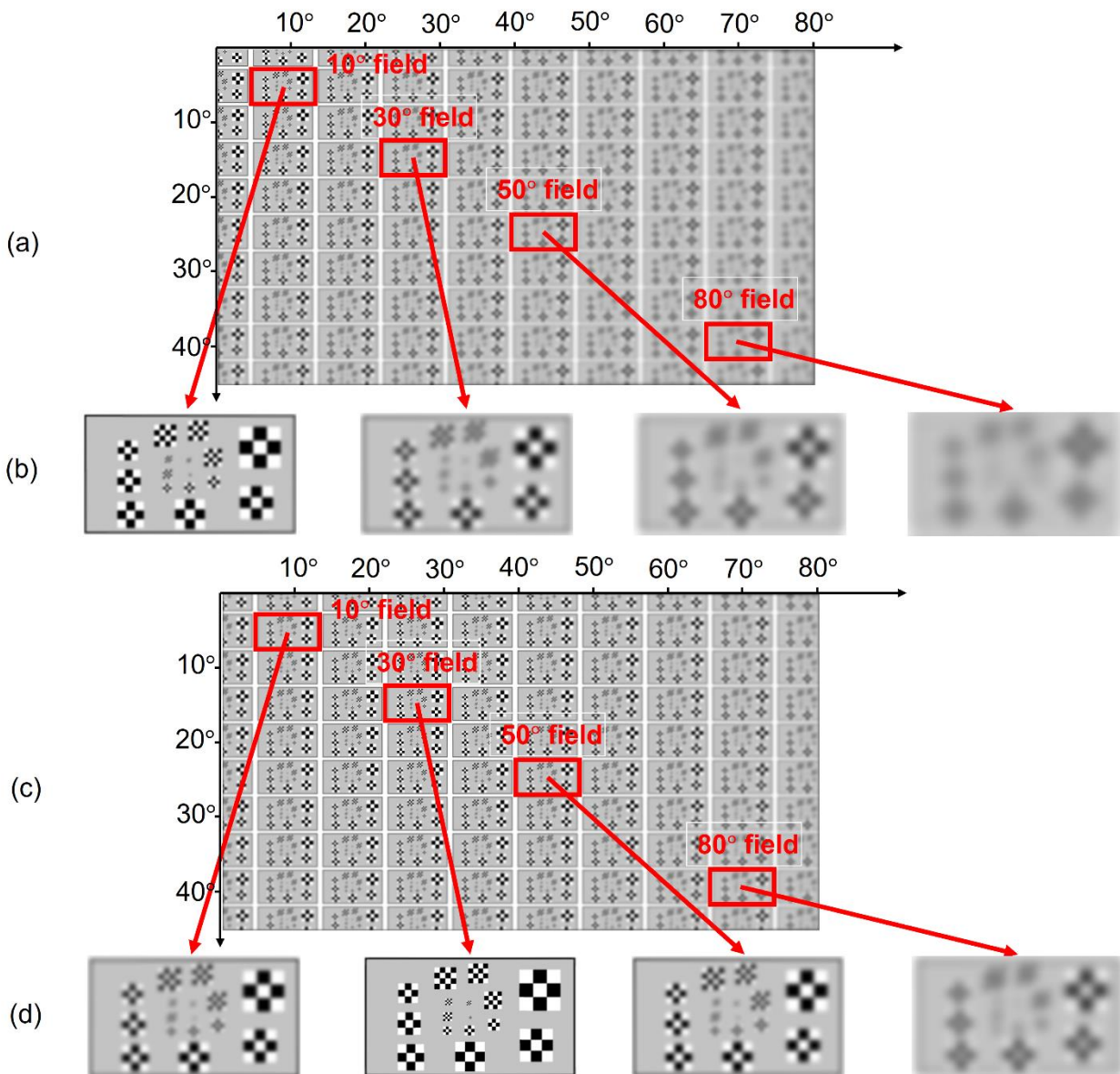


Fig. 2.2 (a) Simulated perceived image of processed Briggs Target pattern when human eye gazed at 0-degree field angle; (b) zoomed in views corresponding the field angles of 10, 30, 50, and 80 degrees, respectively. (c) Simulated perceived image of processed Briggs Target pattern when human eye gazed at 30-degree field angle; (d) zoomed in views corresponding the field angles of 10, 30, 50, and 80 degrees.

2.3 FOVEATION TECHNOLOGY

2.3.1 Categorization of foveation techniques

Inspired by the VA characteristics of the human eye, various efforts have been made to explore foveation techniques in imaging and display applications, which can be broadly classified into three categories.

The first category is research focusing on studying perception and cognition through experiments to gain insights into visual processing and the perceptual artifacts by simulated multi-resolution images or display systems [15–20]. For example, L. C. Loschky, et al. investigated the relationship between spatial vision and attentional selection using a gaze-contingent multi-resolution display [20]. Researchers have extensively examined the perceptual artifacts associated with foveated multiresolution displays, including perceptible image blur and image motion, as these artifacts have the potential to distract users. The primary goal is to strike a balance between maximizing bandwidth savings through foveation techniques and minimizing perception artifacts and performance costs.

The second category is the algorithmic approach for foveation techniques focusing on image processing [21, 22], video encoding [14, 23, 24], and graphics rendering [25–27]. These techniques aim to enable real-time video communication over low-bandwidth networks to save data transmission bandwidth and processing resources. For example, Ienaga, et al. described a Q stereoscopic video system with embedded high spatial resolution images using two channel transmission to enhance operator efficiency and improve depth perception accuracy [21]. Wang, et al. proposed an embedded foveation image coding algorithm to optimize foveated visual quality at arbitrary bit-rates by ordering the encoded bitstream [22]. Geisler and Perry demonstrated a

threefold increase in compression ratio for multiresolution images and videos [14]. Böhme, et al. demonstrated an algorithm to dynamically adjust the temporal resolution of a video in real time based on the viewer's gaze direction [23]. Several researchers employed perceptually driven foveation techniques in 3D graphics rendering [25–27]. Luebeke, et al. introduced a perceptually driven framework for accelerating interactive rendering by utilizing psychophysical models of visual perception which can produce a similar rendering effect with 2–6 times fewer polygons [26]. Murphy, et al. reported a nonisotropic hybrid image/model-based gaze-contingent rendering technique, which can significantly accelerate the rendering speed through rendering high-level 3D scene detail around a user's gaze direction in virtual environments.

The third category of work takes a hardware approach, in which spatially varying resolution for foveation scheme is provided through multiple imaging sensors or displays to improve the data saving efficiency for high-resolution detectors and displays or high-quality and complex optical systems [28–39]. For instance, Sandini, et al. demonstrated a retina-like image sensor with spatially variant resolution, requiring 35 times fewer pixels than a constant high-resolution image of 1100 x 1100 pixels [28]. Wick, et al. presented foveated imaging systems using a spatial light modulator (SLM) to correct optical aberrations of a large FOV optics at the ROI dynamically [29]. Hua and Liu integrated dual-sensor architecture with two separate imaging paths, one for foveated imaging and the other for peripheral vision. The high-resolution imaging path is steered by a 2D microelectro-mechanical systems (MEMS) scanning mirror [38]. Qin and Hua applied this architecture to develop multi-resolution foveated laparoscopes for minimally invasive surgery [39]. Katz, Lee and Hua improved Qin's multi-resolution foveated laparoscope design performance, especially for brightness and lateral chromatic aberration (LCA) correction [30].

Iwamoto, et al. showcased a bench prototype of a foveated display using 2D opto-mechanical scanners to dynamically scan a high-resolution inset image over a wide FOV background while low-resolution display [31]. Rolland, et al. presented a conceptual design for a high-resolution inset HMD system utilizing microlens arrays to duplicate a high-resolution inset image over a background display, with a liquid crystal shutter selecting the copy corresponding to the ROI being gazed at [32]. Tan, et al. demonstrated a dual-resolution HMD design employing two display panels of varying optical magnifications as image sources. Additionally, they incorporated a switchable Pancharatnam-Berry phase deflector to shift the position of the foveated view within the HMD [33]. Boris Greenberg proposed a foveated HMD design based on a direct retinal projection integrating eyetracking, dual-axis MEMS scanners, two laser sources offering different scanline densities [34]. Kim, et al. developed a dynamically-foveated AR display that combines a high-resolution foveated display with a large FOV, low-resolution peripheral display. The system includes a planar image combiner (IC) for the foveated optical path, a reverse optical path for on-axis gaze tracking, and a holographic optical element (HOE) for refracting light rays in the peripheral vision to achieve a Maxwellian viewpoint, adapting to the user's gaze utilizing polarization optics through liquid crystal photonics [35]. Lee, et al. reported a display that incorporated two modules for peripheral and foveal visions and employed a MEMS mirror to steer the holographic foveal area according to gaze direction. Additionally, an LC deflector was implemented to extend the steering range further [36]. Yoo, et al. proposed a foveated display with a single display which is achieved the foveated mode and peripheral mode based on temporal polarization-multiplexing by a doublet geometric phase lens [37].

2.3.2 Limits of dynamic foveation method

Among the various methods that attempted to apply a foveation method to the hardware design of foveated HMD system [28–38], a dynamic discrete foveation approach has been commonly employed. This method involves dynamically steering a high-resolution foveated region according to the user's gaze direction, while a lower-resolution region provides peripheral awareness. The dynamic foveation method often involves a dual-display architecture, where two displays or optical paths with varying pixel resolutions or optical magnifications are utilized to render the foveated and peripheral areas, respectively. The foveated area yields high spatial resolution while typically covering a small FOV, so eye tracking is naturally required to track the viewer's LoS and determine the instantaneous ROI for aligning the higher-resolution display. In the meanwhile a scanning method is obliged to steer and align the high-resolution foveated display approximately with the viewer's LoS to achieve foveated rendering mechanically [30–33, 37], optically [32, 33], or combinedly [36]. The necessity of multi-resolution displays and optical path, a 2D scanning mechanism, eye tracking device or equivalent causes the dynamically foveated multi-resolution display inevitably complex, costly, bulky, and heavy. Moreover, the discrete resolution samples provided by the dynamically foveated multi-resolution display introduce visual artifacts due to the discontinuous perception of image quality, which can impact the overall visual experience.

3. PERCEPTUAL DRIVEN APPROACH TO STATICALLY FOVEATED HMDS

As touched upon in Section 2.3.2, the drawback of the dynamic foveated dual-resolution display was discussed. To address the limitations, this chapter describes a new perceptual-driven approach to the design of a statically foveated display covering large FOV with nearly imperceptible or minimal degradation of the perceived resolution within the region of frequent eye movement r while also eliminating the equipment of multi-resolution displays, eye tracking devices, and a 2D scanner. A full accounting of this body of work, including approach overview, performances metrics, optimization process, and simulation and experiment verification, has been published [40] and is included in APPENDIX A.

3.1 PERCEPTUAL DRIVEN APPROACH OVERVIEW

Refer to the book [41], although the maximum eye rotation is around 25° to 35° , the optimal required eye rotation angle for a device is much less than the maximum eye rotation angle. Motivated by the fact that an HMD is generally attached to a user's head with a relatively fixed viewing position, the perceptual-driven approach was proposed fully considering the characteristics of eye and head movement mechanisms and the perceived visual effects.

To better describe the degradation rate in the perceived resolution of a foveated display considering the eye and head motion mechanisms, the display plane may be divided into three functional regions, as a fovea region, a parafovea region, and a peripheral region, by two critical balance field angles, illustrated in Fig. 3.1 (a). Generally, the three regions have a common rotationally symmetrical center at display center I. Like the fovea in the retina, the display's fovea

region is fixed at the center statically, offering the highest resolution and a small and uniform or nearly uniform pixel pitch to provide high angular resolution when the eye gaze direction falls within this region. The fovea region is defined by a critical field angle, θ_{c1} , that serves as its boundary. This critical field angle is the visual and musculoskeletal balance point and the region within which frequent and comfortable eye movement occurs. A preferred choice for θ_{c1} is between 5° and 20° , for instance, Burgess-Limerick, et al. proposed that comfortable eye movements occur within a field angle of $\pm 15^\circ$ for a good compromise between visual and musculoskeletal needs [42]. Adjacent to the fovea is the parafovea region, where resolution degradation is moderate within the annular zone defined by θ_{c1} and θ_{c2} . θ_{c2} is preferably chosen between 20° and 40° , and is treated as the balance point between eye movements and head motion, with head motion becoming more preferred beyond 30° for eye rotation angle [43]. The peripheral region, beyond θ_{c2} , experiences rapid resolution degradation and primarily serves to peripheral vision and the sense of immersion. Within this region, comfortable eye movements are unlikely to occur and head or body motion is preferred. An HMD system typically employs a head tracker for scene rendering updates based on head motion while maintaining the eye's relative position to the display field, and thus eye gaze direction much less likely falls within the peripheral region than the other two regions.

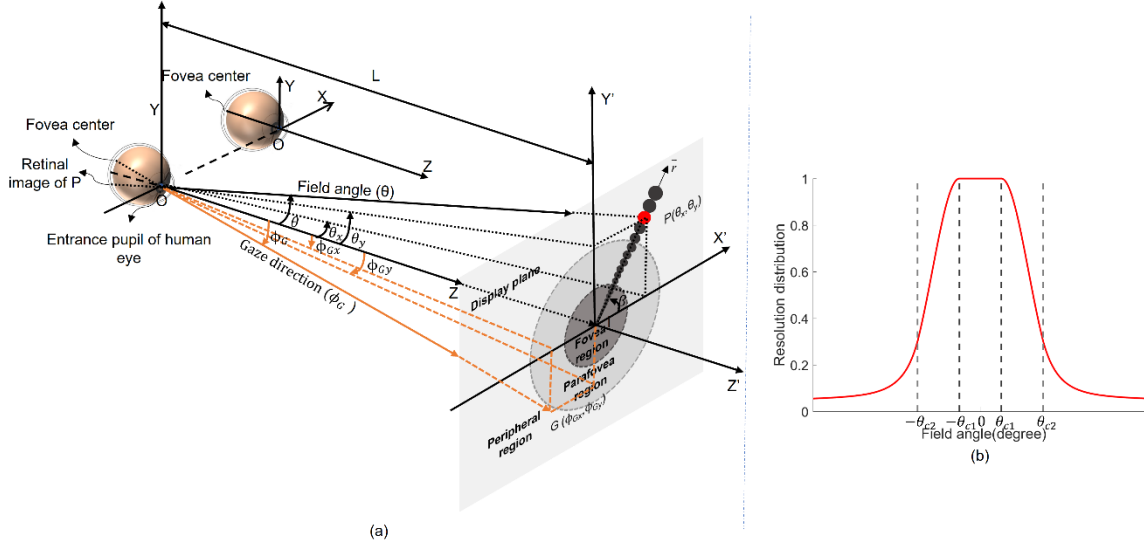


Fig. 3.1 (a) The schematic illustration of a continuously foveated display where its angular resolution varies as a function of the field angle θ and symmetric about the display center I; (b) Example of an angular resolution distribution function along a given direction crossing the display center I as a function of the field angle.

The pixel distribution of a foveated display can be described by the angular resolution distribution function, denoted as $F_{FD}(\theta_x, \theta_y)$, which is defined as the reciprocal of the angular resolution of the display in minutes of arc, where θ_x and θ_y correspond to the X-component and Y-component of the field angle θ in the horizontal and vertical directions, respectively. By considering the three divided functional regions, the angular resolution distribution of a statically foveated display can be represented as:

$$F_{FD}(\theta_x, \theta_y) = \begin{cases} f_1(\theta_x, \theta_y) & |\theta| \leq \theta_{C1} \\ f_2(\theta_x, \theta_y) & \theta_{C1} < |\theta| \leq \theta_{C2} \\ f_3(\theta_x, \theta_y) & \theta_{C2} < |\theta| \leq \theta_{\max} \end{cases}, \quad (2)$$

where f_1, f_2 , and f_3 represent the segmented functions that describe the resolution distribution within their respective regions, and θ_{\max} is the maximum field angle in the radial direction. To maintain resolution continuity and image smoothness across the boundaries of a foveated display, it is

important for the function values and derivatives at the first and second critical balance points (θ_{c1} and θ_{c2}) to be equal.

3.2 PERFORMANCES METRICS

To optimize and select the optimal one from many forms of resolution distribution functions, we established a set of performance merit functions to minimize perceivable quality degradation, enhance data saving, and facilitate implementation. The performance metrics has two types, one assesses perceived image quality degradation, while the other measures data saving efficiency.

Taking into account the specifications of degradation rate in resolution for the three functional regions in the display, as well as the dynamic nature of eye movements and the VA characteristics of the HVS, the perceived visual acuity of a display, also referred to as the perceived resolution, was characterized. It factors in the VA of a 20/20 standard observer and the resolution distribution of the display as the function of both the field angle and the eye gaze direction. For a given field θ , the perceived VA of a foveated display, expressed as VA_{FD} , is determined by the smaller value by comparing the values of display's resolution distribution and the VA curve of a 20/20 standard observer when the eye is gazed along ϕ_G direction, as illustrated by Fig. 3.1 (a). Generally, it can be expressed as,

$$VA_{FD}(\theta_x, \theta_y, \phi_{Gx}, \phi_{Gy}) = \min[F_{FD}(\theta_x, \theta_y), VA_{HVS}(\theta_x, \theta_y, \phi_{Gx}, \phi_{Gy})]. \quad (3)$$

For example, Fig 3.2 demonstrates the perceived VA of a foveated display when the eye is gazing at 40° angle away from the straight-ahead direction, in which we assume the resolution distribution function of the foveated display is a rotationally symmetric Gaussian function, as

$F_{FD}(\theta) = e^{-0.001 \times \theta^2}$. The VA curve is plotted in black solid line calculated by Eq. (1), and the resolution distribution of the foveated display is marked as red solid line. Applying the Eq. (3), the perceived VA of the display is plotted by the yellow line with “*” markers. The yellow-shaded area under the curve represents the region where the perceived image quality matches the observer's VA, while the black-shaded area indicates the region where the display resolution limits the perceived image quality instead of the observer's VA.

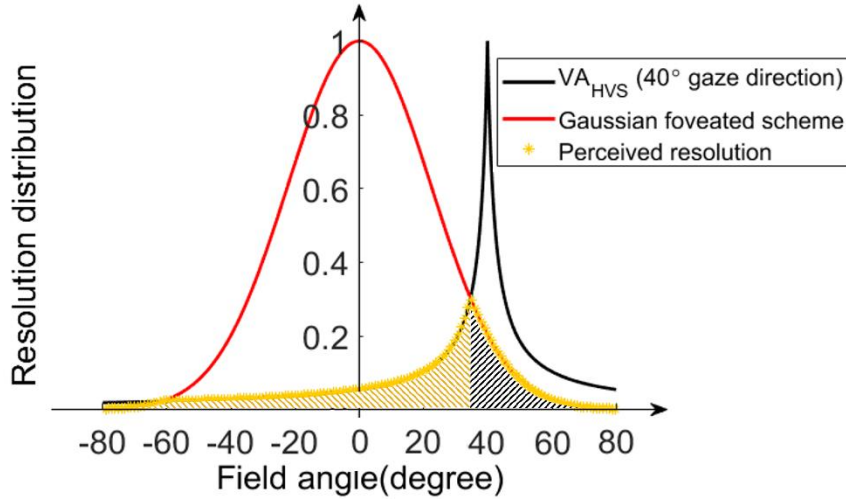


Fig. 3.2 Illustration of the perceived resolution of a foveated display with its resolution distribution function in the form of a simple Gaussian function while the eye is gazed in the direction of 40° away from the display center.

Further to evaluate the perceived performance and make comparison among different resolution distribution functions for foveated displays, two types of metrics are developed—the perceived maximum resolution of a display $VA_{FD}|_{\max}$ and the volume ratio VR_{FD} . The perceived maximum resolution of a display is the highest resolution experienced throughout the entire FOV, providing an evaluation of the peak performance relative to eye movements, expressed as,

$$VA_{FD}|_{\max}(\phi_{Gx}, \phi_{Gy}) = \max[VA_{FD}(\theta_x, \theta_y, \phi_{Gx}, \phi_{Gy})]. \quad (4)$$

The volume ratio is a summative metric that determines if the perceived resolution of a display falls below the perceptible limit of the HVS. It is calculated by comparing the volumes enclosed by the perceived resolution curve and the VA curve of the HVS across the display's FOV for various eye gaze directions, and is defined as,

$$VA_{FD}(\phi_{Gx}, \phi_{Gy}) = \frac{\int_{-\theta_{Xmax}}^{\theta_{Xmax}} \int_{-\theta_{Ymax}}^{\theta_{Ymax}} VA_{FD}^2(\theta_x, \theta_y, \phi_{Gx}, \phi_{Gy}) d\theta_x d\theta_y}{\int_{-\theta_{Xmax}}^{\theta_{Xmax}} \int_{-\theta_{Ymax}}^{\theta_{Ymax}} VA_{HVS}^2(\theta_x, \theta_y, \phi_{Gx}, \phi_{Gy}) d\theta_x d\theta_y}, \quad (5)$$

where θ_{Xmax} and θ_{Ymax} are the maximum half FOVs of the display system in the horizontal and vertical directions, respectively. The volume ratio of one indicates that the resolution of a display through its entire FOV is at or above the VA of the HVS, regardless of eye gaze direction. The metrics described in Eqs. (3) to (5) assess the perceived resolution performance of a display based on its field angles and gaze directions.

Using the analytical method outlined by Hua and Liu [38], the total rendered data of a system are calculated by integrating its resolution distribution across all fields, expressed as follows:

$$B = \int_{-\theta_{Xmax}}^{\theta_{Xmax}} \int_{-\theta_{Ymax}}^{\theta_{Ymax}} F_{FD}^2(\theta_x, \theta_y) d\theta_x d\theta_y. \quad (6)$$

To assess and compare data sampling efficiency of various foveation schemes, we use a uniformly sampled, single-resolution display (SRD) as a reference. The SRD provides consistent resolution equivalent to the peak resolution of a foveated system throughout its entire FOV, which matches the FOV of the foveated display. The data sampling efficiency of a foveated display is defined as,

$$S_{FD} = \frac{B_{SRD} - B_{FD}}{B_{SRD}}. \quad (7)$$

3.3 OPTIMIZATION

To implement the proposed method described in Section 3.1, we optimized the choices of critical balance points and resolution distribution functions based on eye and head motion characteristics, perceived performance metrics defined in Eqs. (3) through (5), and data saving efficiency by Eq. (7). By considering these factors and the described metrics described in Section 3.2, we adjust the segmented functions' general form to achieve an optimal resolution distribution across the FOV.

3.3.1 Optimization process

The overall flowchart schematic of the optimization process is demonstrated in Fig. 3.3. The optimization process begins with initializing the three key aspects, the resolution distribution functions, target display specifications, and threshold performance metrics. The initialization step involves choosing the general form of functions and relevant critical balance points, specifying the parametric space and range for optimization. There are several critical factors considered for a statically foveated display. One is the target display specifications including performance requirements, such as spatial resolution and FOV, and hardware constraints, for instance total pixel counts and data bandwidth available. The other consideration is the threshold values of the performance metrics that are used to determine if a parametric combination satisfies the target display specifications. Following the initialization step, parametric combinations are evaluated based on performance metrics and compared against threshold values. Finally, the optimal resolution distribution is determined by selecting the parametric combination that balances perceptual quality, data saving efficiency, and hardware constraints.

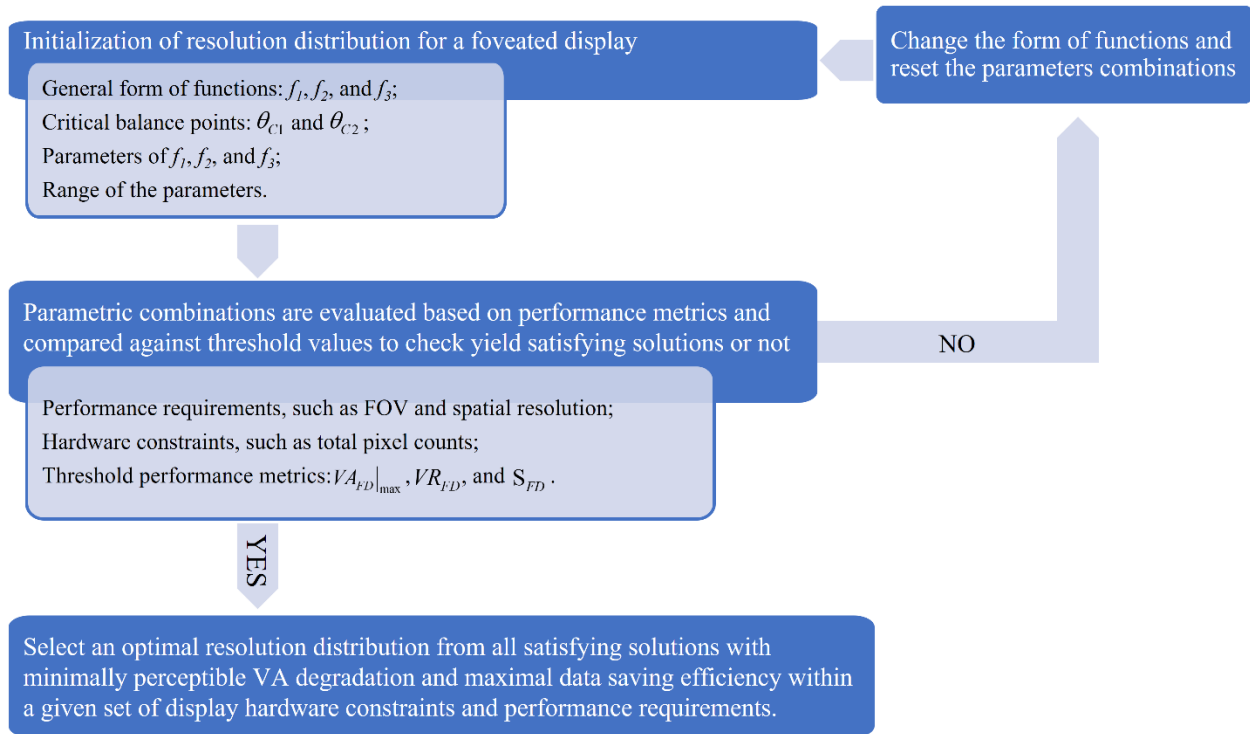


Fig. 3.3 Overall flowchart schematic of the optimization process.

3.3.2 Optimization variables

Based on the paper [40], in the fovea region, a uniform or nearly uniform angular resolution is assumed to ensure minimal impact on image quality degradation when the eye is gazing within this region. Within the parafovea region, a Gaussian function is selected to describe the resolution distribution, which offers not only an elegant approximation of the VA degradation, but also a statistical estimation of the probability of eye movements in the region. For the peripheral region, the resolution distribution is modeled via the HVS' VA curve at a large eccentricity angle, adjusted with a polynomial correction function for continuity at the boundary. To sum up, the general form of the resolution distribution function as a starting point for initialization is modeled as

$$F_{FD}(\theta) = \begin{cases} F_0 & |\theta| \leq \theta_{C1} \\ F_0 e^{\frac{-(\theta-\theta_{C1})^2}{2\sigma^2}} & \theta_{C1} < |\theta| \leq \theta_{C2} , \\ \frac{2.3F_0}{2.3 + (\theta - \phi_{th})} + \Delta(\theta) & |\theta| > \theta_{C2} \end{cases} \quad (8)$$

where F_0 is the reciprocal of the peak angular resolution at the display center field, σ is the standard deviation of the Gaussian function, which determines the degradation rate in resolution for the parafovea region, ϕ_{th} is a threshold angle for eye gaze direction deciding the eccentricity angle in the peripheral region and the rate of resolution degradation, and $\Delta(\theta)$ is the polynomial correction function. The third segment, which has little impact on perceived performance and data sampling efficiency, $\Delta(\theta)$ can be adequately represented by a simple third-order polynomial function. All the variables discussed above are crucial considerations in the optimization process to achieve an optimal foveated scheme.

3.3.3 Example of foveation scheme

To develop a proof-of-concept prototype, we demonstrate the availability of a commercially available 4K monitor for the statically-foveated display. The target display specifications include a minimum FOV of 80°, a center angular resolution of 1 arc minute per pixel, and a data sampling efficiency of 50% or higher. At a 30° eye gaze angle from the display center, the desired perceived maximum resolution is better than 4 arc minutes, and the volume ratio should exceed 0.5. Out of the 5712 foveation schemes evaluated, 133 schemes successfully met the threshold performance specifications. Among the 133 evaluated schemes, we picked an optimal foveation scheme with a resolution distribution function expressed as follows:

$$F_{FD}(\theta) = \begin{cases} 1 & |\theta| \leq 10^\circ \\ e^{-\frac{1}{2} \left(\frac{\theta-10}{12.89} \right)^2} & 10^\circ < |\theta| \leq 30^\circ \\ \frac{2.3}{2.3 + (\theta - 24.63)} & |\theta| > 30^\circ \end{cases} \quad (9)$$

3.3.4 Discussions of the selected foveation scheme

This section provides a comprehensive evaluation of the proposed continuous foveation scheme outlined in Eq. (9) and compares it with established dual-resolution schemes [38]. Because our focus is on statically foveated displays, we assume that there will be no optical or mechanical scanning mechanism to dynamically align the position of the fovea region based on eye gaze. In all foveation schemes, the fovea region remains fixed at the display center irrespective of the eye gaze direction. A dual-resolution scheme divides the field into a high-resolution fovea region and a reduced-resolution peripheral region. To enable effective comparison and guidance, we selected two dual-resolution schemes: one with a narrow $\pm 10^\circ$ fovea region and another with a wider $\pm 30^\circ$ fovea region. Fig. 3.4 illustrates the resolution distribution functions of three foveation schemes: the proposed three-segment continuous foveation scheme (red solid curve with asterisk marks), the 10° dual-resolution scheme (green dashed curve with diamond marks), and the 30° dual-resolution scheme (blue dotted curve with pentagram marks). The VA curve of the HVS for an eye gaze angle of 0° is also included as a reference (black solid curve).

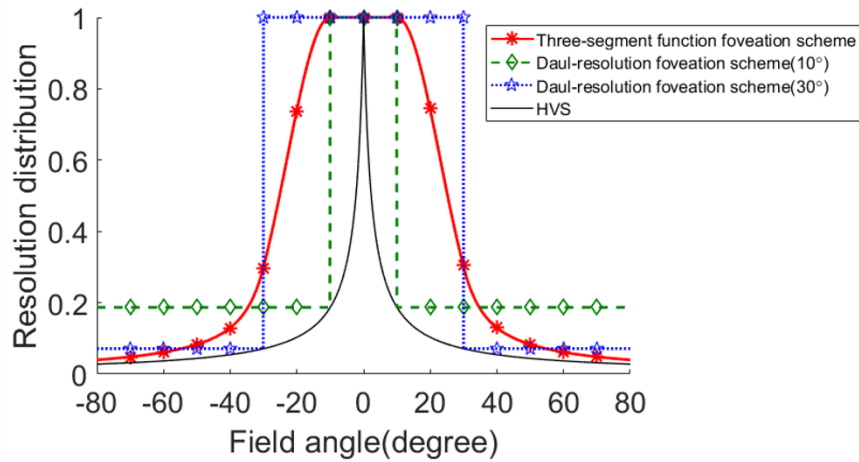
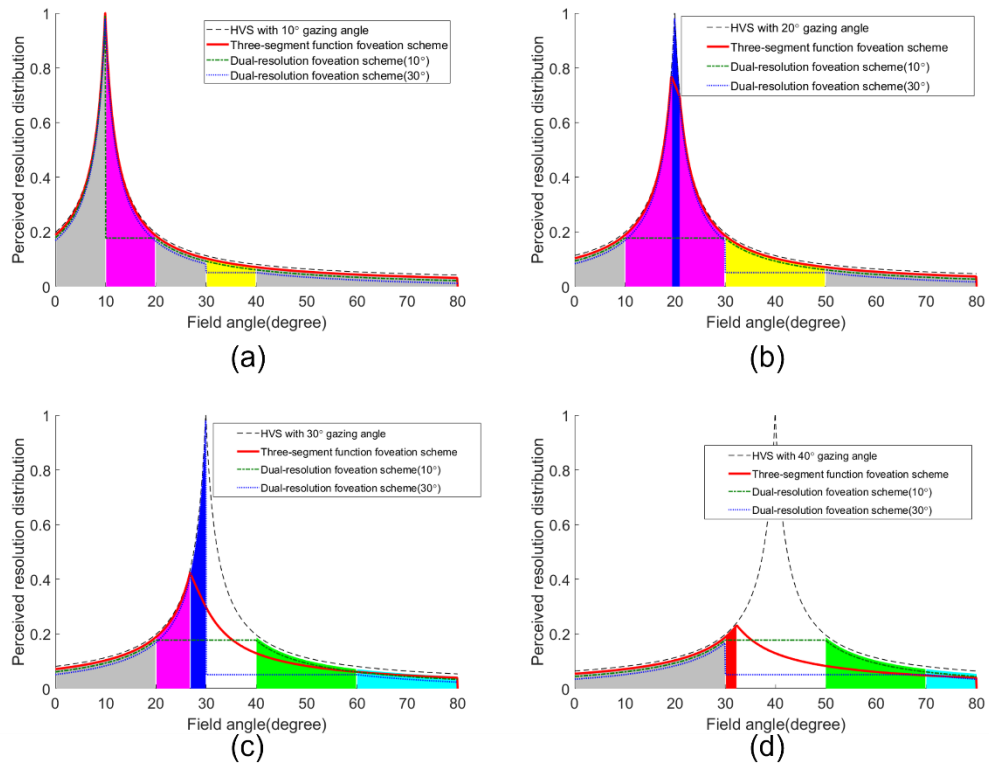


Fig. 3.4 Resolution distribution for three different foveation schemes: proposed three-segment continuous foveation scheme defined by Eq. (9), a 10° dual-resolution scheme, and a 30° dual-resolution scheme.

The perceived resolution of the three foveation schemes depicted in Fig. 3.4 was analyzed and compared using the metrics defined in Section 3.2. The perceived VA of the schemes was computed for different field angles and eye gaze angles. Figures 3.5(a) to 3.5(d) present the results with half of the display FOV from 0° to 80° for eye gaze angles of 10°, 20°, 30°, and 40°, respectively, in which the perceived VA curves for the continuous foveation scheme, 10° dual-resolution scheme, and 30° dual-resolution scheme are represented by the red solid line, green dashed line, and blue dotted line, respectively. Shading is used to indicate regions where the perceived VA of a particular scheme matches that of a 20/20 standard observer. For example, the red, green, and blue-shaded areas represent the regions where only the continuous foveation, 10° dual-resolution, or 30° dual-resolution scheme achieves the same perceived VA of a 20/20 standard observer, respectively. The gray-shaded areas indicate regions where all three schemes achieve the same perceived VA of a 20/20 standard observer. The yellow, magenta, and cyan-shaded areas represent combined regions of different schemes yield image quality as high as the

VA of a 20/20 standard observer. The unshaded area under the HVS curve denotes regions where none of the foveation schemes matches the VA of a 20/20 standard observer.

The continuous foveation scheme closely matches the HVS limiting resolution for eye rotation angles up to $\pm 15^\circ$. As shown by Fig. 3.5(a), at a 10° eye rotation angle, the perceived VA across the entire field is equivalent to or better than that of a 20/20 standard observer. For field angles between 10° and 30° , the 10° dual-resolution scheme shows significant performance drop, while the 30° dual-resolution scheme performs similarly to the continuous foveation scheme. When the eye rotates within the parafovea region, the perceived resolution gradually degrades for both the continuous foveation and 30° dual-resolution schemes. The continuous foveation scheme outperforms the 10° dual-resolution scheme generally. In the peripheral region, the continuous foveation scheme exhibits further resolution degradation but is still better than the 30° dual-resolution scheme within 70° . The proposed foveation scheme provides minimal perceivable resolution degradation across the entire FOV within the $\pm 15^\circ$ eye rotation angle and overall better resolution performance compared to the dual-resolution schemes.



■ All three schemes are as high as the HVS	■ Three-segment and 30° dual-resolution scheme are as high as the HVS
■ Only 30° schemes is as high as the HVS	■ Three-segment and 10° dual-resolution scheme are as high as the HVS
■ Only 10° schemes is as high as the HVS	■ 10° and 30° dual-resolution scheme are as high as the HVS
■ Only three-segment schemes is as high as the HVS	

Fig. 3.5 The perceived visual acuity of three different foveation schemes shown in Fig. 3.4 as a function of field angles for the eye gaze angle of (a) 10°, (b) 20°, (c) 30°, and (d) 40°, respectively.

By Eqs. (4) and (5), we calculated the perceived maximum resolution and volume ratio for the three foveation schemes across eye gaze angles ranging from 0° to 40° with a 5° increment. The results are presented in Figs. 3.6(a) and 3.6(b), respectively. Based on Fig. 3.6 (a), the maximally perceived resolution of continuous foveation scheme maintains a peak perceived resolution of 0.95 or higher within ±15° eye gaze angle, while the maximally perceived resolution of the 10° dual-resolution scheme drops below 0.3 at 15° eye rotation angle. In the parafovea region, the maximally perceived resolution of the continuous foveation scheme gradually decreases from 0.95 to 0.45, whereas the 10° dual-resolution scheme remains consistently low beyond 15°. Although

the maximally perceived resolution of the 30° dual-resolution scheme maintains its peak resolution until 30°, beyond 30°, it sharply declines. Fig. 3.6(b) indicates that, for volume ratio, over 95% of the display's fields performs to the limit of the HVS within $\pm 25^\circ$ eye gaze angle for the continuous foveation scheme, while only around 86% and 78% of the display fields performs to the limit of the HVS for the 30° and 10° dual-resolution schemes at 25° eye gaze angle, respectively. Although the 30° dual-resolution scheme generally has higher perceived maximum resolution for angles less than 30°, its volume ratio is substantially lower, indicating more regions with lower perceived resolution. Overall, the continuous foveation scheme achieves adequate perceived resolution without employing dynamic foveation and degrades more gracefully than the traditional dual-resolution schemes, especially in areas with frequent eye movements.

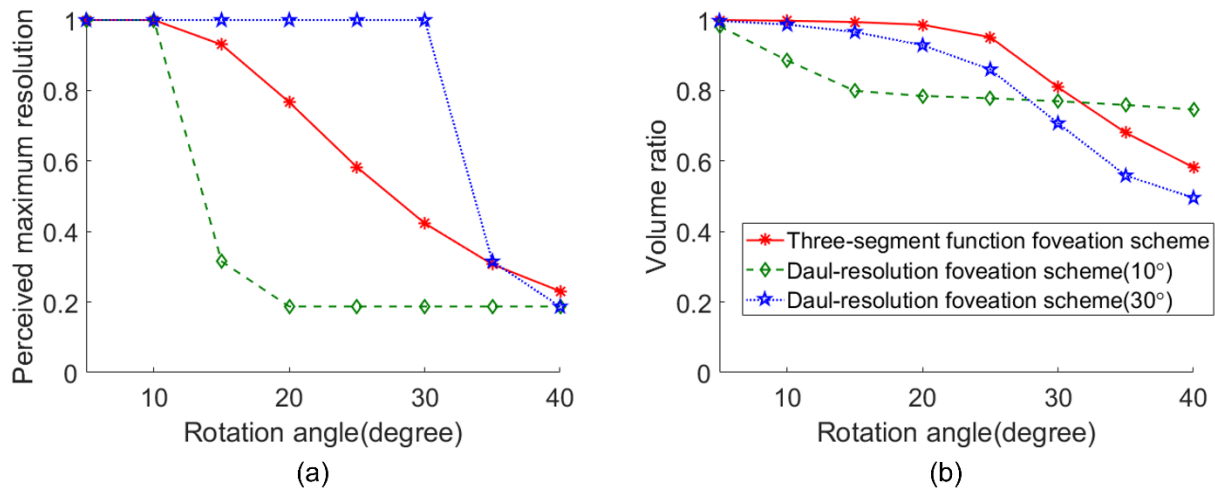


Fig. 3.6 The comparison of (a) the perceived maximum resolution and (b) volume ratio of the three foveation schemes shown in Fig. 3.4 as a function of eye gaze angles.

Applying the Eq. (6) and Eq. (7), Fig. 3.7(a) shows the relative data sampling efficiency for the three foveation schemes as a function of full FOV. The continuous foveation scheme achieves a high data saving efficiency of approximately 81.5% and 92.8% for displays with 100° and 160°

FOV, respectively. For 100° FOV, the sampling efficiency of the continuous scheme is about 7% lower than the 10° dual-resolution scheme and about 18% higher than the 30° dual-resolution scheme at the same FOVs. Fig. 3.7(b) illustrates the required pixel count in a diagonal direction for the four display schemes, assuming a peak resolution of 1 arc minute per pixel to match the HVS. The continuous foveation scheme requires approximately 2900 pixels to achieve a 100° FOV, while a commercially available 4K display is sufficient to support an FOV over 160°. In comparison, the 10° dual-resolution scheme requires 1900 pixels, the 30° dual-resolution scheme requires 3400 pixels, and the single uniform resolution scheme requires 6000 pixels for the same 100° FOV.

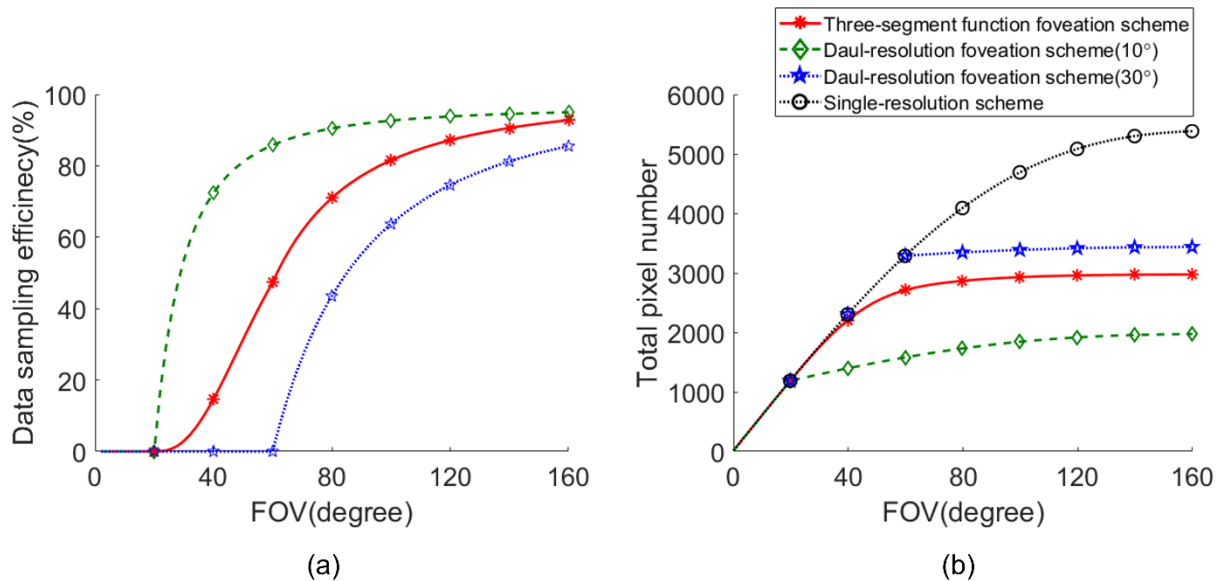


Fig. 3.7 (a) The comparison of data sampling efficiency as a function of the overall FOV for three different foveation schemes shown in Fig. 3.4; (b) The comparison of total pixel number required in a diagonal direction as a function of the overall FOV among the three foveation schemes shown in Fig. 3.4 and a single-resolution display.

3.4 EXPERIMENTAL VERIFICATION

To experimentally demonstrate and validate the visual effects of a statically foveated display described by Eq. (9), we constructed a camera-monitor test setup. The setup involved a 27" 4K monitor with a pixel size of $155.7 \mu\text{m}$ and a resolution of 3840 by 2160 pixels. To generate the necessary high-resolution target images, we focused on a horizontal FOV of 80° starting from the top-left corner pixels. This ensured sufficient pixel density to achieve the desired resolution of 0.5 arcminutes per pixel matching the highest VA of the HVS. The target images effectively covered a quadrant of the total field, spanning up to 160° horizontally. To capture the images, we preserved a fixed position for both the monitor and the camera, employing a method where the rendering viewport of the monitor virtually panned across the entire FOV of the target images. This emulation of a scanning motion resembled the movement of a virtual pair of monitor and camera across a large display. For the camera, we utilized a 2K digital camera equipped with a 50-mm focal length lens. The camera was centered with the 27" monitor, positioned at a distance of 1070 mm. In this setup, the camera was oriented perpendicular to the monitor surface, offering an angular resolution of approximately 0.25 arcminutes per pixel to ensure satisfactory image contrast and resolution at the Nyquist frequency of 60 cycles/degree of the display. We measured the modulation transfer function (MTF) of the camera using the slanted edge method with Imatest® software.

To render a foveated image, the process begins with a full-resolution target image. The foveated image, which is to be displayed, is obtained by convolving the original image with a resolution distribution function acting as a filter. Because the setup produces a peak resolution of 0.5 arcminutes per pixel, the resolution distribution function, as Eq. (9), is scaled by a factor of 2.

A Gaussian-type filter is applied to be the convolution filter with variables of standard deviation and convoluted area to control the blur degree, which is described in detail in paper [40] and the code is demonstrated in APPENDIX C. Fig. 3.8(a) showcases zoomed-in images captured at different field angles, namely 10° , 30° , 50° , and 80° . These images correspond to a resolution target and align with the resolution distribution function. The monitor used in this setup has a pixel pitch of $155.7 \mu\text{m}$, resulting in a pixel density of 163 PPI. After applying the convolution filter, the effective pixel density distribution for the foveated display is depicted in Fig. 3.8(b).

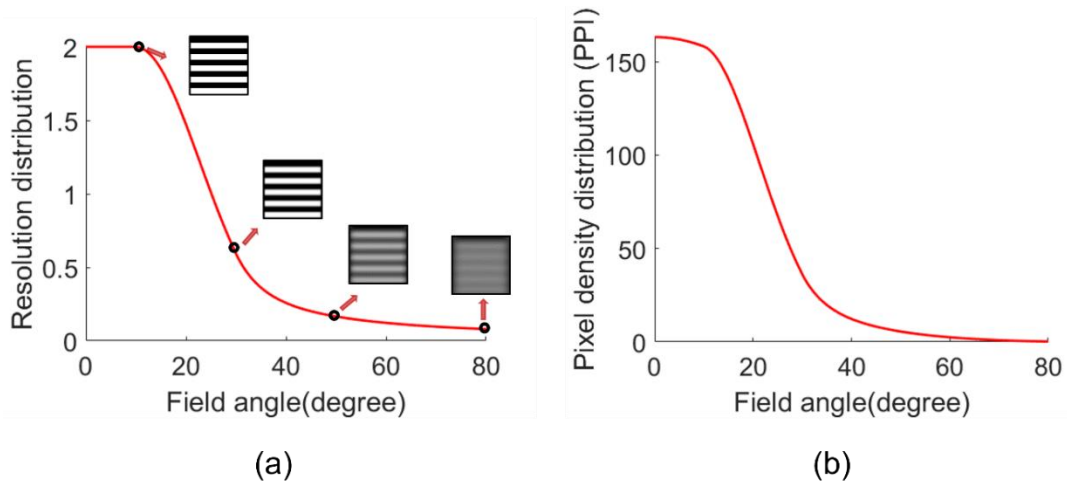


Fig. 3.8 (a) Examples of four captured zoomed-in images corresponding to 10° , 30° , 50° , and 80° field angles; (b) effective pixel density distribution for the foveated display setup as a function of field angles.

3.4.1 Objective assessment and validation

For an objective assessment of the image quality produced by the proposed foveation approach, a 4K-resolution image of modified Briggs targets was generated. The detail of the modified Briggs targets was described in the paper [40]. Fig. 3.9 (a) presents a captured image of the original 4K-resolution Briggs target pattern displayed on the 4K monitor using a 16mm focal length camera lens. The captured image includes horizontal and vertical axes to indicate the field angle on the

monitor, with the top-left corner pixel as the $(0^\circ, 0^\circ)$ field angle. Within the captured image, the red box marks the locations of four Briggs targets centered at 10° , 30° , 50° , and 80° in the diagonal direction. In Fig. 3.9(b), zoomed-in images of these targets are captured using a 50mm focal length camera lens. The rightmost side of the image includes an inset image showing the smallest checkerboard with 1-pixel checkers. These captured images successfully demonstrate sufficient resolution for the original full-resolution target.

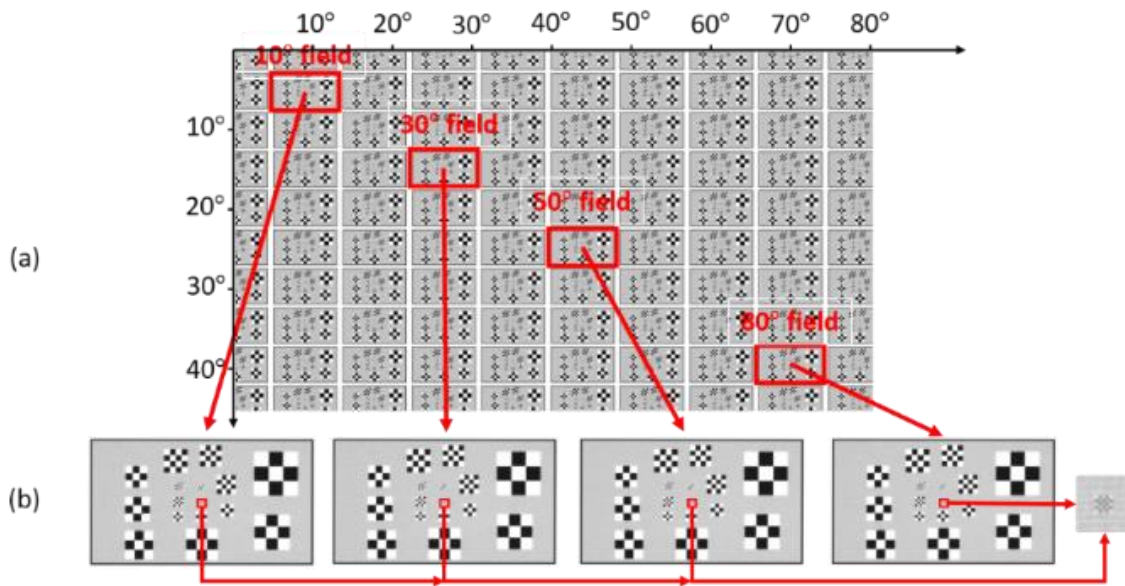


Fig. 3.9 (a) Captured image of original 4K Briggs Target pattern by camera; (b) zoomed in views corresponding the viewing angle of 10, 30, 50, and 80 degrees.

We then applied the rendering method described earlier to generate a foveated image of the Briggs target mosaic shown in Fig. 3.9(a). Fig. 3.10(a) displays the captured foveated image using a 16mm camera lens to provide an overall view of the effect. Subsequently, zoomed-in images of the four marked targets centered at the 10° , 30° , 50° , and 80° field angles are captured using a 50mm camera lens to emulate the corresponding eye gaze angles, as presented in Fig. 3.10(b). For each sub-image, we objectively determined the just distinguishable checkers (JDC) by identifying

the checkerboards at which the contrast of the light-dark checkers dropped to approximately 20%. The resulting JDC values for the 10°, 30°, 50°, and 80° field angles were 1-pixel, 3-pixel, 12-pixel, and 18-pixel checkers, respectively. The right side of each sub-image illustrates the magnified views of these JDCs. To compare the results, we simulated the perceived images of a 20/20 standard observer with the eye rotated at angles of 10°, 30°, 30°, and 30°, respectively, by the captured zoom-in images of the same areas as shown in Fig. 3.9(b). With the same rendering method, the perceived images were rendered by convolving the corresponding images shown in Fig. 3.9(b) with the filter corresponding to the VA of the HVS defined by Eq. (1). For the zoom-in image at the 80° field angle, the filter assumed an eye gaze angle of 30° instead of 80°, considering the limits of frequent and comfortable eye rotation. The simulated perceived images of a 20/20 standard observer for the same local areas as in Fig. 3.10(b) are presented in Fig. 3.10(c), also including the magnified views of the corresponding JDCs. The JDC for each target were objectively determined from the perceived images, resulting in JDC values of 1-pixel, 1-pixel, 10-pixel, and 25-pixel checkers for the 10°, 30°, 50°, and 80° field angles, respectively. Comparing Figures 3.10(b) and 3.10(c), the foveated rendering method yields visually comparable image quality to the perceived images of original full-resolution images, demonstrating the effectiveness of the proposed approach in rendering visually imperceptible quality degradation.

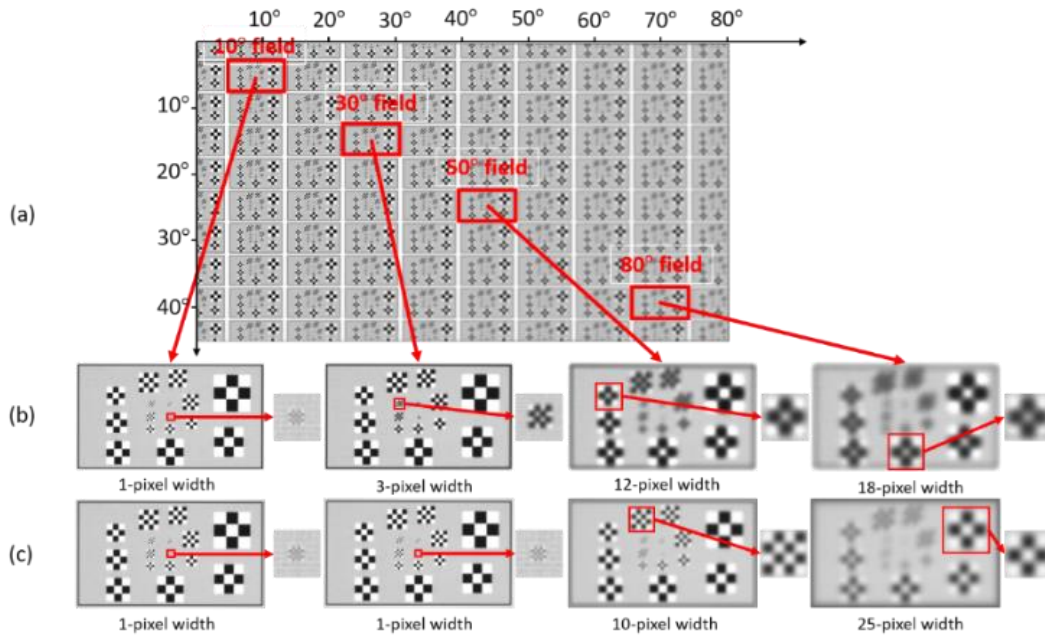


Fig. 3.10 (a) Captured image of processed Briggs Target pattern by camera; (b) zoomed in views corresponding the viewing angle of 10, 30, 50, and 80 degrees; (c) 4 rendered images of the same local areas perceived by a standard observer with the eye rotated at the angles of 15, 30, 30, and 30 degrees.

In addition, we applied the same procedure to a 4K resolution image captured from a real scene. In Fig. 3.11(a), the captured foveated image of the entire scene is presented, highlighting four sub-regions marked by red boxes that correspond to field angles of 10°, 30°, 50°, and 80°. In Figs. 3.11(b) and 3.11(c), the zoom-in images of these regions are presented, showcasing the original full-resolution image and the rendered foveated image, respectively. Additionally, Figs. 3.11(d), (e), and (f) illustrate the perceived images of the sub-regions for a 20/20 standard observer at eye rotation angles of 0°, 15°, and 30°, respectively, for comparison. The statically foveated display in Fig. 3.11(c) generally provides visually comparable or superior image quality to the perceived images of a full-resolution display across most eye gaze angles. Except, the perceived image of the 50° sub-region at a 30° eye gaze angle appears slightly sharper than the captured foveated image of the same region.

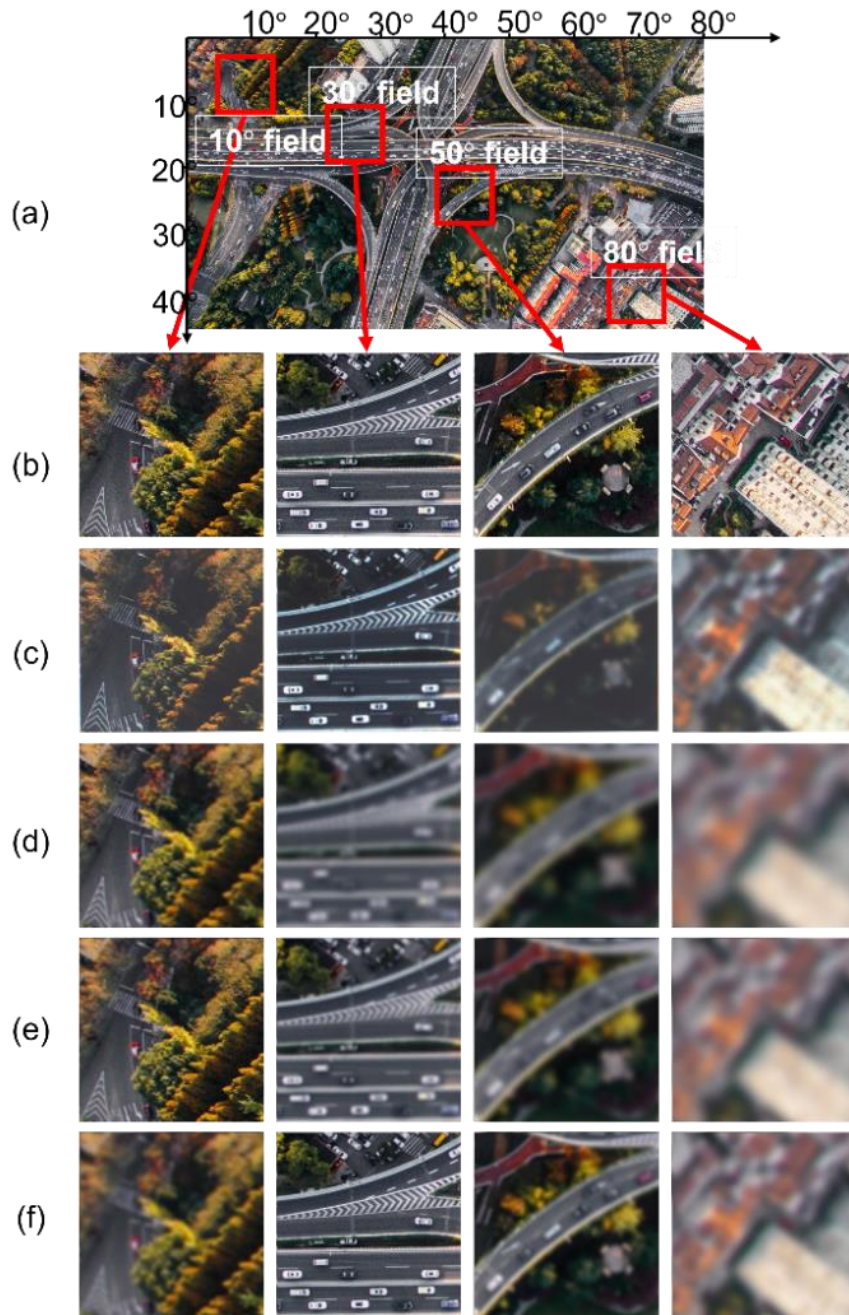


Fig. 3.11 (a) Captured image of a foveated scene with four marked regions of interests, corresponding to 10°, 30°, 50°, and 80° fields; **(b)** zoomed-in images of the four marked regions captured with the original full-resolution image displayed on the monitor; **(c)** zoomed-in images of the four marked regions captured with the statically foveated image displayed on the monitor; **(d)-(f)** perceived images of the four marked regions by a 20/20 standard observer, simulated from the captured zoom-in full-resolution image for the eye gaze angle of 0°, 15°, and 30°, respectively.

3.4.2 Quantitative assessment and validation

Two experiments were conducted to assess the image quality of the proposed foveation scheme. The first experiment validated the resolution distribution function described by Eq. (9) by measuring the foveated display's resolution distribution. In the second experiment, the perceived display resolution was measured as a function of the eye gaze angle. Both experiments used two sets of small full-resolution bar targets orientating vertical and horizontal directions and covering approximately 10° field angles. Foveated images were rendered from these targets for selected field positions. A 50-mm focal length lens on a camera was used to capture zoomed-in views of the foveated targets displayed on a 4K monitor for varying field angles.

To evaluate the resolution distribution of the foveated display, the slanted-edge method was used to measure the MTFs. We rendered horizontal or vertical bar targets on the monitor and rotated the monitor to simulate the slanted edge effect. 23 fields were sampled along the diagonal direction of the display, from 5° to 80° with varying increments to account for varying resolution degradation rate. The foveated images were generated by applying Gaussian-type convolution filters, based on the angular magnifications of the fields. To ensure accurate measurement of the resolution distribution of the foveated display, the camera was positioned perpendicular to the display and centered with each sampled field. The captured slanted edge images were analyzed to determine the MTFs in both horizontal and vertical directions. The MTF measurements were converted to the display space by considering the optical magnification between the camera and monitor pixels. The resulting MTF curves of the foveated display in the horizontal direction for 13 sampled fields were plotted in Fig. 3.12(a), showing a decrease in MTF as field angles increased, except for the 5° and 10° fields which maintained higher MTF values corresponding to the fovea

region. Similar results were observed for the vertical direction. To recover the resolution distribution function from the corrected MTF curves, a threshold value of 0.89 at Nyquist frequency of the monitor, as 60 cycles/degree, obtained from the 5° zoomed-in view was used to determine the limiting resolutions for different field angles. The MTF degradation from this threshold value represented the impact of the foveation scheme. Fig. 3.12(b) displayed the resolution distributions of the foveated display in both horizontal (*) and vertical (Δ) directions, respectively. These distributions showed excellent agreement with the theoretical foveation scheme.

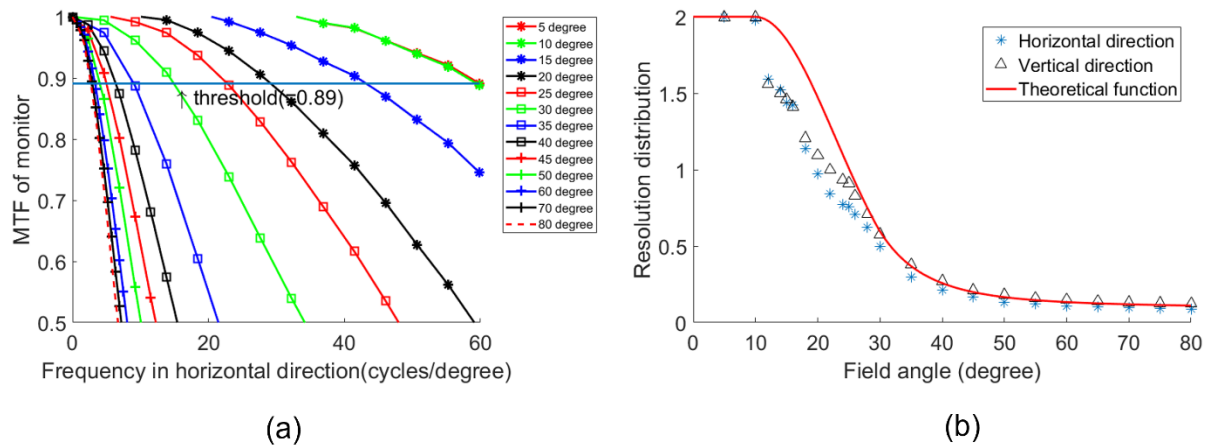


Fig. 3.12 (a) MTF curves of foveated display in horizontal direction as a function of spatial frequencies in cycles/degree for 13 different field angles; (b) The resolution distribution of the foveated display measured in the horizontal and vertical directions.

Different from the previous experiment, to simulate different gazing directions for a standard observer of 20/20 vision, each sampled field position was repeatedly measured at various camera viewing angles. The captured images were convolved with a foveation filter, mimicking the visual acuity of a 20/20 observer characterized by Eq. (1), for MTF analysis that mimicked the sampling effects by a human eye. The field sampling and foveated images rendering method are in the same

way as the first experiment. We captured images at 8 different camera viewing angles (5° to 40° with a 5° interval) for each field position. To ensure accuracy, we adjusted the target image positions on the monitor instead of the camera orientation. This process was repeated for both horizontal and vertical bars across all sampled fields and viewing directions, resulting in a total of 368 images. For each viewing angle, the capture and analysis process described above is repeated. Fig. 3.13 shows the perceived resolution distributions as a function of field angles for 4 eye gaze angles (10° , 20° , 30° , and 40°) denoted by *, Δ , +, and O, respectively. The figure includes the theoretical resolution distribution of the foveation scheme represented by red dashed lines, as well as the theoretical perceived resolution distributions calculated using Eq. (3) for the four eye gaze angles. The experimental measurements of the perceived resolution distributions align closely with the theoretical results.

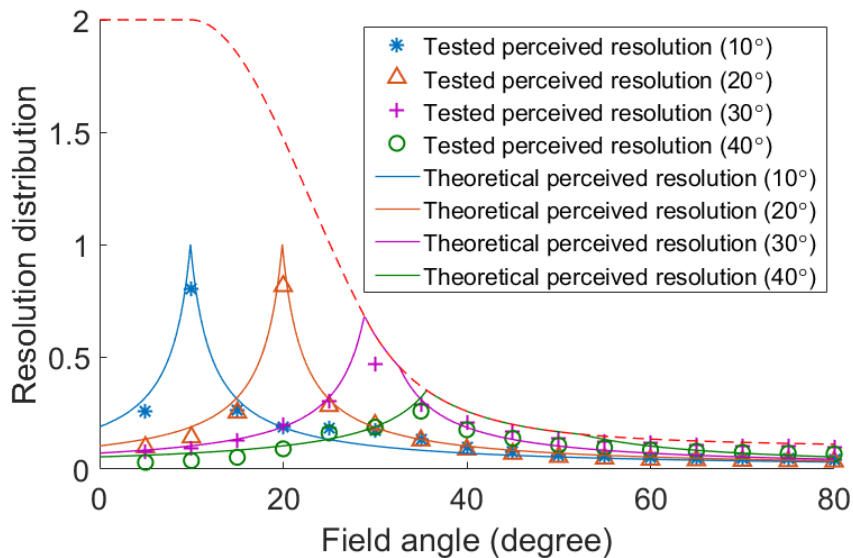


Fig. 3.13 Quantitative assessment of the perceived resolution distributions as a function of field angles for four different viewing angles, 10° , 20° , 30° and 40° .

4. DESIGN OF A STATICALLY FOVEATED IMMERSIVE HMD

The perceptual driven approach discussed in Chapter 3 was used to design a statically foveated immersive HMD. This chapter demonstrated the design and optimization process of the statically foveated display, along with a novel method to evaluate the perceived optical performance by incorporating the Arizona eye model. A prototype is implemented to evaluate the perceived performance. A full description of the study, including in-depth procedures and results, can be found in the published work [44], which is included in APPENDIX B.

4.1 SYSTEM OVERVIEW

To design a statically foveated HMD system with spatially varying angular resolution, one direct approach is to use a display that has varying pixel density to match the desired resolution distribution function of a foveation scheme. However, manufacturing displays with such varying pixel density is challenging. Alternatively, a statically foveated display can be achieved by applying display panels with uniform pixel density and designing an eyepiece that provides spatially varying optical power. This ensures that the angular resolution distribution of the virtual display seen through the eyepiece aligns with the foveated scheme. The spatially varying optical power of an eyepiece, Φ_{EP} (or eyepiece focal length f_{EP}), can be calculated based on the resolution distribution function and defined as

$$\Phi_{EP}(\theta_x, \theta_y) = \frac{1}{f_{EP}(\theta_x, \theta_y)} = \frac{\tan\left(\frac{1}{60 \cdot F_{FD}(\theta_x, \theta_y)}\right)}{p_0 \cos^2 \theta}, \quad (10)$$

where the p_0 is the pixel pitch of a uniform-resolution display.

Based on the resolution distribution function depicted in Eq. (9), we plotted the number of required pixels as a function of the FOV for three different peak resolutions of 1, 1.5, and 2 arcminutes per pixel, respectively, as Fig. 4.1. Considering factors such as display size, design complexity, and pixel count, the choice for the display panel fell upon a smartphone (Sony Xperia XZ2 Premium). This particular smartphone was selected due to its compact pixel pitch and sufficient pixel count, which has a diagonal size of 147 mm and a total resolution of 3840 x 2160 pixels. However, to accommodate the interpupillary distance of human eyes, only a portion of the display area was utilized, measuring approximately 60mm horizontally and 60mm vertically. This region corresponded to a resolution of 1820 x 1820 pixels. The selected display configuration allowed for a foveated display with an 80° diagonal field of view (FOV) and a peak angular resolution of 1.5 arcminutes per pixel.

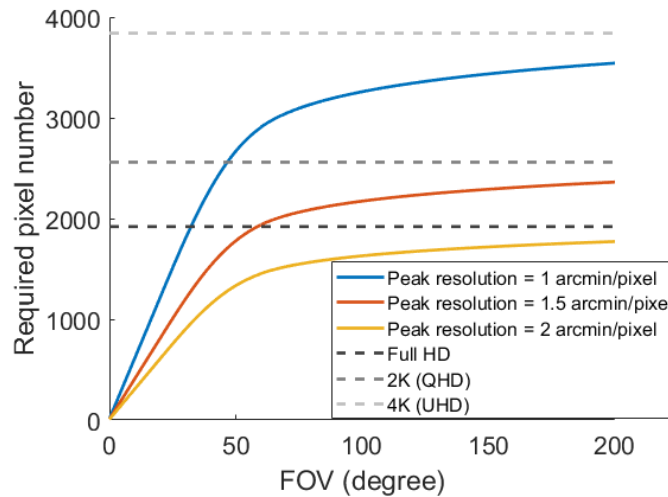


Fig. 4.1 The required pixel number of a foveated display as a function of the overall FOV in a given direction for three different peak resolutions of 1, 1.5, and 2 arcminutes per pixel, respectively.

The overall specification of the foveated display is listed in Table 4.1. The eyepiece design considerations for the HMD system included setting the exit pupil diameter at 8 mm to

accommodate the limited eye movement range for eye pupil sizes ranging from 2 to 4 mm. Additionally, an eye relief of at least 18 mm was chosen to accommodate standard eyeglasses. The target diagonal FOV was set to 80°. To optimize the design, the total number of optical elements in the eyepiece was limited to no more than five, with a preference for stock lenses to minimize fabrication costs. It was anticipated that at least one of the elements would be an aspherical lens capable of varying the optical power as a function of the fields.

Table 4.1 The specification of the foveated display.

	Parameters	Specifications
Display	Active panel size	< 3.33in. diagonally (60mm horizontally and 60mm vertically)
	Active pixel resolution	1820 x 1820 pixels
	Pixel pitch	0.033 mm
Optical system	Exit pupil diameter	8 mm
	Eye relief	≥ 18 mm
	Number of elements	≤ 5
	Wavelength	480 - 625 nm
	FOV	80° diagonally, $\sim 56.5^\circ$ (H) * $\sim 56.5^\circ$ (V)
	Vignetting	< 0.3 for the edge fields ($\pm 40^\circ$)
	Image quality	MTF > 10% at 15 cycles/mm

4.2 OPTIMIZATION METHOD

Initially, we started with a design with all spherical lenses, and a preliminary configuration of three spherical lenses was obtained based on the first-order calculation to guarantee an angular resolution of 1.5 arcminutes per pixel in the central region of the display. Then, an aspherical lens was positioned near the display panel as a field lens to enable control over spatially varying optical power. The reason for the choice of the mentioned placement of the aspherical lens is because of minimal interaction between ray bundles from adjacent fields, resulting in more effective control

over optical power and aberrations. Throughout the design process, the resolution distribution was calculated by the chief ray heights traced in software at the display panel across various field angles. When the field sampling is adequately dense to ensure a negligible difference between adjacent fields, the resolution distribution at θ field angle is expressed as:

$$F(\theta) = \frac{h_c(\theta + \Delta\theta) - h_c(\theta)}{p_0 \times \Delta\theta}, \quad (11)$$

where the $h_c(\theta)$ is the chief ray height at the display panel for θ° field, and $\Delta\theta$ is sampling interval of field angle, which was set to 0.1% of the full FOV.

In the design software, the optical power as function of the field angle can be calculated by employing Eq. (10) and Eq. (11). And the ray-tracing data obtained through Eq. (11) were used to create user-defined constraints for lens optimization. Due to the impracticality of constraining the optical power distribution with large samples, a progressive optimization approach was employed. The optimization process began with loose controls of optical power constraints at two critical field angles, 10 and 30 degrees, using low-order polynomial parameters for the aspheric surfaces. As up to 8th higher-order parameters were introduced for aspheric lens, these constraints were gradually tightened to match their target values. Additional weak constraints were added at intermediate fields, determined by the resolution distribution curve obtained during optimization. However, it is significantly challenging to achieve a large range of optical power variation within a single eyepiece to match the angular resolution distribution in Eq. (9). For a statically foveated display with 40° half FOV, the desired optical power difference between the center and edge fields was substantial, over 7.5 times. Considering only one aspherical field lens applied, it was feasible to achieve an optical power ratio of approximately 3 times to preserve the high perceived

performance. To reduce the requirement for optical power range while maintaining the same FOV and peak angular resolution of 1.5 arc minutes per pixel, additional pixels on the display panel were utilized. Although this slightly reduced data sampling efficiency, it was expected to enhance perceived performance within the parafovea and peripheral regions.

4.3 PERFORMANCE ANALYSIS

The 2D layout of the finalized eyepiece design, including three stock lenses and one aspherical lens, is illustrated in Fig. 4.2, where 30% vignetting was introduced for the edge field due to the clear aperture limitation of the stock doublet lens (third lens from the left).

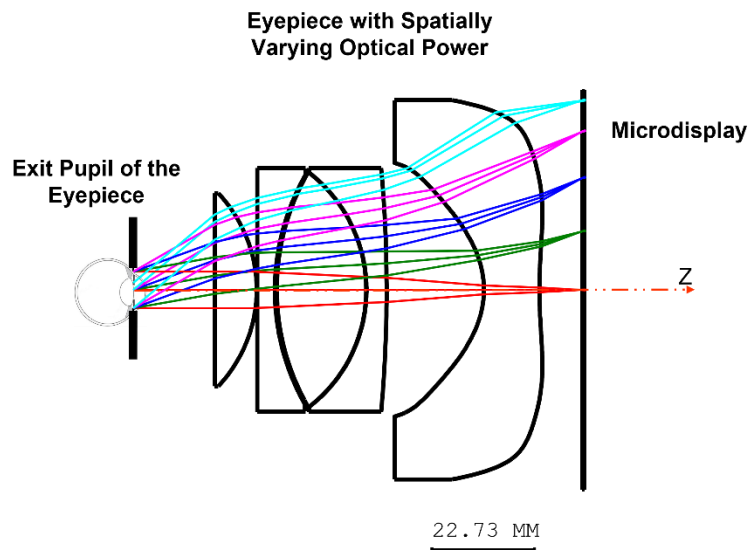


Fig. 4.2 The layout of eyepiece for the statically foveated display.

4.3.1 Normal performance analysis

The plots of MTF were examined to evaluate the performance, as shown in Fig. 4.3, for three different eye positions within the exit pupil: center, up 2 mm, and down 2 mm, respectively. These plots assume a 4-mm eye pupil. With the exception of the edge fields, the MTF values for almost all fields exceed 0.2 at the cut-off frequency, which is determined based on the pixel pitch of the

center field. However, given the spatially varying optical power of the eyepiece in the foveated eyepiece design, the adoption of this common practice is less indicative for the perceived optical performance. The cut-off frequency changes as the effective pixel pitch, which varies spatially as the function of field angles.

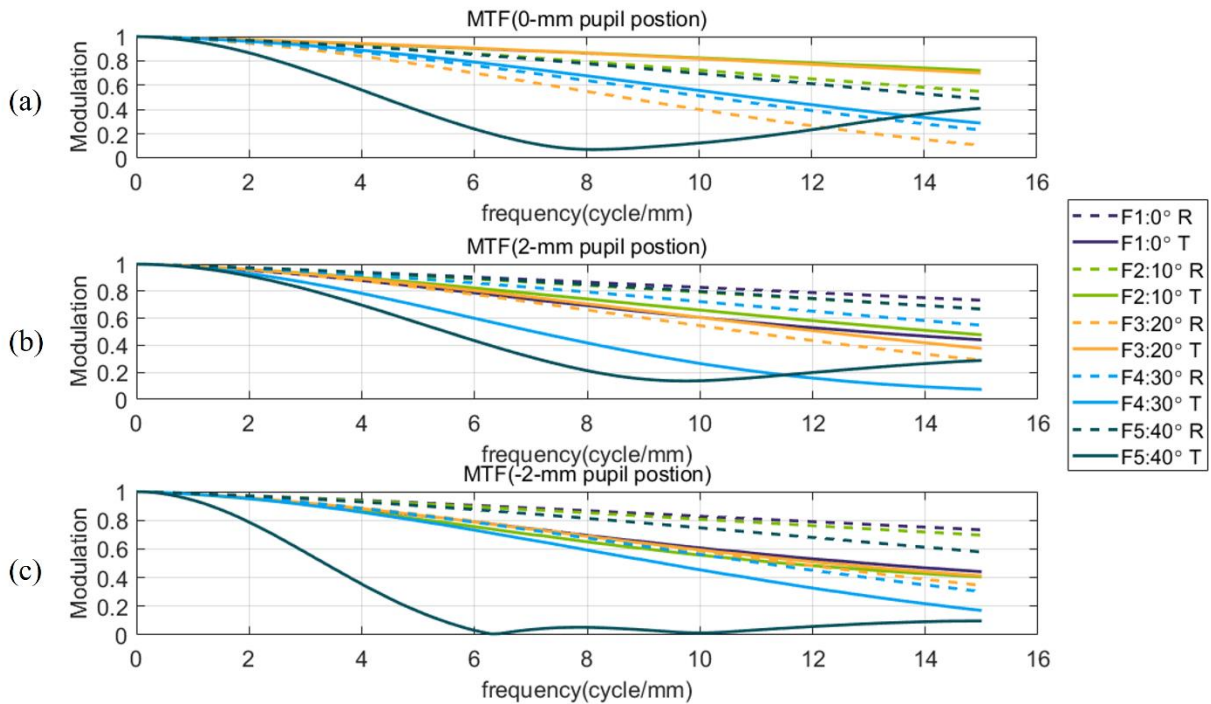


Fig. 4.3 MTF plots for different eye position with 4-mm pupil size. (a) MTF plot when eye is located in the center of the eyebox. (b) MTF plot when human eye moves up 2 mm. (c) MTF plot when human eye moves down 2 mm.

4.3.2 Perceived performance assessment through a reversed system integrated with Arizona eye model

For the analysis of the perceived performance in the visual space, we employed a reversed layout approach. By flipping the optical system shown in Fig. 4.2, we traced rays from the display to the exit pupil. Additionally, we inserted the Arizona eye model at the exit pupil. The reversed layout

is illustrated in Fig. 4.4, where the display panel is treated as the object with uniform spatial sampling, and the retina of the eye model serves as the image plane. The Arizona eye model's entrance pupil, situated 3.05 mm from the cornea, coincides with the exit pupil position of the foveated eyepiece. Two examples of the system setup are illustrated in Figures 4.4(a) and 4.4(b), corresponding to the eye model rotated by 0° and 30° , respectively, where the Arizona eye model is rotated around its rotation center, located 13 mm behind the corneal vertex.

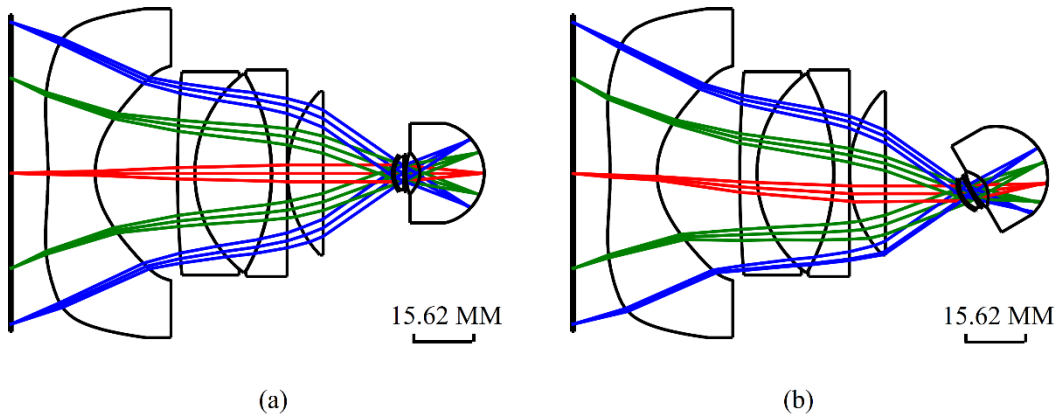


Fig. 4.4 The layout of the reserved system with Arizona eye model: (a) eye gaze at 0° ; and (b) eye gaze at 30° .

The perceived performance of the static foveated display was assessed by rotating the Arizona eye model from 0° to 30° at 5° intervals. To make a comparison with the HVS, the unit of spatial frequency was converted to cycles per degree in the visual space, and field types were converted to field angles incident upon the eye pupil based on ray trace data instead of the object height at the display panel. The designed peak angular resolution of 1.5 arcminutes per pixel corresponds to an effective pixel size of $7.2 \mu\text{m}$ on the human retina, resulting in an MTF cut-off frequency of approximately 20 cycles per degree or 69.5 cycles per millimeter on the retina. Figures 4.5 (a) through (d) plot the MTF curves of the foveated display when the Arizona eye model is rotated at 0° , 10° , 20° , and 30° , respectively. Each plot includes five sampled fields covering the FOV of the

display: 0° , $\pm 20^\circ$, and $\pm 35^\circ$, in which these fields correspond to the central zones of the fovea, parafovea, and peripheral regions, respectively. The MTF values for negative field angles, as -20° and -35° , represented by dashed lines in Figs. 4.5(b) and 4.5(c), remain similar to the 0° field for eye gaze angles up to 20° . Despite a 30° eye movement as illustrated in Fig. 4.5(d), the MTF values for negative fields maintain a level above 20% for frequencies up to 15 cycles per degree. These findings indicate that the foveated display can deliver high image contrast even for eye movements of up to 30° . While the MTF values for positive field angles displayed as solid lines are lower compared to the 0° field, it is important to note that these fields fall within the peripheral region of the HVS.

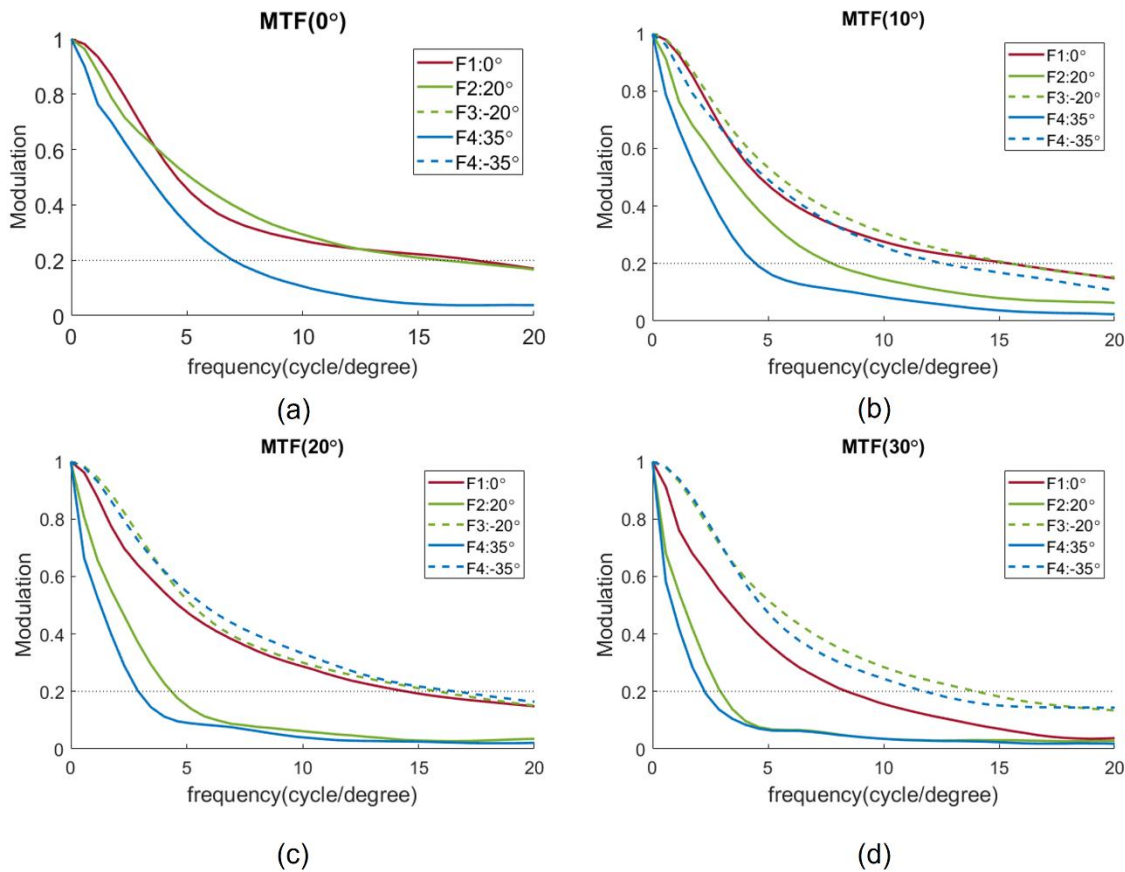


Fig. 4.5 MTF plots for various fields with the rotation angle of Arizona eye model part: (a) 0°; (b) 10°; (c) 20°; (d) 30°.

To assess the perceived limiting resolution distribution of the foveated display under different eye rotation angles, the average MTF values were calculated in both the tangential and radial directions for each sampled field angle. For a given rotation angle, the perceived limiting resolution for each field angle was determined by identifying the maximum angular frequency on the MTF curve where the MTF value reaches a contrast modulation threshold of 20%. The modulation threshold was chosen considering the HVS's contrast sensitivity function, which enables the detection of fine details at cut-off frequencies up to 20 cycles per degree. Figures 4.6(a) to 4.6(d) depicted the perceived limiting resolution distributions of the foveated display for different eye rotation angles, 0°, 10°, 20°, and 30°, respectively, as a function of the display field angle, in which the VA curve described as Eq. (1) is also overlaid for reference aligned with the corresponding gaze direction. Based on Figs. 4.6(a) through 4.6(c), for eye rotation angles up to 20°, the foveated display achieves a peak resolution of approximately 60% compared to a standard observer, corresponding to an angular resolution of about 1.5 arcminutes per pixel. The perceived limiting resolution of the foveated display exceeds the visual acuity of a standard observer throughout the field of view, except a small region near the gaze direction. At around 30° eye gaze illustrated as Fig. 4.6(d), the peak resolution decreases to around 40% of a standard observer's VA, with a slight deviation of approximately 10° that is caused by the limitations of Arizona eye model. However, the perceived limiting resolution still surpasses the visual acuity of a standard observer within the -25° to 40° field region. In summary, the static foveated display demonstrates adequate perceived performance without the need for dynamic tracking and scanning devices, particularly within the $\pm 20^\circ$ region of frequent eye movements.

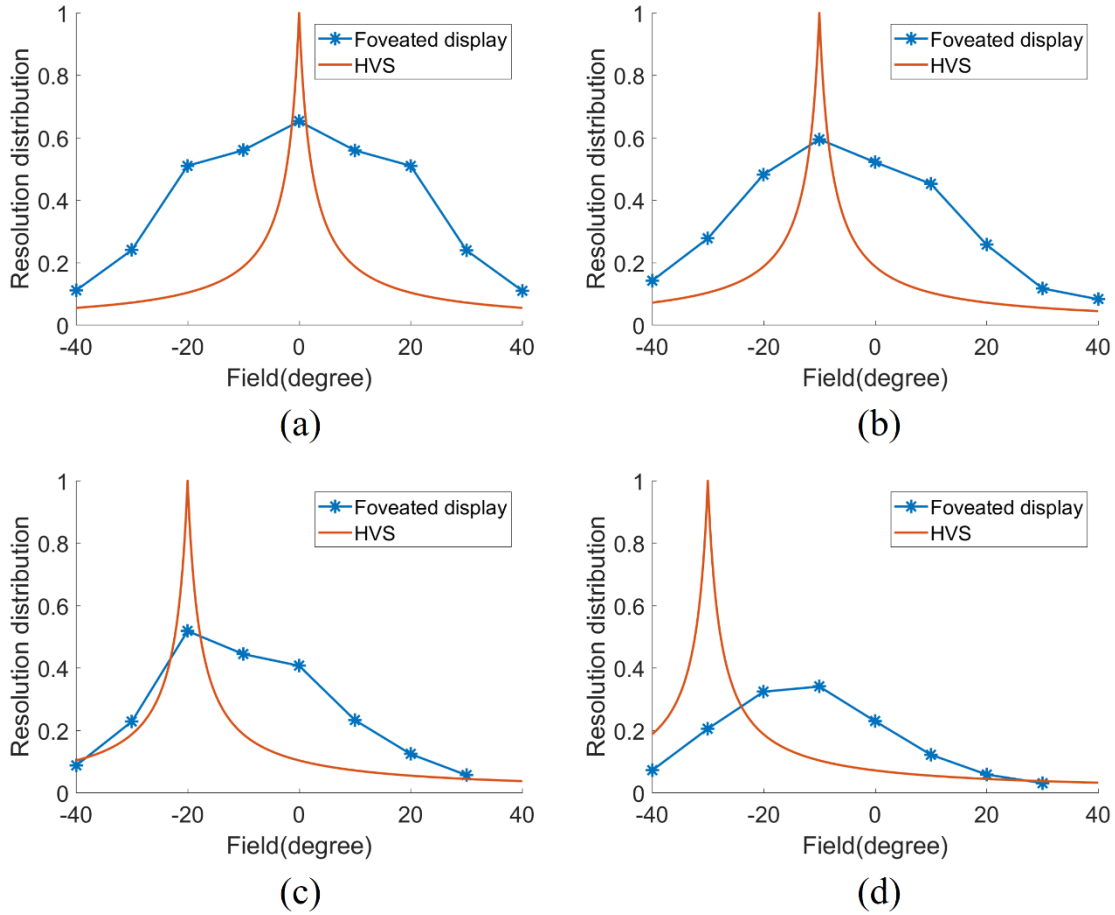


Fig. 4.6 The resolution distributions of the foveated display as the function of the field angle with the eye rotation angle of (a) 0° ; (b) 10° ; (c) 20° ; (d) 30° , respectively.

4.3.3 Resolution distribution map

Figure 4.7 (a) demonstrates the distortion grid of the foveated display at the display plane with a 21×21 grid field sampled. To compute the resolution distribution using Eq. (11), we performed ray tracing for one million chief rays, sampled at a 0.08 -degree interval across an 80 -degree square FOV. Figure 4.7 (b) presents the resolution distribution map throughout the virtual display plane. Figure 4.7(c) further depicts the resolution distribution as a function of the field angle along the diagonal direction, with the target resolution distribution shown as a dashed line for comparison.

The resolution degradation rate aligns with our design objective, remaining relatively constant within the foveated region and gradually declining at a faster rate as the field angle increases. In Fig. 4.7(d), the number of pixels in the diagonal direction is plotted as the function of FOV for the designed foveated display, derived from the resolution distribution curve. The total pixel count required for an 80-degree FOV in the diagonal direction is approximately 2340, which considerably reduces the display panel requirement compared to a rectilinear sampling display.

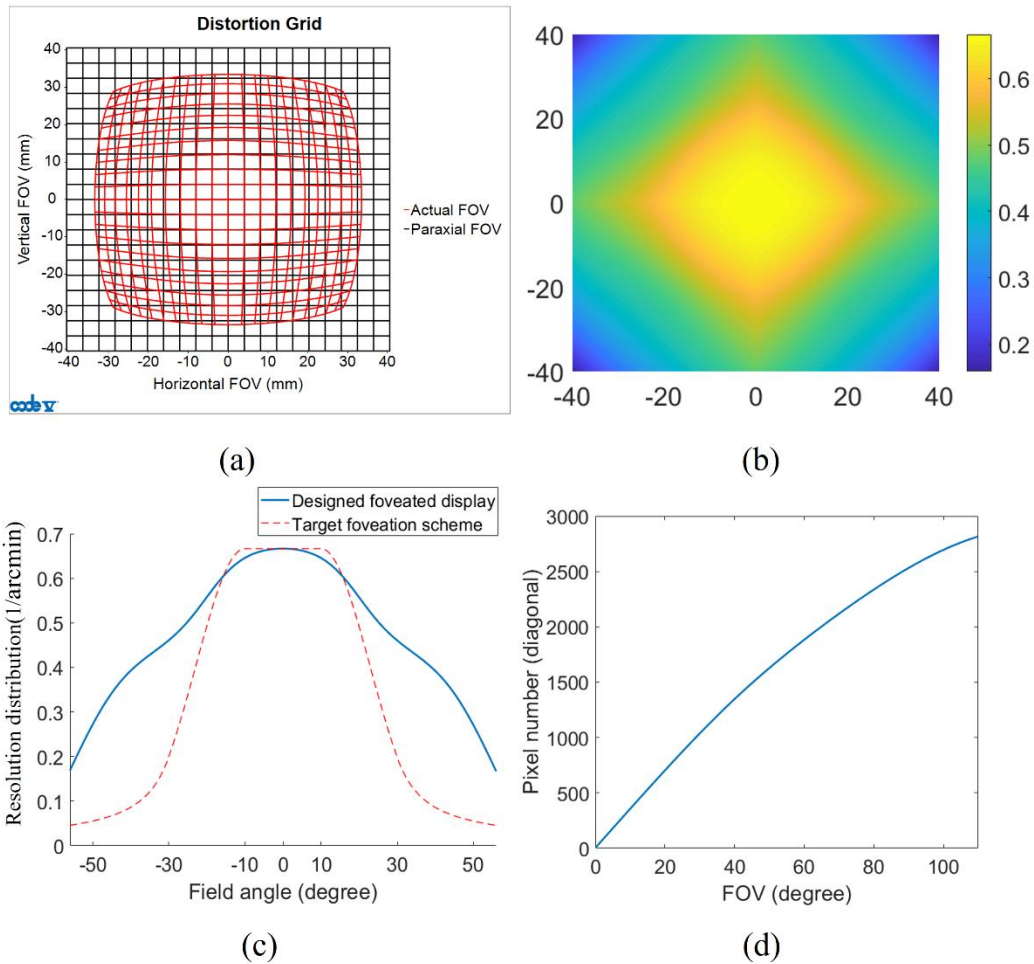


Fig. 4.7 (a) The distortion grid of designed foveated display; (b) The resolution distribution in field map; (c) the resolution distribution of designed foveated display and a target foveation scheme as the function of the field along the diagonal direction; (d) the pixel number in diagonal direction as a function of the FOV for designed foveated display.

4.3.4 Tolerance analysis

Considering the optical fabrication, alignment, and cost issue, the tolerance analysis of the statically foveated display was evaluated based on the tolerance values listed in Table 4.2.

Table 4.2 Tolerance items.

Tolerance Type	Location	Value	Unit
DLR—delta radius	S_2 - S_{10}	$\pm 0.3\%$	--
DLS—delta sag at clear aperture	S_2 - S_{10}	± 0.05	mm
DLF—delta sag at clear aperture	S_9, S_{10}	2	--
IRR—cylindrical irregularity in fringes	S_2 - S_{10}	1λ	--
DLX—surface X -displacement	S_2 - S_{10}	0.1	mm
DLY—surface Y -displacement	S_2 - S_{10}	0.1	mm
DLZ—surface Z-displacement	S_2 - S_{10}	0.1	mm
DLN—refractive index delta	S_2, S_4, S_6, S_7 and S_9	0.001	--
DLV—Abbe-number delta	S_2, S_4, S_6, S_7 and S_9	0.008	--
TIR—total indicated reading	S_2 - S_{10}	0.04	mm
DIS—group displacement	S_{2-3} , and S_{4-8}	0.01	mm
	S_{9-10}	0.02	mm
BTI—group barrel tilt in radians	S_{2-3} , and S_{4-8}	0.015	radians
	S_{9-10}	0.05	radians
CMP DLT—compensator: image plane position	S_l	--	mm

The tolerance analysis was conducted through 50,000 Monte Carlo simulations for each case. Figure 4.8 illustrates the sensitivity analysis of tolerances in MTF values at the Nyquist frequency for various eye pupil locations with a 4-mm eye pupil size. The results indicate that the designed statically foveated display exhibits high stability according to commercial manufacturing specifications.

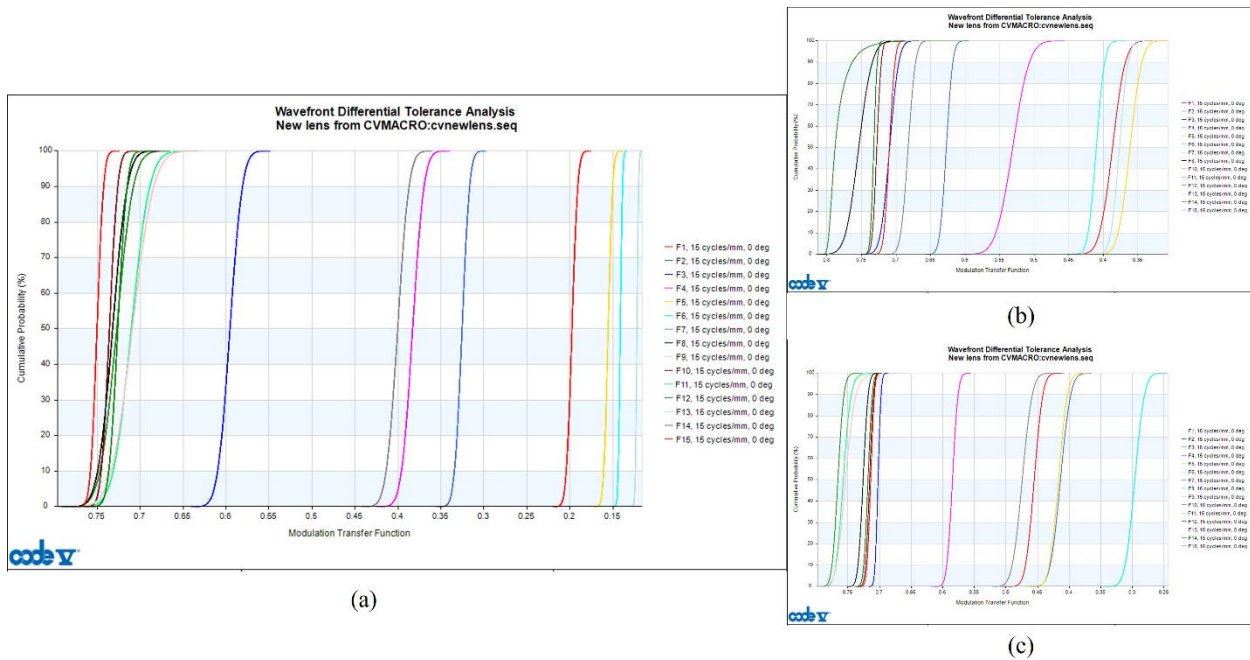


Fig. 4.8 The foveated display MTF tolerancing results at Nyquist frequency with 4-mm eye pupil size (a) when eye locates in center of eyebox; (b) when human eye moves up 2 mm; (c) when human eye moves down 2 mm.

4.4 PROTOTYPE AND PERFORMANCE EVALUATION

The three stock lenses data and the customized aspherical lens data are presented in Table 4.3 and Table 4.4, respectively. Based on the lens shape and size information, the eyepiece mount for the prototype was designed, as depicted in Fig. 4.9.

Table 4.3 Stock lenses data.

Lens brand	Lens stock number	Effective focal length	Radius R_1	Glass1	Radius R_2 (R_3)	Center thickness
Edmund	Stock #45-150	40 mm	Infinity	N-BK7	-31.03 mm	9.31 mm
Thorlabs	LC1093-A	-100 mm	Infinity	N-BK7	51.50 mm	4 mm
Edmund	Stock #49-291	75 mm	51.88 mm	N-BAF10	-32.79 mm	20 mm
			--	N-SF10	-309.45 mm	4.5 mm

Table 4.4 Aspherical lenses data.

Coefficients	Comment	Front surface (mm)	Rear surface (mm)
R	Radius	-20.26103943	111.20650840
k	Conic number	-0.50200021	-36.55525701
A	4 th -order parameter	8.19668027e-006	-3.37952689e-006
B	6 th -order parameter	5.42668346e-009	-1.11635600e-008
C	8 th -order parameter	1.78601819e-011	1.54186620e-011
D	10 th -order parameter	-8.38642508e-015	-5.96525291e-015

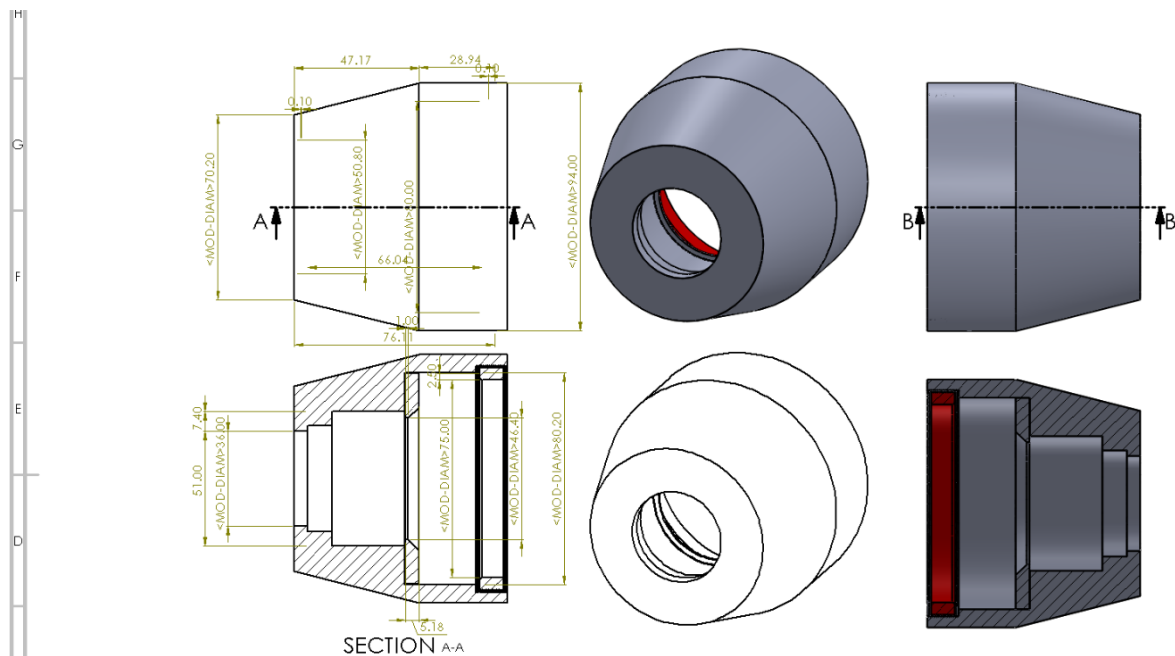


Fig. 4.9 The schematic diagram of mount design for the design eyepiece.

A photograph of the test prototype is displayed in Fig. 4.10 (a), where a 2K camera located at an anticipated viewing position was to simulate the human eye and capture images through optics. The display panel consisted of a Sony cellphone (Sony Xperia XZ2 Premium) with a diagonal size of 147 mm and a total of 3840 x 2160 pixels. The prototype system generated an 80-degree circular FOV for the captured images. A 4K-resolution image was generated, comprising modified USAF 1951 targets arranged in a 17 by 9 grid, as depicted in Fig. 4.10 (b). Each sub-image in Fig. 4.10 (c) contained the elements from Groups 2 and 3. For more detail, we have described it in paper

[44]. The 4K image covers an 80° by 40° FOV in the horizontal and vertical directions, respectively. Figure 4.11 (a) presents an image captured by the 2K camera equipped with an 8-mm focal length lens. The spatially varying optical magnification of the eyepiece is evident considering the non-uniform arrangement of the sub-images. To evaluate the optical performance at different field positions, a 50-mm lens replaced the 8-mm camera lens so that the camera is able to resolve spatial details as high as xx/pixel . Figs. 4.11(b) to 4.11 (d) depict the captured images corresponding to the camera pointing towards 0° , -20° , and -35° of the display fields horizontally. Within the $\pm 15^\circ$ region, as shown in Figs. 4.11(b) and 4.11(c), the display exhibits excellent optical performance, which is the area for frequent eye movements. Notably, the native 4K resolution image could not be displayed faithfully on the Sony cellphone due to the panel limitations. To emulate 4K resolution, the display was forced to scale down a 4K image to 1080p before enlarging it to 4K using the Android Debug Bridge method, resulting in additional blur or misalignment.

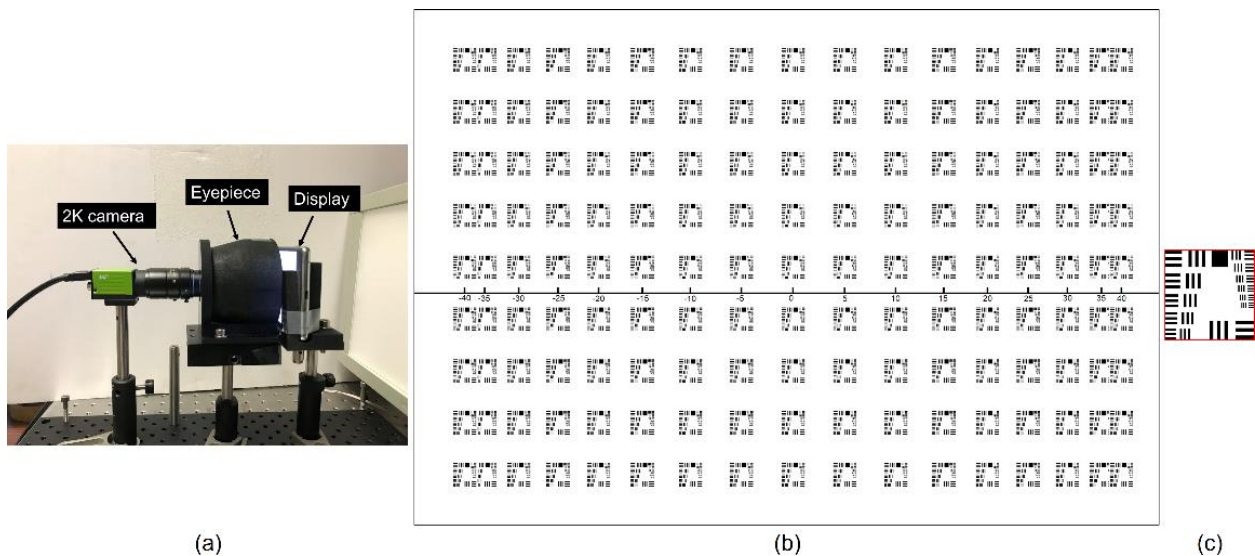


Fig. 4.10 (a) Prototype of the static foveated display with cellphone display panel; (b) The input image displayed on the cellphone screen; (c) Zoomed sub-image for the modified USAF target.

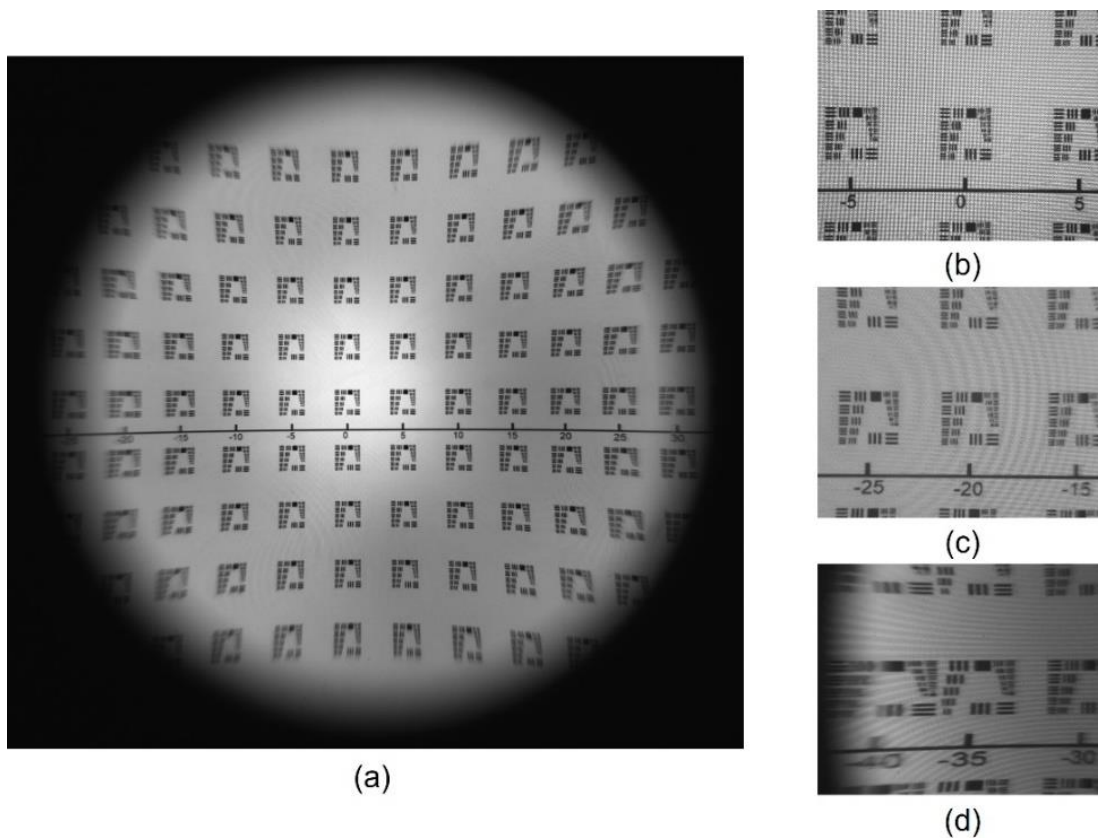


Fig. 4.11 (a) Captured image by 2K camera with 8-mm focal length camera lens; Captured image by 2K camera with 50-mm focal length camera lens when the camera was towards (b) 0° , (c) -20° , and (d) -35° of the field angle of display, respectively.

For accurate optical performance evaluation, we used the slanted edge method with Imatest® software to measure the system MTF curves. Instead of using the Sony display panel, we employed a transparent high-resolution target (USAF 1951 Target) illuminated by an LED backlight (Fig. 4.12(a)). An example of the captured images was shown in Fig. 11(b) which shows the slanted edge aligned with the center of the eyepiece FOV. The zoomed-in image within the red rectangle was used for MTF measurements. We utilized a 2K camera with a 25-mm focal length lens, providing an angular resolution of 0.69 arcminutes per pixel, more than twice the peak resolution of the foveated display to ensure sufficient image contrast and resolution at the Nyquist frequency

of 20 cycles/degree. To simulate horizontal eye movement, we rotated the camera while maintaining the target's height, ensuring the measured edge remained in the same position within the camera's view. The camera direction and target position were aligned with a printed transparent field coordinate reference label in front of the high-resolution target, shown as Fig. 11(b).

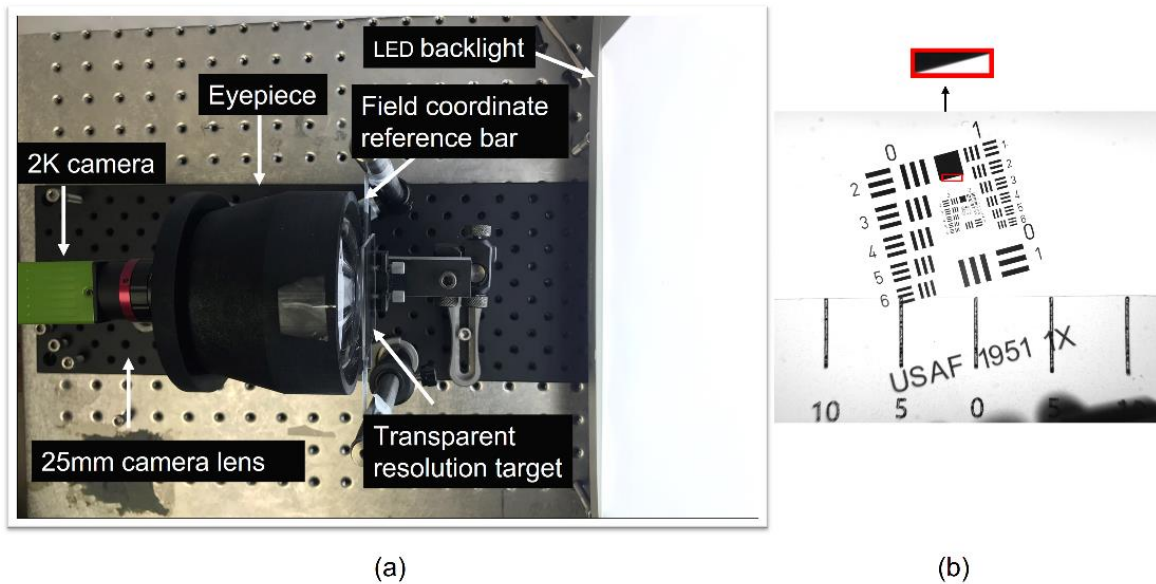


Fig. 4.12 (a) Prototype of the static foveated display with transparent high-resolution target; (b) The captured image of high-resolution target for straight view direction.

Nine fields were captured in the image space from 0° to 40° at 5° intervals. To account for the camera sensor's sampling frequency, we converted these frequencies from the camera sensor space to angular frequencies in the display space by applying the optical magnification factor. Fig. 4.13(a) shows the MTF plots as a function of the converted frequency in the display space, which closely match the simulated MTF of the eyepiece design in CODEV. The MTF curves gradually decrease as the field angle increases.

To construct the resolution distribution based on the MTF curves in Fig. 4.13(a), we used a threshold value of 0.64 at 20 cycles/degree from the 0° MTF plot. This threshold represents the

combined modulation of the resolution target caused by the eyepiece and camera sampling effects at the Nyquist frequency, serving as the inherent resolution limit of the testing system. By comparing the other eight MTF plots with non-zero field angles to this threshold, we determined the limiting resolutions. Fig. 4.13(b) displays the graph of the limiting resolution distribution function as a function of field angles, resembling the simulated distribution obtained in CODEV.

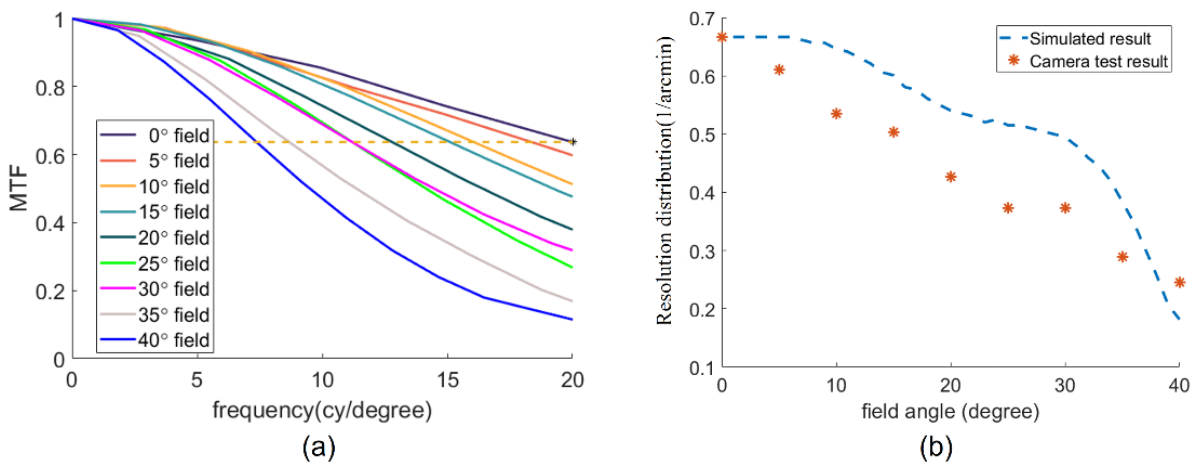


Fig. 4.13 (a) MTF curves of foveated display in horizontal direction as a function of spatial frequencies in cycles/degree for 9 different field angles; (b) The resolution distribution of the foveated display measured in the horizontal direction.

5. STATICALLY FOVEATED FREEFORM OST-HMD SYSTEM WITH LARGE FOV

After designing the statically foveated immersive HMD in Chapter 4, we also applied this approach to design a statically foveated OST-HMD system with three freeform wedge-shape prisms to achieve a large FOV and high perceived performance within the region of frequent eye movements. This chapter explained the design and optimization method of the statically foveated OST-HMD system. Performance simulations, tolerance analysis, and housing design are also discussed in this Chapter.

5.1 SYSTEM OVERVIEW

The design of an OST-HMD system requires the choice of a proper optical combiner which merges the optical paths of virtual image display and real-world view. Though there are several choices of optical combiner techniques, from a simple planar beamsplitter to a sophisticated holographic waveguide combiner, few of these combiners support large FOV, compact dimensions, and high optical performance. After considering various tradeoff factors, we chose to utilize a freeform waveguide combiner for a statistically foveated OST-HMD design [9, 45–47].

The system's overall specifications are provided in Table 5.1. To meet the requirements for a minimal interpupillary distance (IPD) of 55 mm and desired optical performance, we opted for a 2-inch display with a resolution of 1920 x 1840 pixels and a pixel pitch of 20 μm . The active area utilized was 1920 x 1230 pixels, corresponding to a size of 38.4 mm x 24.6 mm. In order to accommodate the range of eye movement for eye pupils ranging from 2 to 4 mm especially considering without eye tracking device, the exit pupil diameter of the eyepiece was increased to

10 mm compared with our previous design described in Chapter 4. The eye clearance was set to be greater than 15 mm, and the FOV target covered $\pm 35^\circ$ horizontally and from $+25^\circ$ to -15° vertically, resulting in an approximate diagonal FOV of 80 degrees.

Table 5.1 The overall specifications of the system.

	Parameters	Specifications
Display	Active panel size	38.4 mm x 24.6 mm
	Active pixel resolution	1920 x 1230 pixels
	Pixel pitch	0.02 mm
Optical system	Exit pupil diameter	10 mm
	Eye relief	≥ 15 mm
	Material of freeform prism	COP
	Wavelength	480 - 625 nm
	FOV	80° diagonally, $\sim 70^\circ$ (H) * $\sim 40^\circ$ (V)
	Vignetting	No
	Image quality	MTF $> 10\%$ at 27 cycle/mm

We started the design process by adopting the well-established monolithic freeform wedge prism structure as the main eyepiece attached with an auxiliary freeform prism or the so-called compensator for the see-through optical path. Although we were able to obtain an eyepiece design that satisfies the overall specifications in Table 5.1 and achieves the desired optical power variation for a statically foveated scheme, due to the challenges posed by the large exit pupil and wide FOV, we encountered significant difficulties in achieving high-quality see-through images when attempting to design an auxiliary freeform prism for the see-through path. We observed that the tilt angle of the first surface of the main freeform prism was too steep for satisfactory results of see-through view, especially for keystone effect. To address this issue and minimize see-through distortion, we drew inspiration from Dewen's work [47] which introduced another auxiliary lens

between the main prism and the human eye, creating a sandwich structure as depicted in Fig. 5.1. In this structure, the optical system is composed of three elements, the main wedge prism E2, the first auxiliary lens E1 attached to the front surface of the main prism, and the second auxiliary lens E3 attached to the back surface of the main prism. The combination of E1 and E2 serves as the optical system for the virtual display path, while the combination of E1, E2, and E3 serves as the optical system for the see-through light path.

Like a conventional wedge-shaped freeform eyepiece design, the main prism E2 comprises three optical surfaces, S3-S3', S4, and S5. The surface S4, facilitated by a half-mirror coating, serves as the combining surface for the paths of virtual display and see-through view. The first auxiliary lens consists of two optical surfaces, S1 and S2, where S2 preferably shares the same optical prescription as S3-S3'. The second auxiliary lens consists of two optical surfaces, S4' and S6, where S4' preferably shares the same optical prescription as S4.

In the virtual display path, the light rays emitted from the display panel undergo a first refraction at surface S5. Subsequently, two consecutive reflections occur at surfaces S3' and S4, with a total internal reflection taking place at surface S3' and a reflection being caused by the half-mirror coating at surface S4. The reflected light rays then are refracted by surface S3 and are directed toward the first auxiliary prism. Following two consecutive refractions by S2 and S1 of the prism E1, the light rays originated from the display panel finally reach the exit pupil, while a viewer's eye is located for observing the virtual image. A small air gap is required between elements E1 and E2 to maintain the total internal reflection for the reflection on the S3' in the display path.

In the see-through path, the light rays from a real-world scene are propagated by a sequence of refractions through the surfaces of elements E3, E2, and E1. The first and second auxiliary prisms, positioned on either side of the main freeform prism, form a plane parallel plate ensuring an undistorted see-through view of the real scene. This 3-element sandwich structure not only mitigates distortion to see-through view but also offers potential capabilities for vision correction. For users with normal vision, the optical surfaces S1 and S6 can remain flat to ensure excellent see-through performance and minimal distortion. However, for users with myopia or hyperopia, the curvature of optical surface S1 can be adjusted to accommodate different diopter correction requirements. In such cases, the curvature of S1 can be modified to be negative or positive to address the specific needs of individual users. In the meantime, surface S6 can be optimized to minimize both shift and distortion of the real-world scene. In summary, the first auxiliary freeform prism can serve as a vision correction insert lens, eliminating the need for additional eyeglasses. This is precisely why a 15-mm eye clearance has been selected for the design.

Although the general optical schematics appear to share similar structure to the work in [45], the fundamental difference lies in the fact that the virtual display optical system of our design, composed of elements E1 and E2, yields a desired spatially varying optical power as the function of the field angle, to achieve a statically foveated display scheme. Among the three elements in Fig. 5.1, the main freeform prism provides most of the optical magnification for the virtual display path, thus it is the core element to be optimized for achieving spatially varying of optical power in our foveated display scheme. Based on the same principles developed in Chapter 4, the design of the optical system for the statically foveated display path relies on a display panel with a uniform

pixel density and the precise control of the spatially varying optical power, depicted as Eq. (10).

The optimization process will be detailed in the next section.

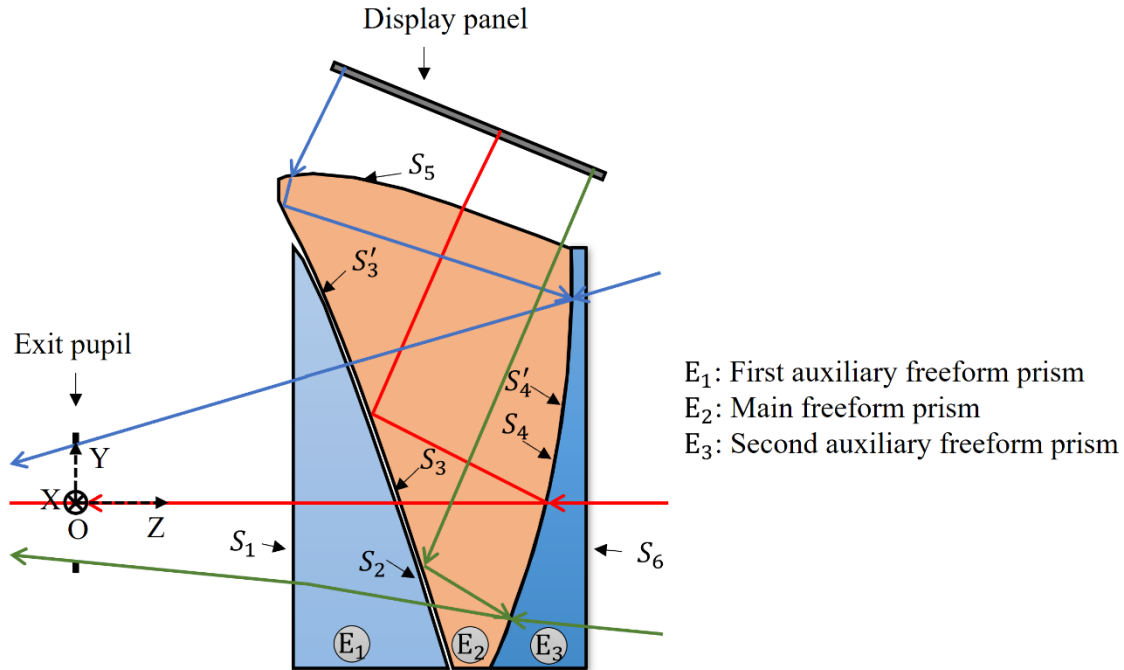


Fig. 5.1 The schematic diagram of foveated OST-HMD for the statically foveated. The first auxiliary freeform prism is composed of S1 and S2, the main freeform prism is composed of S3, S4, S3', and S5, and the second auxiliary freeform prism is composed of S4' and S6.

5.2 DESIGN AND OPTIMIZATION

Freeform surfaces typically provide superior optical performance compared to traditional spherical or aspherical surfaces, which are expressed with more variety of parameters and thus offer more degrees of freedom for compensating and balancing aberrations. However, practical designs must take into account design and manufacturing complexities and ultimately the overall cost. Therefore, the overall optical system in this study maintains symmetry about the YOZ plane instead of being entirely asymmetric, considering the inherent symmetry in the horizontal direction. As illustrated

in Fig. 5.1, the origin of the global coordinate system OXYZ is positioned at the center of the exit pupil, where the eye pupil of a viewer is placed. The Z axis aligns with the head pose direction, the OXY plane is perpendicular to the Z-axis, and the Y-axis is directing upward. It is assumed that the display panel is located above the eyebrow, thus the light ray path for the virtual display is folded within the main prism along the Y direction through two reflections by the surfaces S3' and S4, respectively. In the design configuration, all of the optical surfaces are decentered and tilted relative to this global reference.

The overall system consists of two independent light paths—the virtual display path through E1 and E2 and the see-through path via the E1, E2, and E3. However, optimizing the virtual display path is far more complex than the see-through path. Therefore, our design and optimization concentrate on the virtual display path, while the see-through path will be separately optimized to obtain the prescriptions of E3, following the completion of the display path design. In the case of no vision correction, the S6 of element E3 remains flat and its surface S4' is picked up from S4. For this reason, the rest of this section focuses on optimization strategies for the display path.

A critical aspect of optimizing a freeform system with complex waveguide-like lightpath folding is to define the proper structural and optical constraints. In case of optimizing the dual-element system for the virtual display path, the system design and optimization involve three key aspects: the structure constraints of the prisms, total internal reflection (TIR) conditions for surface S3', and optical performance control, particularly for spatially varying optical power as function of the field angle following the designed foveated scheme described in Eq. (9). The overall CODEV macro code for optimization of this foveated OST-HMD is provided in Appendix D.

5.2.1 Structure constraints

Since the surfaces of the two auxiliary freeform prisms are either flat or picked up from the surfaces of the main freeform prism, we only need to control the minimum thickness of these prisms. Considering the overall size of these elements, it is crucial to maintain a minimum thickness of at least 2 millimeters to ensure stability, ease of processing, and practical application.

The primary objective of the structure constraints is to ensure the proper propagation of rays within the main freeform prism, and the proper formation of a valid freeform prism through its three optical surfaces while maintaining manufacturable center and edge thickness. As shown in Fig. 5.2, the shape of the main prism is governed by the optical paths of the upper marginal ray (colored blue) at the maximum Y-direction field of 25° and the lower marginal ray (colored red) at the minimum Y-direction field of -15° . The intersection points P_{b1} , P_{c1} , and P_{c2} correspond to the intersections of the upper marginal ray with surfaces S4, S3', and S5, respectively. Similarly, the intersection points P_{a1-3} , and P_{b2} correspond to the intersections of the lower marginal ray with surfaces S3, S4, S3', and S5, respectively. By tracing the upper and lower marginal rays and locating these points in the global coordinate system, we can establish the following constraints to ensure the physical structure of the prism (Eq. 12), adequate eye clearance (Eq. 13), and maximum thickness (Eq. 14):

$$\left\{ \begin{array}{l} Y_{P_{a2}} - Y_{P_{a1}} < 0 \\ Y_{P_{a3}} - Y_{P_{a2}} > 0 \\ Z_{P_{a2}} - Z_{P_{a1}} > 2 \\ 0.2 < Y_{P_{c2}} - Y_{P_{c1}} < 5 \\ Y_{P_{b2}} - Y_{P_{b1}} > 1 \\ -5 < Z_{P_{b2}} - Z_{P_{b1}} < -0.5 \end{array} \right. , \quad (12)$$

$$\begin{cases} Z_{P_{a1}} > 15 \\ Z_{P_{c1}} > 15 \end{cases}, \quad (13)$$

$$Z_{P_{b1}} - Z_{P_{c1}} < 25, \quad (14)$$

where all the Y and Z coordinates in the equations are referenced to the global coordinate system with the origin located at the center of the exit pupil.

By applying constraints on the Y coordinates of point P_{a1-3} , the first two equations ensure the proper intersection of surfaces S3, and S4. This allows the lower marginal ray to be traced through the prism without any obstructions. Furthermore, by constraining the Z coordinates of points P_{a2} and P_{a1} , the upper and lower limits (e.g., 5 and 0.2mm, respectively) on the bottom thickness of the prism are established. By controlling the Y coordinates as the fourth equation in Eq. (12), involving points P_{c2} and P_{c1} , it ensures the proper intersection of surfaces S3', and S5, allowing the top marginal ray to pass through the prism without obstruction or escape. This control also aids in managing the prism's height. The remaining two constraints in Eq. (12), related to the Y and Z coordinates of points P_{b2} and P_{b1} prevent the top marginal ray from escaping after reflecting from surface S4' and assist in controlling the prism's thickness. The equations presented in Eq. (12) collectively guarantee the formation of a valid prism shape with the three optical surfaces. By restricting the Z coordinates of points P_{a1} and P_{c1} , Eq. (13) determines a minimum value for the eye clearance distance. Eq. (14) further controlled the total thickness of the main freeform prism by constraining the Z coordinates of the points of P_{b1} and P_{c1} .

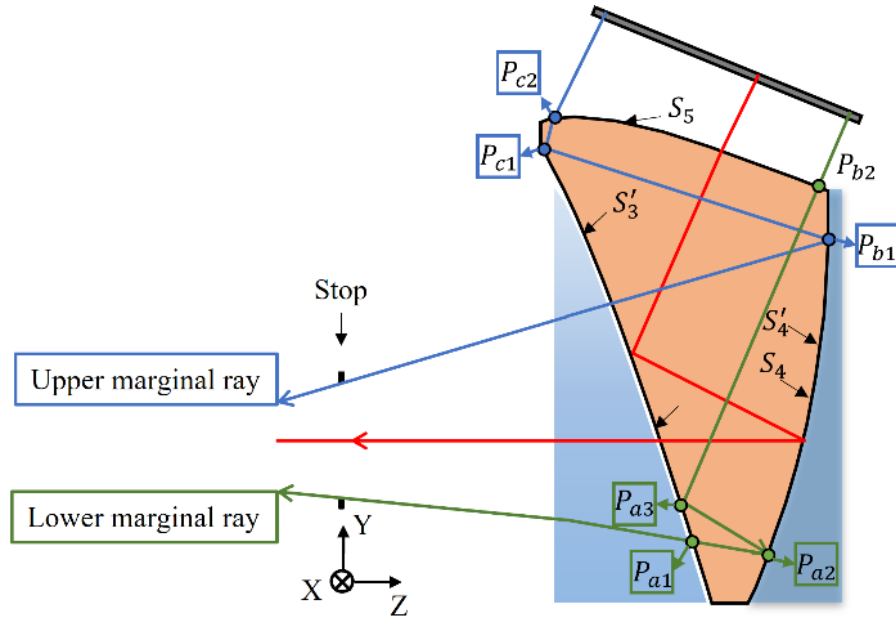


Fig. 5.2 Optical paths of upper and lower marginal rays of maximum and minimum Y-direction field.

5.2.2 TIR condition

As mentioned earlier, all rays from the entire display FOV are reflected off surface S_3' . Given the substantial overlap between the refractive and reflective optical paths for certain rays via surfaces S_3 and S_3' , it is not practical to apply a reflective film to S_3' . Consequently, it becomes necessary to ensure TIR conditions are satisfied at surface S_3' to maintain correct ray propagation within the prism. The critical angle θ_c is determined by the TIR condition, given by

$$\theta_c = \arcsin(1/n), \quad (15)$$

where n is the refractive index of the material of the main freeform prism. In this design, Cyclic Olefin Polymer (COP) is utilized instead of Acrylic (PMMA) because of its higher refractive index corresponding to larger critical angle potentially offering more space for optimization.

In the case of design structures starting with spherical or aspherical surfaces, it may be possible to identify a representative ray with the minimum incidence angle across the full field, such as the upper marginal ray for the maximum Y-direction field, to satisfy the TIR condition. However, for freeform surfaces, solely controlling the incident angle of the edge field is not sufficient for TIR to occur accurately for all fields. During the design process, the incident angles of the upper marginal ray, lower marginal ray, and the chief ray of the center field are controlled to be larger than the critical angle θ_c . This ensures that all rays across the field of view are reflected. On the other hand, for surfaces S3, S4 and S5, the TIR condition needs to be avoided. In CODEV, the MXA function is employed to ensure that the incident angles of all sampled fields are less than the critical angle θ_c .

5.2.3 Field sample

In contrast to traditional designs, the statically foveated virtual image in this study exhibits spatially varying magnification characteristics as function of field angle and is not rotational symmetry. To efficiently control the performance of the system and properly control optical magnification distribution through the FOV, fields distributed on concentric rings are sampled. Two zoom systems are utilized to sample fields on nine rings and several edge fields, as outlined in Table 5.2. The distribution of the sampled fields is illustrated in Fig. 5.3, where the red, green, and blue ‘*’ marks represent the sampled fields located within the fovea, parafovea, and peripheral regions, respectively. This approach ensures field sampling efficiency and provides enough samples for optimization.

Table. 5.2 The sampling field distribution.

		Zoom1		Zoom 2	
F1	4° field	0°, 4°	20° field	0°, 20°	
F2		0°, -4°		20°, 0°	
F3		4°, 0°		12°, 17,32°	
F4		2°, 3.464°		17.32°, -12°	
F5		3.464°, 2°		25° field	0°, 25°
F6		2°, -3.464°			25°, 0°
F7		3.464°, -2°			12°, 21.932°
F8	8° field	0°, 8°	30° field	21.932°, 12°	
F9		0°, -8°		16.583°, 25°	
F10		8°, 0°		30°, 0°	
F11		4°, 6.928°		22.361°, 20°	
F12		6.928°, 4°		25.377°, 16°	
F13		4°, -6.928°		35° field	24.495°, 25°
F14	6.928°, -4°	35°, 0°			
F15	12° field	0°, 12°	30°, 18.028°		
F16		0°, -12°	28.723°, 20°		
F17		12°, 0°	40° field	31.225°, 25°	
F18		6°, 10.392°		33.407°, 22°	
F19	10.392°, -6°	35°, 19.365°			
F20	15° field	0°, 15°	Edge field	34.641°, 20°	
F21		0°, -15°		35°, 25°	
F22		15°, 0°		35°, -15°	
F23		8°, 12.689°		-35°, 25°	
F24		12.689°, -8°		-35°, -15°	
F25		0, 0			

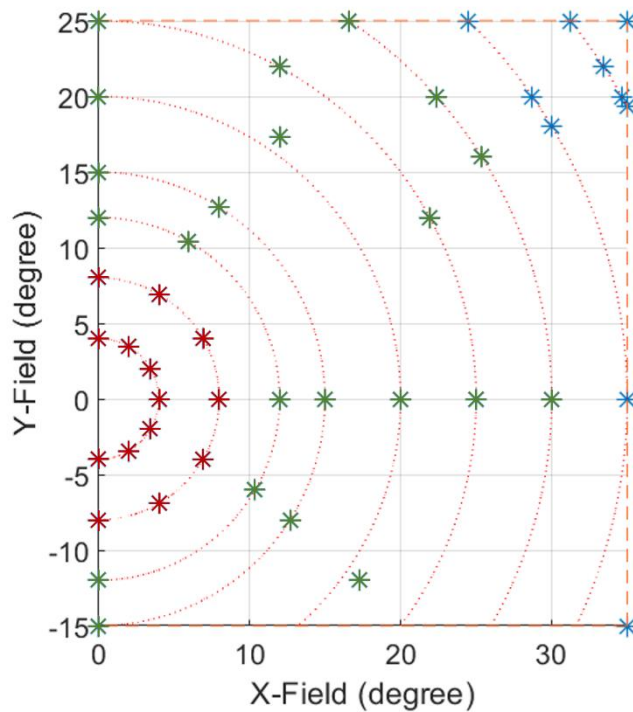


Fig. 5.3 The schematic diagram of field sampling distribution by circular grid.

5.2.4 Constraints for spatially varying optical power control

Based on the sandwich-structure of the eyepiece shown in Fig 5.1, we designed the virtual image optical path by combining the effects of the main wedge prism and the first auxiliary prism. The main freeform prism consists of three distinctive surfaces, while the first auxiliary prism has a flat surface S1 and surface S2 is picked up with surface S3 of the main prism. In the initial design phase, we began with a starting point composed of three conic surfaces or spherical surfaces, which may have a smaller FOV compared to our final target at first. The primary focus of the starting point design was to achieve the correct optical power for the center field while satisfying the structural and TIR condition requirements discussed in Section 5.2.1 and 5.2.2. After finding the starting point structure, we converted all the three surfaces into Zernike type surfaces.

Similar to the optimization method outlined in Section 4.2 for foveated displays in immersive HMDs, the resolution distribution of the foveated display can be determined by analyzing the chief ray heights at the display plane for the sampled fields, as described by Eq. (11). However, due to the freeform nature of the prism surfaces where local optical power can change rapidly, it is inadequate to strictly follow the constraints of the resolution distribution defined by Eq. (11) at critical balance field points, such as the θ_{c1} and θ_{c2} described in Section 3.1. Instead, a more robust method needs to be adapted from Eq. (11) to ensure gradual and smooth optical power variation without accidentally inducing steep change of optical power by local surface shapes. It is therefore preferable to control the average degradation rate in resolution or average optical power over a region based on the distance (D) at the display panel between the target field θ and

the center field. It ensures that the degradation rate changes smoothly and naturally for the three regions of display, avoiding sudden variations. The distance can be expressed as follows:

$$D(\theta) = \sqrt{(X(\theta) - X(0))^2 + (Y(\theta) - Y(0))^2}, \quad (16)$$

where the $X(\theta)$, $Y(\theta)$, $X(0)$, and, $Y(0)$ are the X and Y local coordinates at the display panel plane for θ -angle and center field, respectively. This distance can also be converted to represent the cumulative number of pixels utilized, based on the average value of the spatially varying resolution distribution function from the center field to the target field. As discussed in Section 5.3.2, the fields were sampled in a grid of nine concentric rings. Given the non-rotational symmetry of the freeform optics system, it is more efficient to control the average distance value for all fields with the same angular distance from center, which are located at the same ring of the sampled fields. By comparing it with the target resolution distribution value calculated using Eq. (9), we have effectively controlled the average degradation rate in resolution within the section across from the target field to the center field. The constraint for resolution distribution can be expressed as:

$$Metric_{resolution_distribution} = \left| \frac{\sum_i^n D_i(\theta)}{n} - D_{theoretical}(\theta) \right|, \quad (17)$$

where $D_i(\theta)$ is the distance at display panel from the center field to the field selected from one of the sampled fields with the angular distance θ as listed in Table 5.2, and the variable n denotes the total number of the fields with the angular distance θ located at the same field sampling ring. Another crucial aspect of optical performance is the control of rotational symmetry in the

resolution distribution. This is achieved by controlling the variance of the distances among all the sampled fields with the same angular distance., defined as,

$$Metric_{symmetry} = \sum_i^n [D_i(\theta) - \frac{\sum_i^n D_i(\theta)}{n}]^2 . \quad (18)$$

In addition to ensuring the compliance of the TIR and structure constraints defined by Eqs. (12) through (15), we incorporate the metrics defined by Eqs. (17) and (18) to control the resolution distribution, aiming to gradually align it with the theoretical function described in Eq. (9) at specific selected fields. We focus on controlling the spatial variation of optical power at angles such as 4°, 15°, and 30°. The selection of these angles is based on two key factors. Firstly, the degradation rate in resolution of the theoretical function around these fields shows relatively stability. Secondly, these fields closely represent the average resolution distribution within the fovea, parafovea, and peripheral regions, respectively. By choosing these angles, we ensure a smooth and coherent variation in the resolution distribution, gradually following the desired statically foveated resolution distribution function.

Beginning with the initial structure, we initially apply loose constraints on the resolution distribution and symmetry at the 4° field angle. Since the 4° field is within the fovea region and shares a similar resolution distribution with the center field, this step allows us to identify a structure that aligns more closely with our final target while preserving the first-order parameters. Subsequently, the high-order parameters of the three surfaces were incrementally introduced as variables for optimization. The constraints defined by Eqs. (17) and (18) were gradually incorporated during the optimization process, applied at the field angles of 15° and 30°. Initially,

these constraints were implemented with loose controls and were subsequently tightened as the optimization progressed. Additionally, the FOV is gradually increased towards the design target.

It is important to note two factors in the optimization. Firstly, we minimize the usage of surface S_5 parameters in the preliminary stage due to its significant impact on aberration control and its role in achieving the desired optical power spatial variation. For example, we optimized the system using 6th order parameters of the surface S_3 and S_4 , while only employing a conic type for surface S_5 . This step helps us find a result with good optical performance under relatively loose constraints for resolution distribution and symmetry. Subsequently, we maintain the optics with equivalent performance and gradually introduce the parameters of surface S_5 as variables, up to 6th order. This strategy proves to be more time-efficient and facilitates the identification of the appropriate structure compared to direct optimization with 6th order parameters for all surfaces. Secondly, if the pixel count of the display is sufficient to provide higher perceived performance, we can relax the control requirements for the resolution distribution in each region. Thus, the active size of the display panel serves as an important reference for optimization. Initially unconstrained, it is gradually limited to the actual size listed in Table 5.1. Ultimately, a total of 60 variables are activated to optimize the system. The constraints for resolution distribution, defined by Eq. (17), are controlled within one pixel, eight pixels, and fifty pixels error for 4°, 15°, and 30° angle field, respectively.

5.3 Performance evaluation

The 2D layout of the virtual optical path for the statically foveated freeform OST-HMD is depicted in Fig. 5.4. The figure provides a cross-sectional view of both the YOZ plane and XOZ plane,

showcasing the elements that are relevant to the virtual optical path, namely the first auxiliary freeform prism and the main freeform prism.

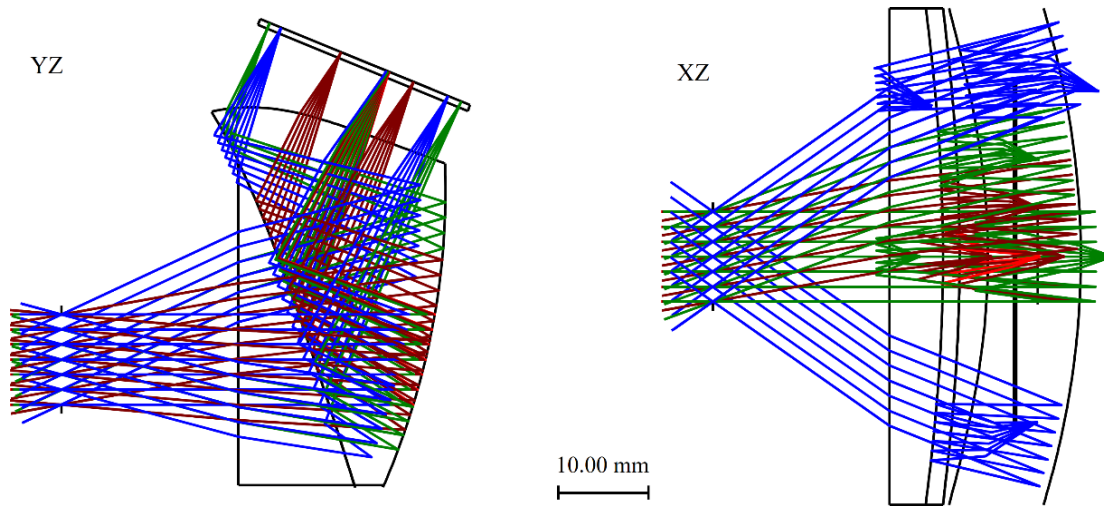


Fig. 5.4 The YOZ plane and XOZ plane layout of virtual image optical path of statically foveated freeform OST-HMD.

The specific surface parameters and the global coordinates of each surface of three freeform prisms are listed in Appendix E.

5.3.1 MTF analysis

The polychromatic MTF plots of the virtual image optical path for the statically foveated freeform OST-HMD with 10-mm exit pupil are presented in Fig. 5.5 (a)-(c). The plots are categorized into three distinct regions based on their functional characteristics: fovea, parafovea, and peripheral region. The MTF values exceed 10% at the Nyquist frequency for the majority of fields, indicating satisfactory optical performance. Notably, the fields within the foveated region demonstrate exceptional optical performance for MTF.

To visually depict the MTF performance across different regions, Fig. 5.6 presents a box plot of MTF values. The plot employs the colors red, green, and blue to represent the MTF plots for

the fovea, parafovea, and peripheral regions, respectively. The solid line in each plot represents the average MTF value for all sampled fields within the corresponding region. For each region, six fields were sampled to calculate the average MTF and generate the box plots. The box in the plot represents the interquartile range (IQR), which spans from the first quartile (25th percentile) to the third quartile (75th percentile). Inside the box, a line indicates the median value. Additionally, small horizontal lines extending beyond the box's upper and lower ends represent the maximum and minimum MTF values in the region.

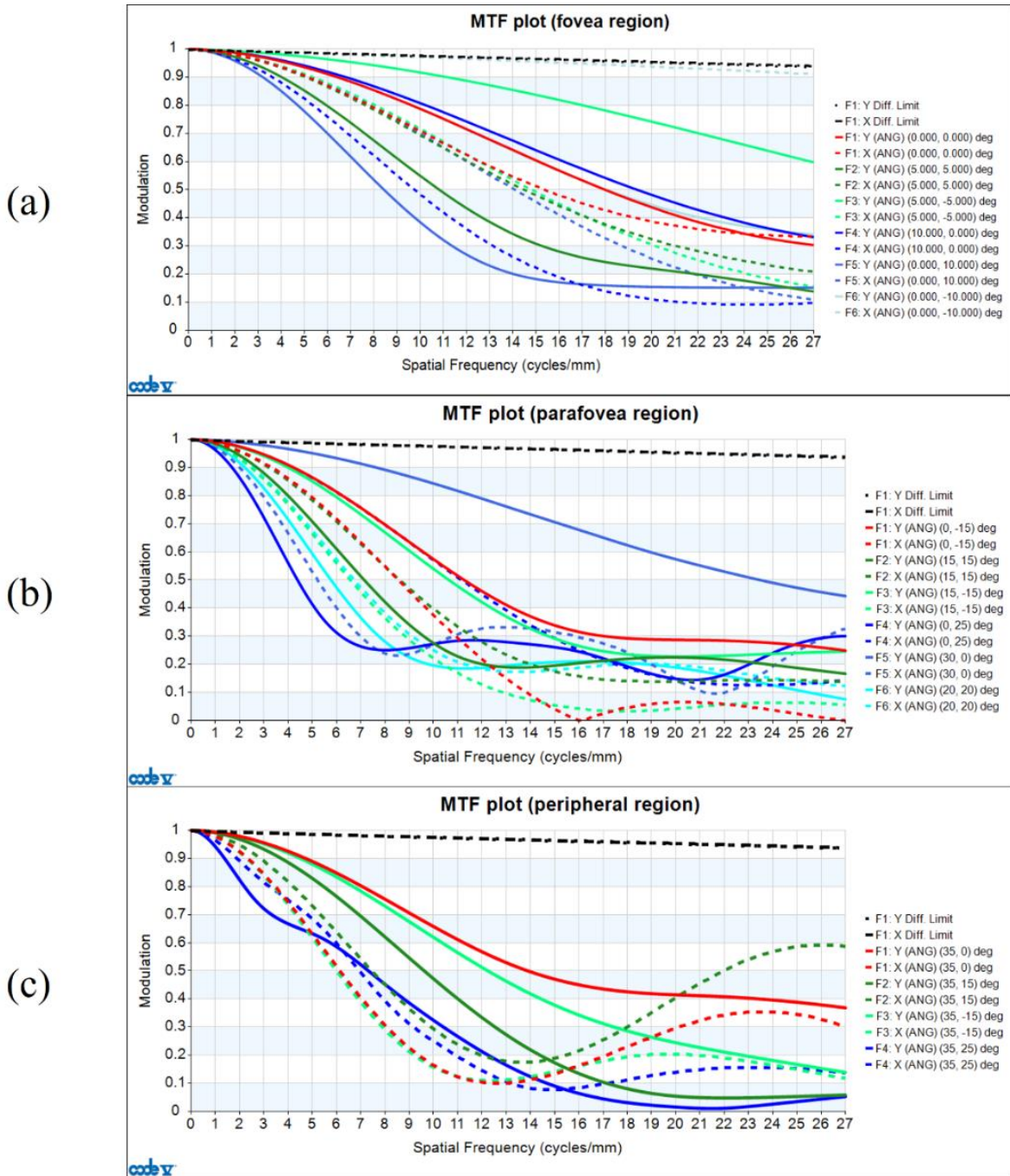


Fig. 5.5 The MTF plots of virtual image optical path of statically foveated freeform OST-HMD for (a) fovea region, (b) parafovea region, and (c) peripheral region, respectively.

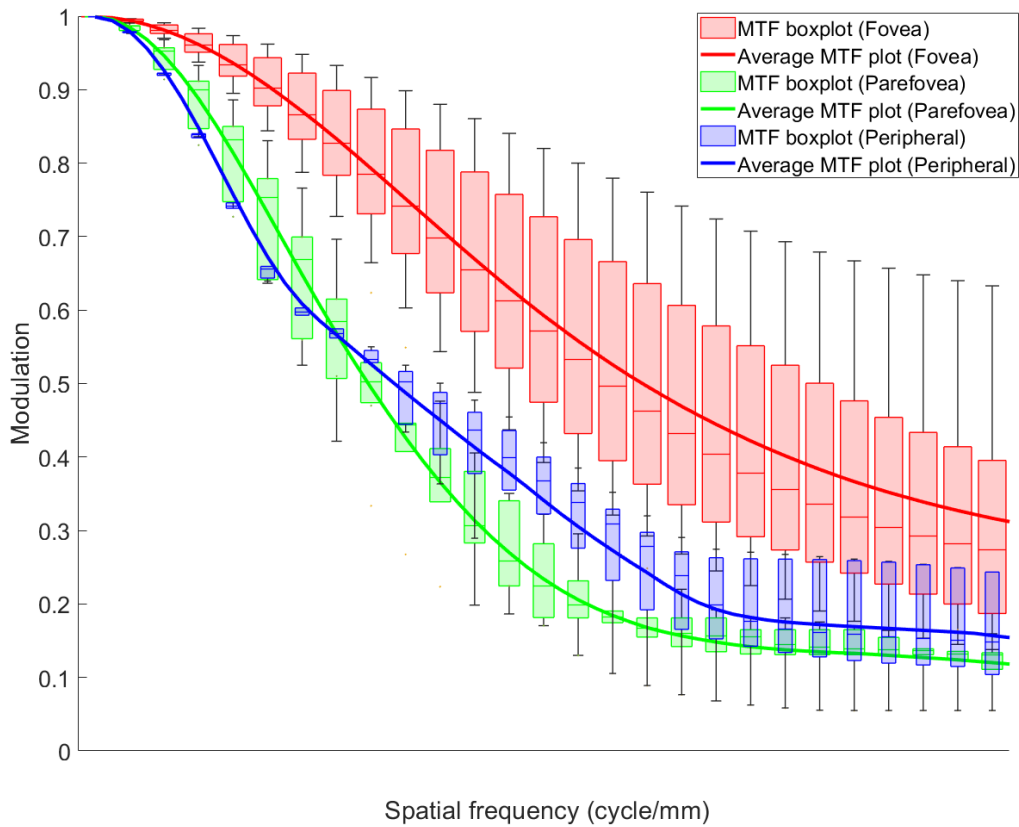


Fig. 5.6 The MTF box plots of virtual image optical path of statically foveated freeform OST-HMD.

Additionally, we simulated MTF plots for different eye pupil positions with a 4-mm diameter size. Specifically, we examined the scenario where the human eye moves 2 mm along the +y direction, -y direction, and +x direction, respectively. These simulations are presented in Fig. 5.7. The results demonstrate that the MTF values for all fields exceed 0.1 at the cut-off frequency of 27 lps/mm, indicating that the MTF performance at various eye pupil positions meets the design requirements.

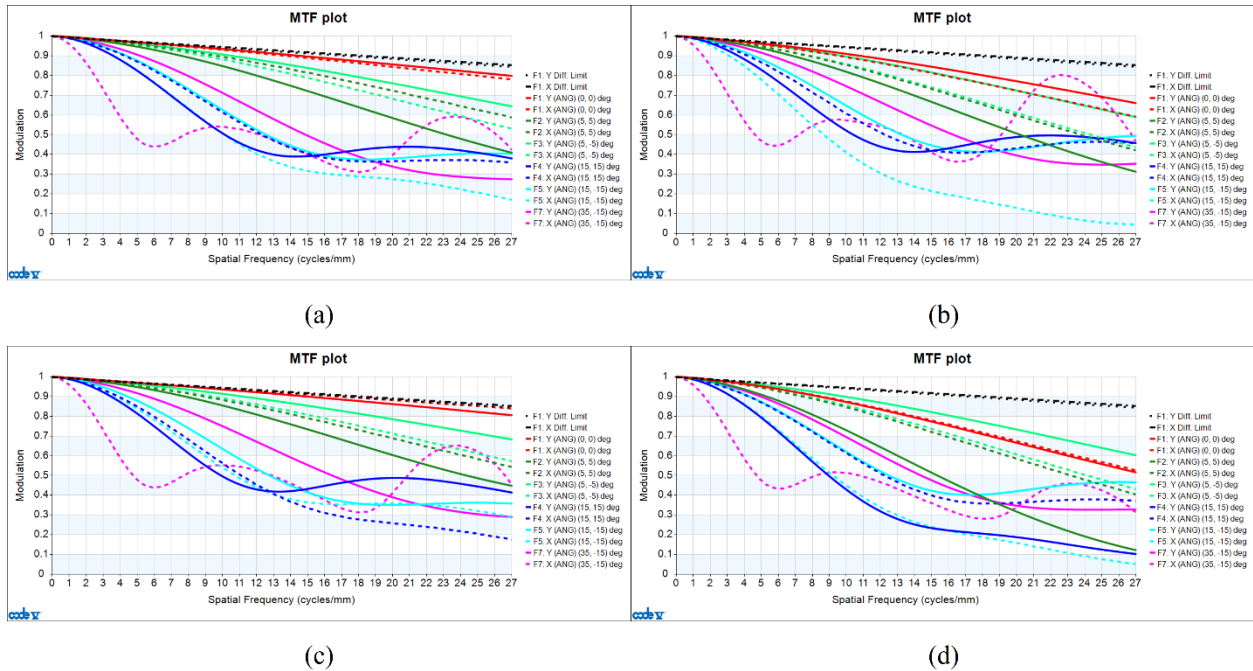


Fig. 5.7 The MTF plots of virtual image optical path of statically foveated freeform OST-HMD with 4-mm exit pupil mimic as human eye when the pupil is (a) at center, (b) moved 2 mm along +y direction, (c) -y direction and (d) +x direction, respectively.

5.3.2 Perceived performance with Arizona eye model

Similar to the approach described in Section 4.3.2 for perceived performance analysis, we employ the Arizona eye model to receive the light emitted from the display panel. In Fig. 5.8 (a) and (b), we present two examples of the reversed layouts obtained by rotating the eye model by 0° and 30° in the YOZ plane, respectively.

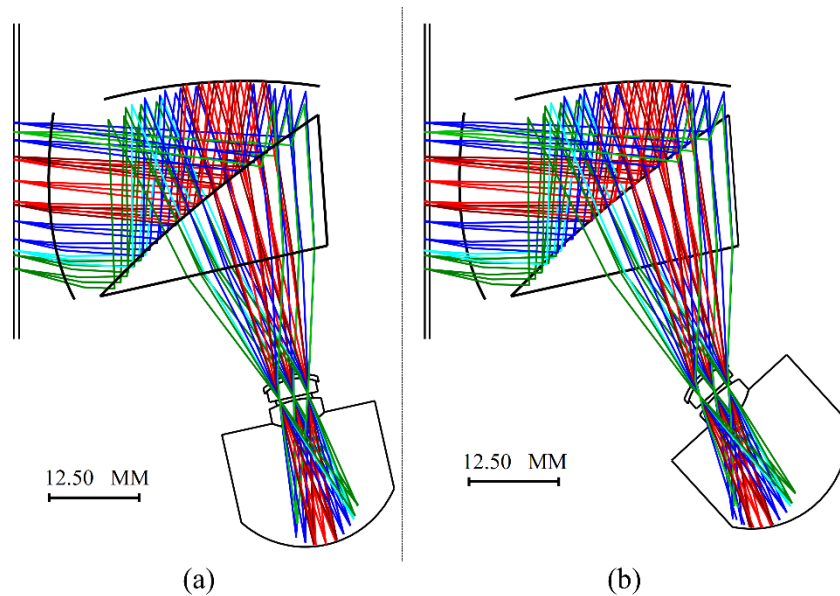


Fig. 5.8 The layout of the reserved system with Arizona eye model: (a) eye gaze at 0°; and (b) eye gaze at 30°.

The perceived performance of the statically foveated display was assessed by rotating the Arizona eye model along the diagonal direction across the full FOV. The Arizona eye model was rotated from 0° to 30° with a 10° interval along the diagonal direction for full FOV, corresponding to the positions (0°, 0°), (8.14°, 5.81°), (16.28°, 11.62°), and (24.42°, 17.43°) on the diagonal. To facilitate comparison, the spatial frequency unit was converted to cycles per degree in visual space. The designed peak angular resolution was set to 2 arcminutes per pixel, equivalent to the Nyquist frequency of 15 cycles per degree or 52.1 cycles per millimeter on the retina. Fig. 5.9 (a)-(d) present the MTF plots for the Arizona eye model at the aforementioned four angles, where we calculated the average MTF values in the tangential and radial directions for each sampled field angle across the display.

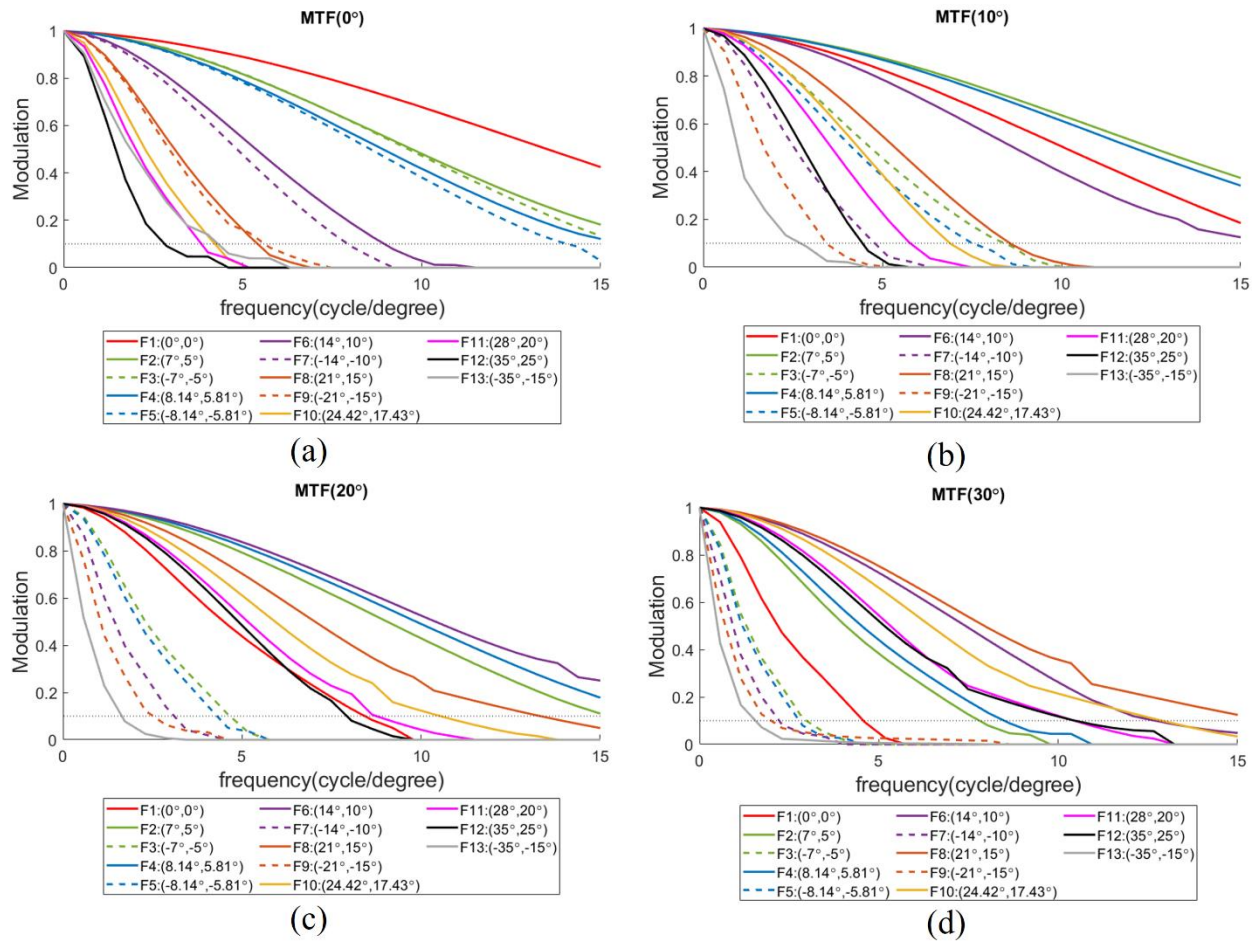


Fig. 5.9 MTF plots for various fields with the rotation angle of Arizona eye model part: (a) 0°; (b) 10°; (c) 20°; (d) 30°.

The contrast modulation threshold of 10% was used at the maximum angular frequency to determine the perceived limiting resolution. Figures 5.10(a) to 5.10(d) depict the perceived limiting resolution distributions of the foveated display as a function of the display field angle, considering eye rotation angles of 0°, 10°, 20°, and 30° along the diagonal direction, respectively.

Based on analysis presented in Figs. 5.10(a) to 5.10(d), within the eye movement region of up to 30°, the display achieves a peak resolution of approximately 50% of a standard observer, corresponding to an angular resolution of around 2 arcminutes per pixel. The perceived limiting

resolution of the foveated display exceeds the visual acuity of a standard observer throughout the entire field of view, with the exception of a small region near the gaze direction. In summary, the static foveated display demonstrates satisfactory perceived performance without the need for dynamic tracking and scanning devices, particularly in areas that undergo frequent eye movements.

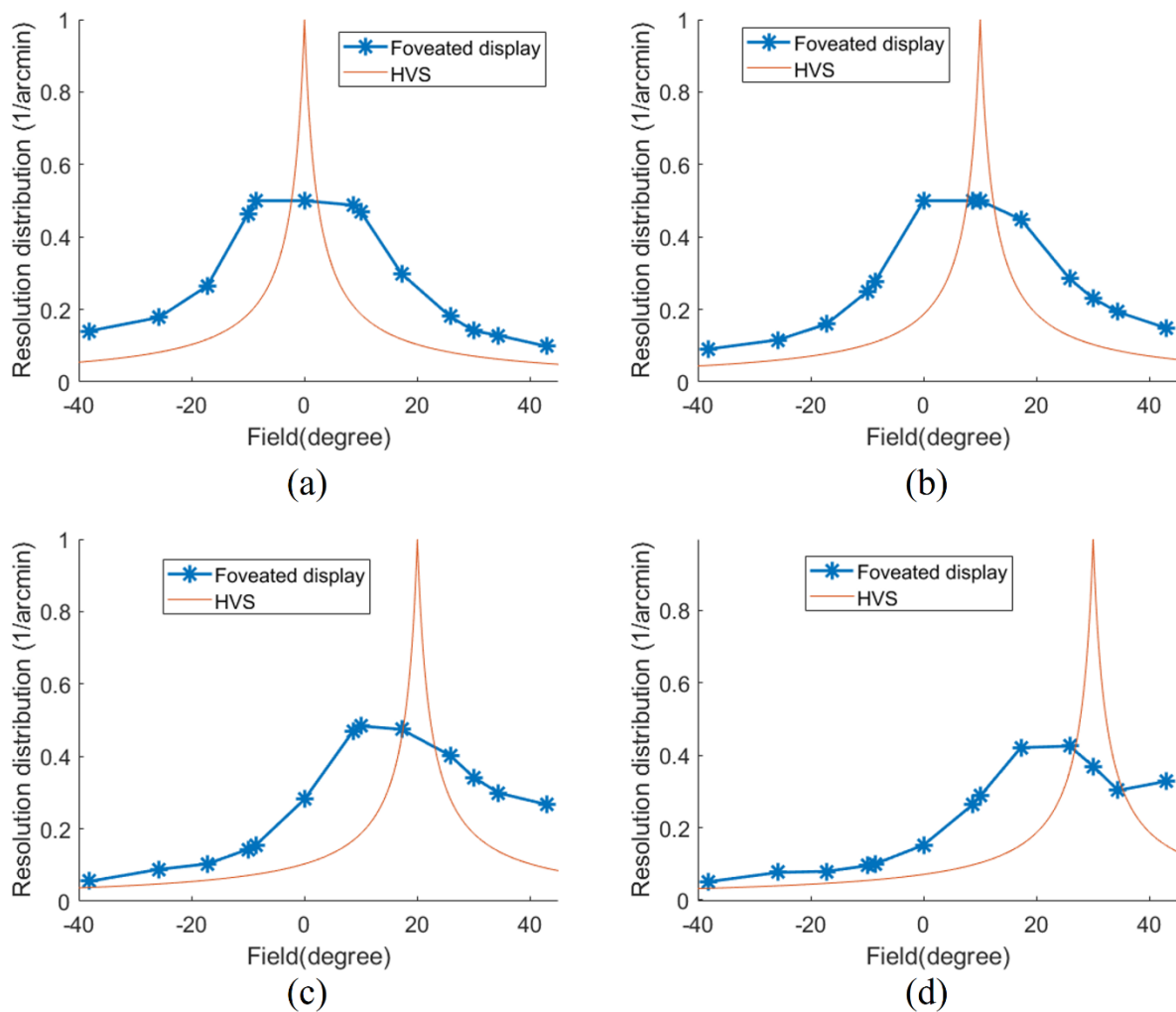


Fig. 5.10 The resolution distributions of the foveated display as the function of the field angle with the eye rotation angle of (a) 0°; (b) 10°; (c) 20°; (d) 30° along diagonal direction, respectively.

5.3.3 Distortion grid and resolution distribution map

Figure 5.11(a) illustrates the distortion grid of the foveated display at display plane. Fig 5.11(b) shows the resolution distribution map across the virtual display plane. To generate the resolution distribution map, we traced 800,000 chief rays with a field sampling angle interval set to 0.1% of the full FOV, resulting in a horizontal interval of 0.07 degrees and a vertical interval of 0.05 degrees. To facilitate the ray tracing process in the CODEV software, for each certain horizontal sample, we traced the 1000 field region vertically from -25° to 25° with a 0.05-degree interval. From this dataset, we selected the data within our designed FOV ranging from -15° to 25° , yielding 800 chief ray heights at the display plane. Based on the findings shown in Fig 5.11(b), it is evident that there is a noticeable variation in resolution distribution as the function of field angle, and the overall view exhibits a high level of rotational symmetry. Figure 5.11(c) presents a detailed representation of the resolution distribution across the field angle along the diagonal direction. The simulated degradation rate of resolution is highly consistent with our intended design objective, exhibiting a relatively stable rate within the foveated region and progressively declining at an accelerated pace with increasing field angles.

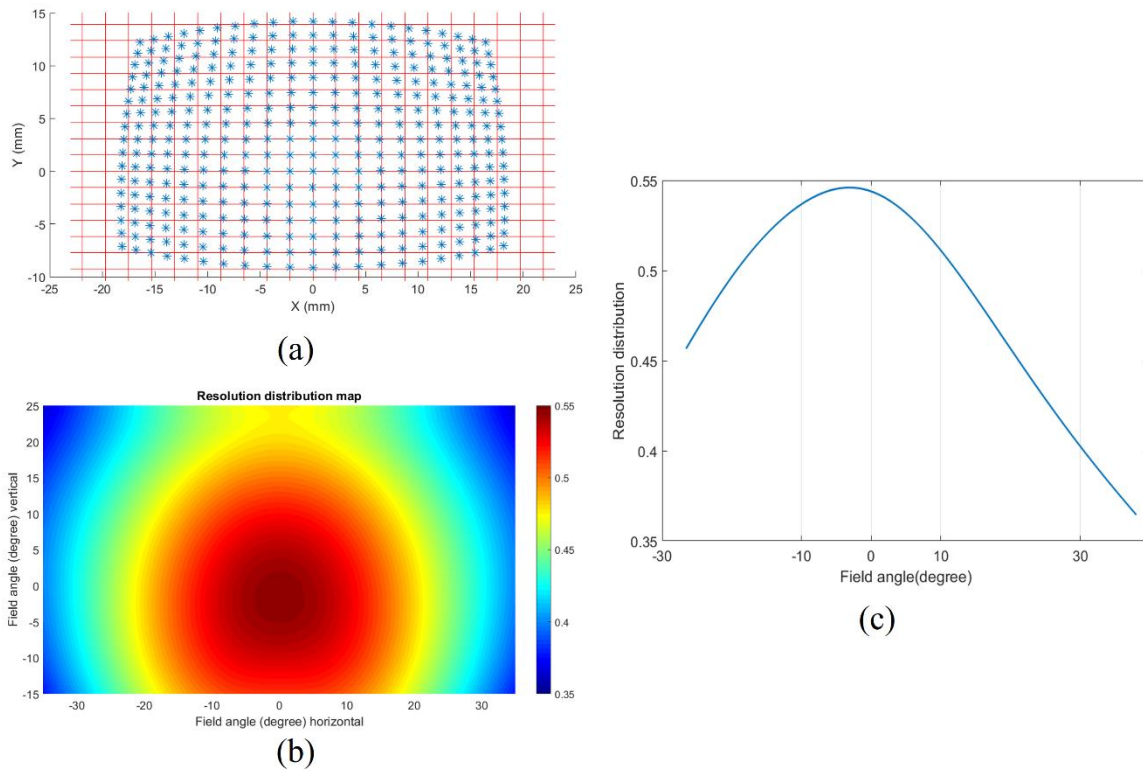


Fig. 5.11 (a) The distortion grid of designed foveated display; (b) The resolution distribution in field map; (c) the resolution distribution of designed foveated display as the function of the field along the diagonal direction.

5.3.4 Optical see-through path performance

By incorporating the first auxiliary lens, the optical see-through path can easily achieve exceptional performance with a flat surface S6 of the second auxiliary freeform. The other surface S4' of it is picked up the surface S4, ensuring precise cementing of the lens and prism and simplifying the design of the freeform lens. The second auxiliary prism exhibits a minimum thickness of approximately 1.5 millimeter. The layout of the optical see-through path for the static foveated display is depicted in Fig. 5.12.

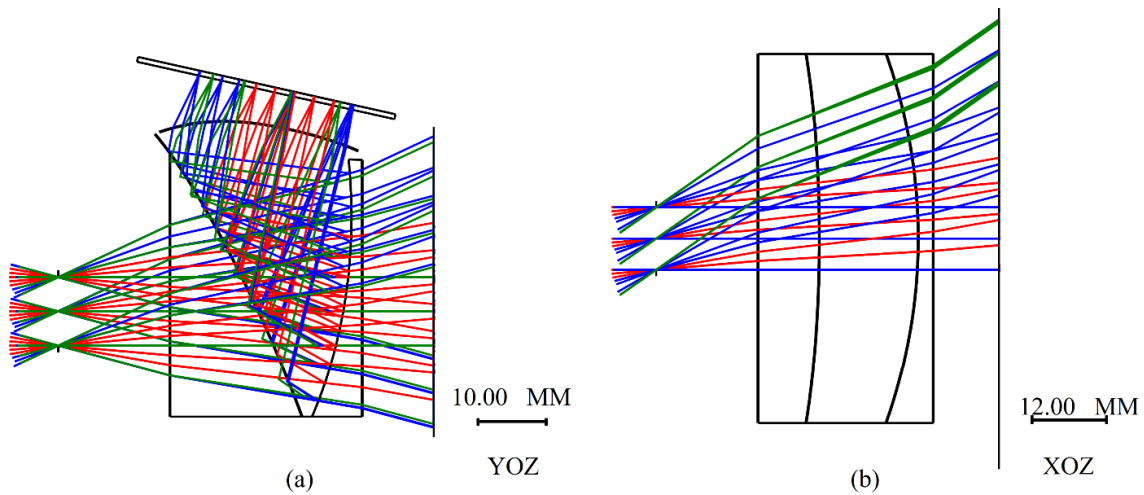


Fig 5.12 The YOZ plane and XOZ plane layout of optical see-through path of statically foveated freeform OST-HMD.

In order to assess the optical performance of the optical see-through path, an ideal lens was introduced 10 mm after the entire system and perpendicular to the optical axis. Fig. 5.13 presents the MTF plot and distortion grid of the optical see-through path for the statically foveated freeform OST-HMD. The MTF exceeds 40% for all fields at the Nyquist frequency, which corresponds to a resolution of 1 arcminute per pixel for the human eye. Furthermore, the maximum distortion value for the entire see-through view is below 0.1%.

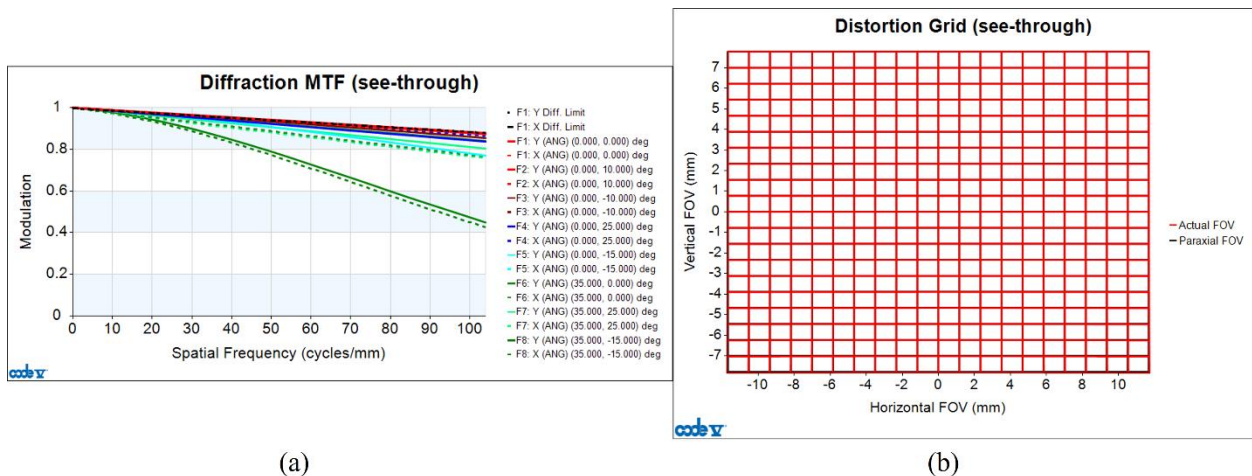


Fig. 5.13 (a) The MTF plot and (b) the distortion grid of optical see-through path of statically foveated freeform OST-HMD.

5.4 TOLERANCE ANALYSIS

Following the evaluation and analysis of the excellent optical performance achieved by the statically foveated freeform OST-HMD, we conducted a tolerance analysis to assess the effects of fabrication and alignment imperfections. It is well recognized that direct tolerance allocation to the coefficients of free-form surfaces is not practical, as perturbations on individual coefficients do not accurately represent realistic manufacturing figure errors. To address this, we adopted an approach to generate random surface figure errors inspired by the work of Hu and Hua [46], which effectively accounts for manufacturing tolerances and their impact on the overall system performance. This method was developed to simulate random surface deformations using CODEV's interferogram (INT) file. A random surface can be created by combining all Zernike terms up to a given radial order using a MATLAB program, excluding piston and tilt. The coefficients of the Zernike terms were randomly generated with a uniform distribution from -1 to 1 μm . Variable weightings were assigned to the Zernike terms of different orders to generate deformations that approximate realistic manufacturing errors, with an emphasis on lower-order terms dominating the RMS deformation. The total deformation was scaled to a maximum absolute value of 1 μm , and only the scaled coefficients were written into a ZRN INT file. An example of the resulting random deformation is shown in Fig. 5.14, generated by Zernike terms up to the sixth order. A collection of 100 INT files of random surface deformations was created to facilitate tolerance analysis for the freeform surfaces. In each Monte Carlo tolerancing cycle, a single INT file was chosen randomly and scaled randomly according to the deformation tolerance values required considering the clear aperture size and manufacture method. The orientation of the

interferogram was also randomized to augment the variety of deformations. The selected deformation was then applied to the surface, covering the entire clear aperture.

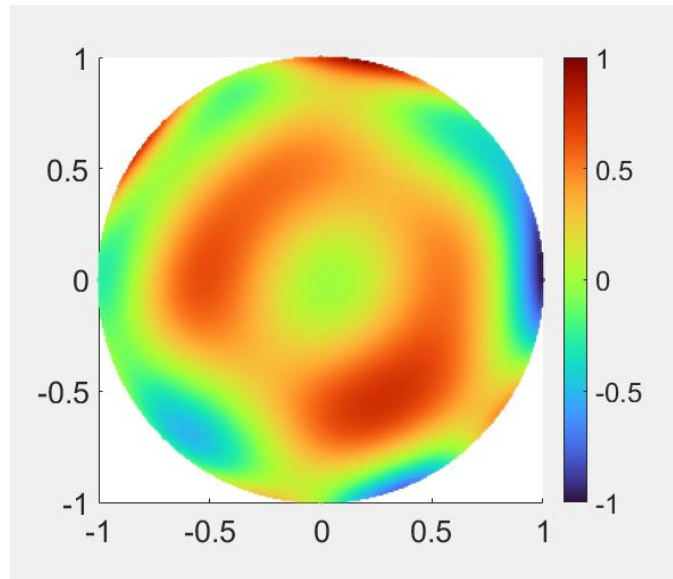


Fig. 5.14 The schematic diagram random surface deformations generated with MATLAB.

Table 5.3 presents the overall tolerance values for the virtual optical path of the system, encompassing the first auxiliary freeform prism and the main freeform prism. The surface roughness error was set at 5 μm peak-to-valley (PV), and the surface sag error at 20 μm PV level, taking into account the quality achievable with the current diamond turning process. It is worth mentioning that these tolerance values are far more conservative than what are practical in most diamond turning shops. During each tolerancing cycle, these surface deformations are randomly assigned to all freeform surfaces.

Table 5.3 Tolerance items.

Tolerance Type	Location	Value	Unit
DLT—thickness delta	S1	500	μm
DLT—thickness delta	S2, S3, S3', and S4'	40	μm
DLT—thickness delta	S5	20	μm
DLN—refractive index delta	E1 and E2	0.001	--
DLV—V-number delta	E1 and E2	0.008	--
DLX—surface X -displacement	S2, S3, S3', S4' and S5	25	μm

DLY–surface Y -displacement	S2, S3, S3', S4' and S5	25	μm
DLZ–surface Z-displacement	S2, S3, S3', S4' and S5	25	μm
DLA–surface alpha tilt	S2, S3, S3', S4' and S5	10	mrad
DLB–surface beta tilt	S2, S3, S3', S4' and S5	10	mrad
DLG–surface gamma tilt	S2, S3, S3', S4' and S5	10	mrad
DLS–delta sag at clear aperture	S2, S3, S3', S4' and S5	20	μm
DSR–surface roughness error	S3, S3', S4' and S5	5	μm

A total of five thousand Monte Carlo tolerance simulations were performed to analyze the probable changes in polychromatic MTF at the 80% of Nyquist frequency of 21.6 cycles/mm, considering a 4 mm exit pupil. The results are presented in Figure 5.15 and summarized in Table 5.4. Although the largest probable decrease in MTF, with a 97.7% confidence level, amounts to -0.24553, the MTF values at the 80% of Nyquist frequency for all sampled fields remain above 0.1. It is worth noting that the significant decrease in MTF is primarily attributed to lateral chromatic aberration due to the fact that a monolithic material type was used in the design. To provide further evidence, the probable changes in monochromatic MTF at the Nyquist frequency of 27 cycles/mm are illustrated in Figure 5.16 and detailed in Table 5.5. Lateral chromatic aberrations may be corrected by digital processing in a similar fashion to digital correction of distortion. In summary, the tolerance analysis demonstrates the stability of the virtual image path in the statically foveated freeform OST-HMD. Overall, the system can maintain an MTF value above 0.1 at the 80% of Nyquist frequency for all sampled fields with a high confidence level of 97.7%.

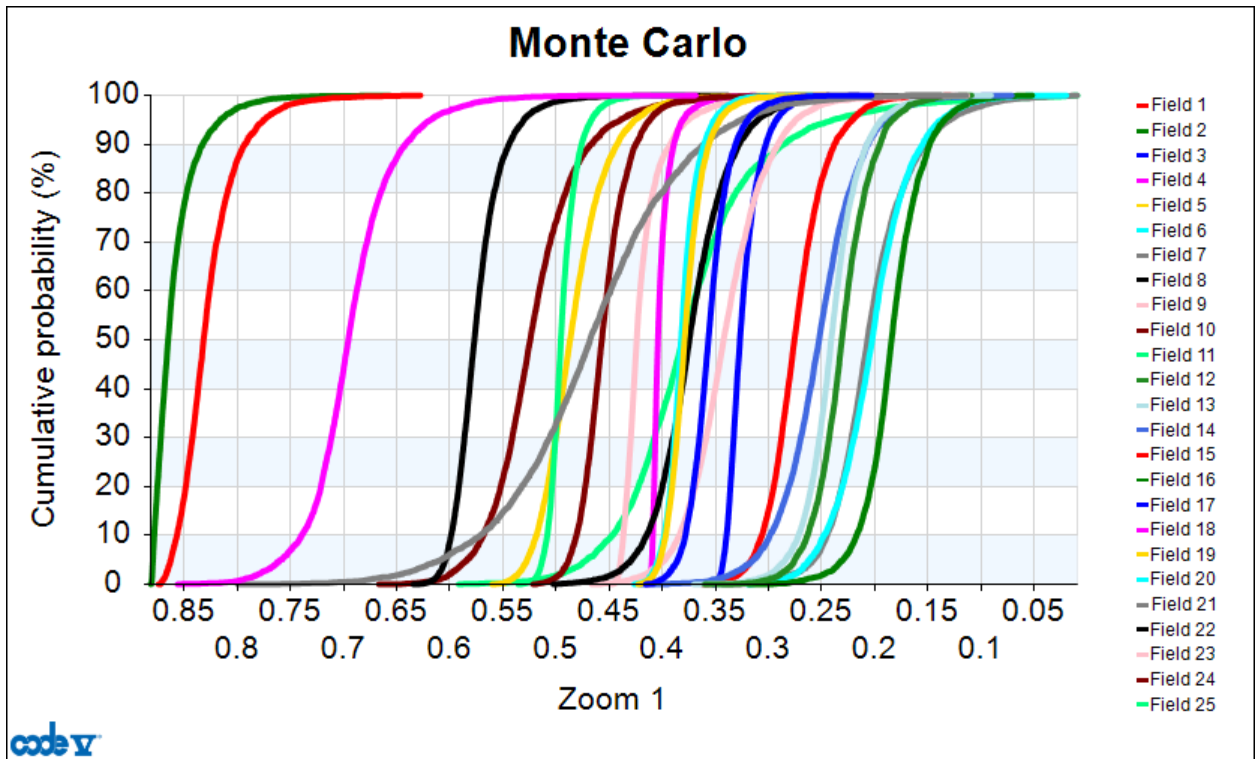


Fig. 5.15 Cumulative probability change of polychromatic MTF at 80% of Nyquist frequency of 21.6cycles/mm with 4-mm exit pupil.

Table 5.4 Monte Carlo tolerance analysis results I.

Monte Carlo Analysis –5000 Trials Cumulative Probability Change of MTF at 27 Cycles/mm				
Field	50%	84.1%	97.7%	99.9%
F1 (0°, 0°)	0.000272	-0.02754	-0.07577	-0.17624
F2 (0°, -7°)	-0.00104	-0.02302	-0.06926	-0.15434
F3 (10°, 0°)	-0.0018	-0.02019	-0.05322	-0.10532
F4 (0°, 13°)	0.011372	-0.02617	-0.09477	-0.19551
F5 (10°, -7°)	-0.00187	-0.01828	-0.04755	-0.10133
F6 (10°, 13°)	-0.003	-0.0178	-0.04552	-0.09742
F7 (0°, -15°)	0.007763	-0.07365	-0.17201	-0.28961
F8 (20°, 0°)	0.00466	-0.02952	-0.08185	-0.18815
F9 (25°, 0°)	0.010571	-0.02737	-0.07719	-0.18325
F10 (20°, -7°)	-0.00074	-0.02437	-0.05956	-0.15342
F11 (20°, 13°)	-0.0059	-0.02005	-0.04445	-0.08402
F12 (10°, -15°)	-0.00532	-0.03164	-0.06746	-0.1134
F13 (10°, 25°)	-0.0095	-0.03403	-0.07444	-0.12584
F14 (20°, -15°)	-0.00797	-0.04249	-0.09029	-0.15385
F15 (30°, 0°)	0.01277	-0.01506	-0.05543	-0.11993
F16 (20°, 25°)	-0.05241	-0.07933	-0.11813	-0.16387
F17 (30°, -5°)	0.000176	-0.0175	-0.04633	-0.09822
F18 (30°, 13°)	0.025939	0.015682	-0.01016	-0.05731

F19 (35°, 0°)	0.017427	-0.01475	-0.06266	-0.14621
F20 (30°, -15°)	-0.01163	-0.04591	-0.09693	-0.15196
F21 (30°, 25°)	-0.07282	-0.11206	-0.17841	-0.25144
F22 (35°, -7°)	-0.00419	-0.02724	-0.06804	-0.13992
F23 (35°, 13°)	0.037073	0.017664	-0.03505	-0.14936
F24 (35°, -15°)	-0.03252	-0.07267	-0.14845	-0.26659
F25 (35°, 25°)	-0.04077	-0.10335	-0.24553	-0.40604

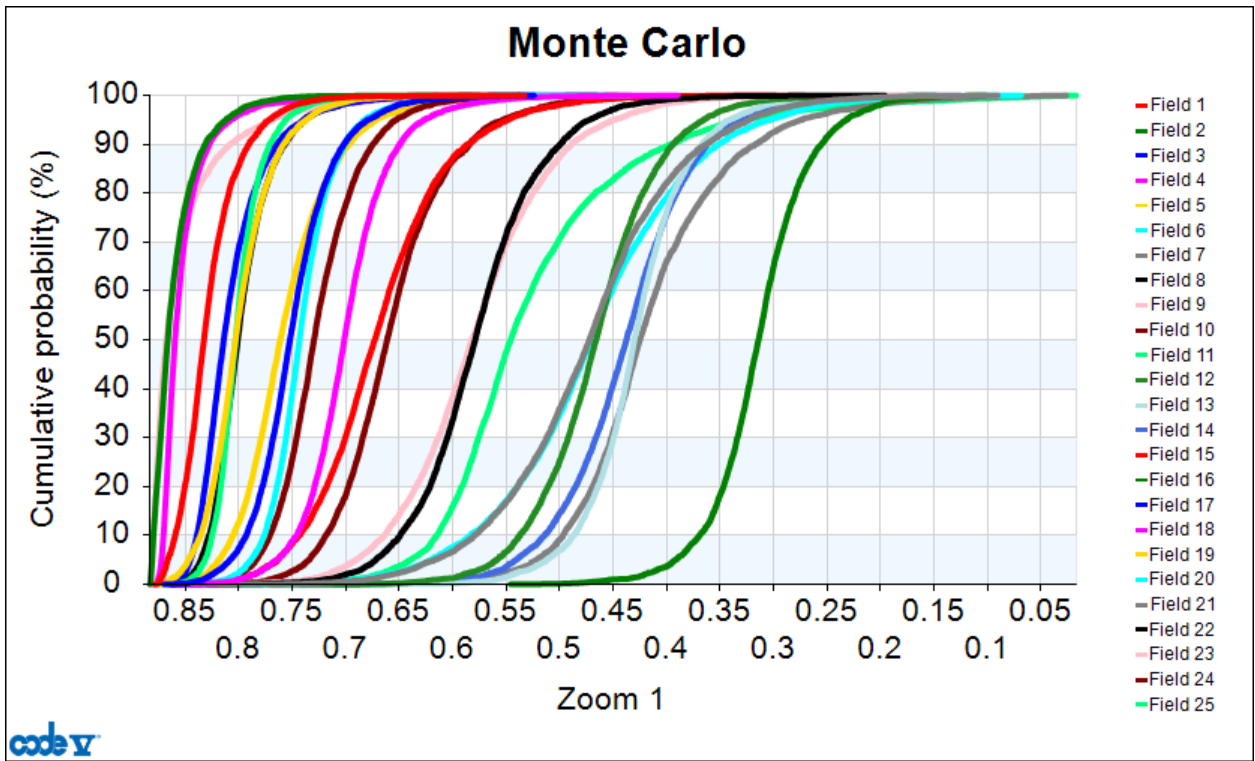


Fig. 5.16 Cumulative probability change of monochromatic MTF at 80% of Nyquist frequency of 21.6cycles/mm with 4-mm exit pupil.

Table 5.5 Monte Carlo tolerance analysis results II.

Monte Carlo Analysis –5000 Trials Cumulative Probability Change of MTF at 27 Cycles/mm				
Field	50%	84.1%	97.7%	99.9%
F1 (0°, 0°)	0.000161	-0.02953	-0.08114	-0.16578
F2 (0°, -7°)	-0.00081	-0.02522	-0.07335	-0.1512
F3 (10°, 0°)	-0.00382	-0.04088	-0.10091	-0.21108
F4 (0°, 13°)	0.012246	-0.02542	-0.0942	-0.21853
F5 (10°, -7°)	-0.00473	-0.03787	-0.09223	-0.19034
F6 (10°, 13°)	-0.00412	-0.03453	-0.09072	-0.17854
F7 (0°, -15°)	0.00715	-0.07286	-0.17984	-0.31259

F8 (20°, 0°)	0.005668	-0.0513	-0.12996	-0.27329
F9 (25°, 0°)	0.018929	-0.05078	-0.15194	-0.27366
F10 (20°, -7°)	-0.00089	-0.04075	-0.10294	-0.22633
F11 (20°, 13°)	-0.00776	-0.03007	-0.07371	-0.16158
F12 (10°, -15°)	-0.01272	-0.06672	-0.14136	-0.26638
F13 (10°, 25°)	-0.01498	-0.06088	-0.13401	-0.24364
F14 (20°, -15°)	-0.01298	-0.07018	-0.1479	-0.2584
F15 (30°, 0°)	0.02878	-0.03319	-0.13703	-0.27038
F16 (20°, 25°)	-0.08525	-0.12742	-0.19353	-0.27027
F17 (30°, -5°)	-0.00222	-0.03739	-0.107	-0.20591
F18 (30°, 13°)	0.058449	0.036848	-0.01853	-0.14958
F19 (35°, 0°)	0.025866	-0.02068	-0.09801	-0.25052
F20 (30°, -15°)	-0.02582	-0.11376	-0.23487	-0.35997
F21 (30°, 25°)	-0.12985	-0.20728	-0.33908	-0.49813
F22 (35°, -7°)	-0.00557	-0.03624	-0.09478	-0.20245
F23 (35°, 13°)	0.054444	0.016316	-0.09266	-0.33013
F24 (35°, -15°)	-0.04095	-0.09525	-0.18746	-0.323
F25 (35°, 25°)	-0.04486	-0.14772	-0.34665	-0.5534

5.5 OPTO-MECHANICAL DESIGN

The freeform elements were precisely modeled using SOLIDWORKS, and a carefully designed mounting structure was implemented with a retainer to securely hold the three elements together without the requirement for cementing. The retainer effectively maintains an air gap between the elements E1 and E2 while ensuring that the gap remains sufficiently small to preserve the desired optical performance. Additionally, the mounting structure ensured proper placement of the display panel at the designated location, as depicted in Fig. 5.17(a). Furthermore, an exploded view of the entire system is presented as Fig. 5.17(b) to provide a comprehensive understanding of its assembly and components.

The fabrication of the optical system is under way. Unfortunately, the process is longer than expected, thus the testing data will not be included in this dissertation.

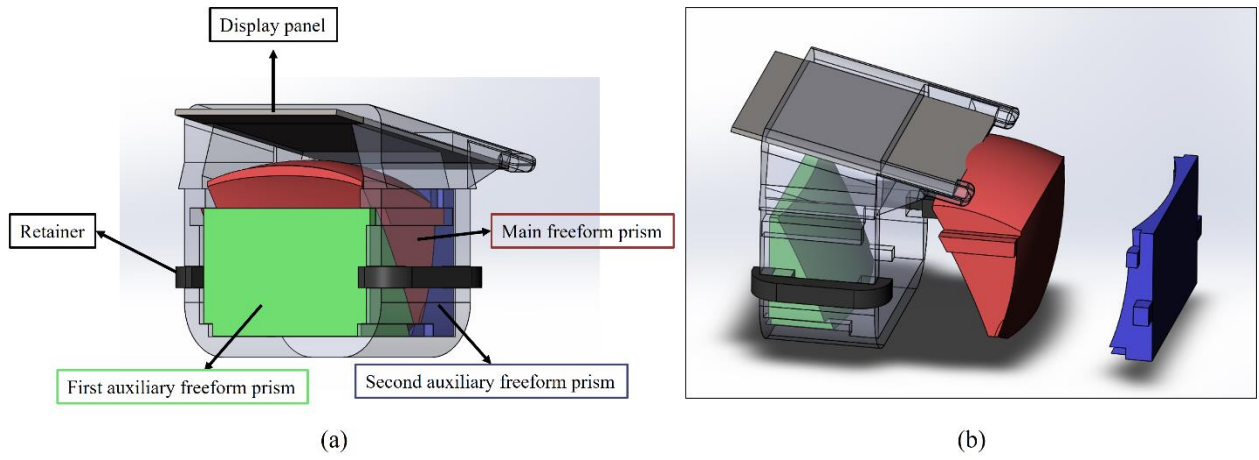


Fig. 5.17 (a) Mounting of the statically foveated freeform OST-HMD; (b) Exploded view of it.

6. CONCLUSION AND FUTURE WORK

6.1 DISCUSSION

The distinction between the two types of foveation schemes, namely the statically continuous degradation scheme and the dynamic dual-resolution scheme, primarily revolves around two key aspects: the hardware structure and the delivered qualities of perceived performance and data saving efficiency.

The dynamic dual-resolution foveation scheme typically necessitates dual displays and optical paths, as well as an essential gazing device and a 2D scanner. In contrast, the statically foveation scheme can be accomplished with a single display without the need for an eye-tracker or scanner. However, in the context of recent VR or AR products, eye tracking devices or even face tracking devices are essential not only for user calibration, such as adjusting the wearing position and pupil distance, but also for various applications, like the creation of 3D digital faces for social software. It is worth noting that these tracking devices are typically small in size and can be easily integrated into the frame of the device. The real challenge for dynamic dual-resolution foveation technology lies in the structure of multiple optical paths and the incorporation of multiple displays, which significantly increases the design complexity and overall system size. Particularly for OST-HMDs, the integration of at least three optical paths becomes necessary. On the other hand, the statically foveated display simplifies the structure to a great extent. However, the dual-resolution foveated display can achieve higher resolution within the fovea region using two display panels with relatively lower pixel counts. In contrast, a high-resolution display panel is usually required for

the statically foveated display. Nevertheless, these advantages of the dual-resolution foveation scheme are gradually diminishing with the advancements in display technology.

When considering the perceived performance and data saving efficiency, the dynamic dual-resolution foveated display emerges as a more ideal solution, particularly due to the practical limitations in designing statically foveated displays that prevent achieving significant optical power variation from the center field to the edge field, thereby hindering data saving as suggested by the theoretical model. However, statically foveated displays can provide competitive perceived performance within the region of frequent eye movements. Although perceived performance degraded as the field angle increases, but through careful control, the degradation can be minimally perceivable or at least visually still acceptable within the regions reachable via eye movements but low-frequency. Although the data saving efficiency of the dynamic dual-resolution foveation scheme is clearly advantageous compared to the static scheme, the statically foveated display still significantly reduces bandwidth requirements than the conventional sampling method without inducing additional optical paths or sources.

While the statically foveated display for HMDs can achieve comparable performance within the range of eye movements and offers significant structural simplification compared to the dynamic dual-resolution foveated display, further optimization is required. First, to validate and evaluate the perceived performance as a function of field angle and gaze direction of the human eye, it is recommended to conduct human studies in addition to the evaluation with mathematical models. Additionally, there is a need to enhance data saving efficiency by achieving a substantial ratio of optical magnification change between the peripheral and fovea regions. This improvement would not only reduce the resolution requirements of the display but also have the potential to

increase the FOV even further. However, realizing such improvements through traditional eyepieces with lens groups or freeform optics presents challenges, thus necessitating the exploration of new structures or technologies for the desired outcome.

6.2 CONCLUSION

Foveated displays offer a potential solution to the trade-off between FOV and resolution in conventional displays. Previous works have explored dynamic discrete foveation methods, where a high-resolution foveated region follows the user's gaze while peripheral awareness is maintained through a lower-resolution region. In this dissertation, a novel perceptual-driven approach was presented aimed at overcoming the limitations of traditional multi-resolution foveated displays due to the complexity structure of multiple displays and optical paths, eye tracking device and scanning mechanism. By utilizing this approach, a statically foveated scheme is proposed that achieves nearly imperceptible or minimal perceived resolution degradation within the region of frequent eye movements, while simultaneously reducing system complexity to achieve lighter, smaller, and more cost-effective HMD systems. More specifically, it introduces performance metrics for evaluating image quality and data sampling efficiency, demonstrates the process of obtaining optimal foveation schemes for different applications, and validates the proposed approach through experimental demonstrations using a 4K monitor-based bench prototype. Based upon the perceptual-driven approach, this dissertation presents the design of statically foveated displays for immersive and OST-HMDs through careful control of optical magnification to achieve a spatially varying resolution distribution that closely matches the target foveation scheme. The dissertation provides a comprehensive discussion of the optimization methods and performance evaluation techniques employed in these designs. The prototype system for the immersive HMD design

achieves an 80-degree FOV and an angular resolution of 1.5 arcminutes per pixel in the foveated region using stock lenses and a customized aspherical lens, with both simulated and experimental results validating the outstanding image quality within the region of frequent eye movement. Similarly, the prototype system for the OST-HMD design achieves an 80-degree diagonal FOV and an angular resolution of 2 arcminutes per pixel in the foveated region using freeform prisms, with the simulated results also confirming the excellent performance.

6.3 FUTURE WORK

Future work can be done in the following areas:

1. Prototyping and testing the statically foveated freeform OST-HMD to validate its performance in practical applications. Additionally, objective and quantitative evaluations should be performed to compare the designed systems with HMDs that utilize rectangular sampling methods through user studies.
2. Conducting a comprehensive human eye study to evaluate the perceived performance of the foveated display, considering the field angle and gaze direction. This study can help determine the region of frequent eye movement and identify the optimal balance point between head motion and eye movement.
3. Exploring methods to achieve a larger spatial variation in optical power for the statically foveated display, surpassing the capabilities of the existing designs.
4. Investigating new structures and approaches for dynamic foveated displays, with a focus on integrating the perceptual-driven approach to further reduce system complexity.

REFERENCES

1. I. E. Sutherland, "A Head-Mounted Three Dimensional Display," in *Proceedings of the December 9-11, 1968, Fall Joint Computer Conference, Part I*, AFIPS '68 (Fall, Part I) (Association for Computing Machinery, 1968), pp. 757–764.
2. L. Jensen and F. Konradsen, "A review of the use of virtual reality head-mounted displays in education and training," *Educ. Inf. Technol.* **23**, 1515–1529 (2018).
3. H. Mäkinen, E. Haavisto, S. Havola, and J.-M. Koivisto, "User experiences of virtual reality technologies for healthcare in learning: An integrative review," *Behav. Inf. Technol.* **41**, 1–17 (2022).
4. P. Hock, S. Benedikter, J. Gugenheimer, and E. Rukzio, "Carvr: Enabling in-car virtual reality entertainment," in *Proceedings of the 2017 CHI Conference on Human Factors in Computing Systems* (2017), pp. 4034–4044.
5. L. Chan and K. Minamizawa, "FrontFace: facilitating communication between HMD users and outsiders using front-facing-screen HMDs," in *Proceedings of the 19th International Conference on Human-Computer Interaction with Mobile Devices and Services* (2017), pp. 1–5.
6. C. Vieri, G. Lee, N. Balram, S. H. Jung, J. Y. Yang, S. Y. Yoon, and I. B. Kang, "An 18 megapixel 4.3 "1443 ppi 120 Hz OLED display for wide field of view high acuity head mounted displays," *J. Soc. Inf. Disp.* **26**, 314–324 (2018).
7. Z. Liu, C.-H. Lin, B.-R. Hyun, C.-W. Sher, Z. Lv, B. Luo, F. Jiang, T. Wu, C.-H. Ho, and H.-C. Kuo, "Micro-light-emitting diodes with quantum dots in display technology," *Light*

- Sci. Appl. **9**, 83 (2020).
8. M. Hoppe and J. E. Melzer, "Optical tiling for wide-field-of-view head-mounted displays," in *Current Developments in Optical Design and Optical Engineering VIII* (SPIE, 1999), Vol. 3779, pp. 146–153.
 9. D. Cheng, Y. Wang, H. Hua, and J. Sasian, "Design of a wide-angle, lightweight head-mounted display using free-form optics tiling," *Opt. Lett.* **36**, 2098–2100 (2011).
 10. W. Song, D. Cheng, Z. Deng, Y. Liu, and Y. Wang, "Design and assessment of a wide FOV and high-resolution optical tiled head-mounted display," *Appl. Opt.* **54**, E15–E22 (2015).
 11. "Science: Second Sight," *Time* (1962).
 12. "https://en.wikipedia.org/wiki/Virtual_reality.," .
 13. P. C. Thomas and W. M. David, "Augmented reality: An application of heads-up display technology to manual manufacturing processes," in *Hawaii International Conference on System Sciences (ACM SIGCHI Bulletin, 1992)*, Vol. 2, pp. 659–669.
 14. W. S. Geisler and J. S. Perry, "Real-time foveated multiresolution system for low-bandwidth video communication," in *Human Vision and Electronic Imaging III* (SPIE, 1998), Vol. 3299, pp. 294–305.
 15. L. Loschky, G. McConkie, J. Yang, and M. Miller, "The limits of visual resolution in natural scene viewing," *Vis. cogn.* **12**, 1057–1092 (2005).
 16. L. C. Loschky and G. S. Wolverton, "How late can you update gaze-contingent multiresolutional displays without detection?," *ACM Trans. Multimed. Comput. Commun. Appl.* **3**, 1–10 (2007).

17. W. S. Geisler, J. S. Perry, and J. Najemnik, "Visual search: The role of peripheral information measured using gaze-contingent displays," *J. Vis.* **6**, 858–873 (2006).
18. M. Dorr, T. Martinetz, M. Böhme, and E. Barth, "Visibility of temporal blur on a gaze-contingent display," in *Proceedings of the 2nd Symposium on Applied Perception in Graphics and Visualization* (2005), pp. 33–36.
19. D. J. Parkhurst and E. Niebur, "Variable-resolution displays: A theoretical, practical, and behavioral evaluation," *Hum. Factors* **44**, 611–629 (2002).
20. L. C. Loschky and G. W. McConkie, "Investigating spatial vision and dynamic attentional selection using a gaze-contingent multiresolutional display.," *J. Exp. Psychol. Appl.* **8**, 99–117 (2002).
21. T. Ienaga, K. Matsunaga, K. Shidoji, K. Goshi, Y. Matsuki, and H. Nagata, "Stereoscopic video system with embedded high spatial resolution images using two channels for transmission," in *Proceedings of the ACM Symposium on Virtual Reality Software and Technology* (2001), pp. 111–118.
22. Z. Wang and A. C. Bovik, "Embedded foveation image coding," *IEEE Trans. image Process.* **10**, 1397–1410 (2001).
23. M. Böhme, M. Dorr, T. Martinetz, and E. Barth, "Gaze-contingent temporal filtering of video," in *Proceedings of the 2006 Symposium on Eye Tracking Research & Applications* (2006), pp. 109–115.
24. H. R. Wu and K. R. Rao, *Digital Video Image Quality and Perceptual Coding* (CRC press, 2017).
25. A. T. Duchowski and A. Çöltekin, "Foveated gaze-contingent displays for peripheral LOD

- management, 3D visualization, and stereo imaging," *ACM Trans. Multimed. Comput. Commun. Appl.* **3**, 1–18 (2007).
26. D. Luebke and B. Hallen, "Perceptually driven simplification for interactive rendering," in *Rendering Techniques 2001: Proceedings of the Eurographics Workshop in London, United Kingdom, June 25–27, 2001 12* (Springer, 2001), pp. 223–234.
 27. H. A. Murphy, A. T. Duchowski, and R. A. Tyrrell, "Hybrid image/model-based gaze-contingent rendering," *ACM Trans. Appl. Percept.* **5**, 1–21 (2009).
 28. G. Sandini, P. Questa, D. Scheffer, B. Diericks, and A. Mannucci, "A retina-like CMOS sensor and its applications," in *Proceedings of the 2000 IEEE Sensor Array and Multichannel Signal Processing Workshop. SAM 2000 (Cat. No. 00EX410)* (IEEE, 2000), pp. 514–519.
 29. D. V Wick, T. Martinez, S. R. Restaino, and B. R. Stone, "Foveated imaging demonstration," *Opt. Express* **10**, 60–65 (2002).
 30. J. I. Katz, S. Lee, and H. Hua, "Improved multi-resolution foveated laparoscope with real-time digital transverse chromatic correction," *Appl. Opt.* **59**, G79–G91 (2020).
 31. K. Iwamoto, S. Katsumata, and K. Tanie, "An eye movement tracking type head mounted display for virtual reality system: evaluation experiments of a prototype system," in *Proceedings of IEEE International Conference on Systems, Man and Cybernetics* (IEEE, 1994), Vol. 1, pp. 13–18.
 32. J. P. Rolland, A. Yoshida, L. D. Davis, and J. H. Reif, "High-resolution inset head-mounted display," *Appl. Opt.* **37**, 4183–4193 (1998).
 33. G. Tan, Y.-H. Lee, T. Zhan, J. Yang, S. Liu, D. Zhao, and S.-T. Wu, "Foveated imaging

- for near-eye displays," *Opt. Express* **26**, 25076–25085 (2018).
34. B. Greenberg, "EyeWay Vision: Highly Efficient Immersive AR Glasses Using Gaze-locked Exit Pupil Steering," in *SPIE AVR21 Industry Talks II* (SPIE, 2021), Vol. 11764, p. 117641P.
 35. J. Kim, Y. Jeong, M. Stengel, K. Aksit, R. A. Albert, B. Boudaoud, T. Greer, J. Kim, W. Lopes, and Z. Majercik, "Foveated AR: dynamically-foveated augmented reality display.," *ACM Trans. Graph.* **38**, 91–99 (2019).
 36. S. Lee, M. Wang, G. Li, L. Lu, Y. Sulai, C. Jang, and B. Silverstein, "Foveated near-eye display for mixed reality using liquid crystal photonics," *Sci. Rep.* **10**, 16127 (2020).
 37. C. Yoo, J. Xiong, S. Moon, D. Yoo, C.-K. Lee, S.-T. Wu, and B. Lee, "Foveated display system based on a doublet geometric phase lens," *Opt. Express* **28**, 23690–23702 (2020).
 38. H. Hua and S. Liu, "Dual-sensor foveated imaging system," *Appl. Opt.* **47**, 317–327 (2008).
 39. Y. Qin and H. Hua, "Continuously zoom imaging probe for the multi-resolution foveated laparoscope," *Biomed. Opt. Express* **7**, 1175–1182 (2016).
 40. P. Lyu and H. Hua, "Perceptual-driven approach to statically foveated head-mounted displays," *Opt. Express* **29**, 33890–33914 (2021).
 41. J. Schwiegerling, "Field guide to visual and ophthalmic optics," in (Spie Bellingham, Washington, USA, 2004).
 42. R. Burgess-Limerick, M. Mon-Williams, and V. L. Coppard, "Visual display height," *Hum. Factors* **42**, 140–150 (2000).
 43. G. Cook and L. Stark, "Derivation of a model for the human eye-positioning mechanism,"

- Bull. Math. Biophys. **29**, 153–174 (1967).
44. P. Lyu and H. Hua, "Design of a statically foveated display based on a perceptual-driven approach," *Opt. Express* **31**, 2088–2101 (2023).
 45. D. Cheng, Y. Wang, H. Hua, and M. M. Talha, "Design of an optical see-through head-mounted display with a low f-number and large field of view using a freeform prism," *Appl. Opt.* **48**, 2655–2668 (2009).
 46. X. Hu and H. Hua, "Design and tolerance of a free-form optical system for an optical see-through multi-focal-plane display," *Appl. Opt.* **54**, 9990–9999 (2015).
 47. D. Cheng, J. Duan, H. Chen, H. Wang, D. Li, Q. Wang, Q. Hou, T. Yang, W. Hou, and D. Wang, "Freeform OST-HMD system with large exit pupil diameter and vision correction capability," *Photonics Res.* **10**, 21–32 (2022).

APPENDIX A: PERCEPTUAL-DRIVEN APPROACH TO STATICALLY
FOVEATED HEAD-MOUNTED DISPLAYS

Pengyinjie Lyu, and Hong Hua

This paper was published in Optics Express, Vol. 29, No. 21, pp. 33890- 33914 (2021)

Perceptual-driven approach to statically foveated head-mounted displays

PENGYINJIE LYU AND HONG HUA* 

3D Visualization and Imaging Systems Laboratory, College of Optical Sciences, University of Arizona,
1630 East University Boulevard, Tucson 85721, USA
*hhua@optics.arizona.edu

Abstract: A foveated display is a promising technique to realize displays offering both a large field of view (FOV) and high spatial resolution. Although several prior works have attempted to apply a foveation method to the design of a head-mounted display (HMD) system, the common method is based on a dual-resolution dynamic foveation scheme which is inevitably complex and has a high cost due to the requirements for multiple display sources, a 2D steering mechanism, and eye tracker. In this paper, a new perceptual-driven approach to the design of a statically foveated HMD is proposed with the goal of offering a wide FOV across which the degradation of the perceived image resolution is nearly imperceptible or minimal within regions of frequent eye movements. Compared to a dual-resolution discrete and dynamic foveation approach in the prior art, the static foveation approach will not only maintain resolution continuity but also eliminate the need for a scanning mechanism, multiple display sources, and an eyetracker, and therefore minimize hardware complexity. We present the general approach for creating a static foveation scheme, performance metrics for evaluating the perceived image quality, and the process of optimizing a foveation scheme to meet different requirements. Finally, we experimentally demonstrate and validate the proposed foveation scheme using a testbed system. Overall, we demonstrate a statically foveated scheme is capable of offering a display with a total 160° FOV, a constant resolution of 0.5 or 1 arcminutes per pixel within the $\pm 10^\circ$ region where frequent eye movements occur, an adequate resolution no less than 45% of peak resolution within the parafovea region of $\pm 30^\circ$, and a data sampling efficiency as high as 90%.

© 2021 Optical Society of America under the terms of the [OSA Open Access Publishing Agreement](#)

1. Introduction

Conventional head-mounted displays (HMD) adopt the well-established rectilinear sampling method for 2D display and imaging systems where a finite number of pixels are spread evenly across an entire field of view (FOV), thus are subject to the inherent trade-off between their FOV and spatial resolution. For a given number of available pixels, the larger is the FOV, the lower the angular resolution. Consider an HMD design with a high-definition (HD) display of 1920×1200 pixels. The angular resolution is about 3.75 arc minutes per pixel for a design spreading the 1920 pixels evenly across an FOV of 120° in the horizontal direction. Based on the same sampling method, achieving an angular resolution of 1 arc minutes per pixel for the same FOV would require a display of 7200×4500 pixels and require a data bandwidth 14 times of a typical HD device. Such high-resolution displays are not only very challenging to produce, but also computationally challenging to process, transfer, and store such images. Besides these technical challenges, the rectilinear sampling scheme is very inefficient, leading to a large amount of redundant data for the human visual system (HVS) because the visual acuity (VA) of the human eye drops drastically beyond the fovea region on retina. For instance, a 4 K display based on a rectilinear sampling scheme can only support an HMD of 66° circular FOV to achieve 1 arc minute angular resolution, while over 88% of the rendered information is not perceived by the human visual system at a given time instance.

To mitigate the trade-off between FOV and resolution, a foveated display, inspired by the foveation properties of human eyes, can be generally characterized as a method that identifies a users' region of interest (ROI) and allocates the limited resources, such as a finite number of pixels or data processing and transmission bandwidth, differently between the ROI and the peripheral area outside the ROI region. For example, the number of pixels allocated to a display region is a function of its distance to the center of the ROI. The ROI may be determined by means of a gaze tracker, by tracking the salient points of the scene rendered by the display, by pre-determining the ROIs of the scene, or by other mechanisms.

Many efforts have been made to explore foveation techniques in imaging and display applications and they fall into one of three categories. The first category is experimental research to understand visual processing and perceptual artifacts, such as perceptible image blur and image motion, when viewing software-simulated foveated images [1]. The second category is an algorithmic approach in which foveation techniques are applied primarily to spatially variant image processing and video encoding [2] and variable levels of detail graphics rendering [3–5] to achieve real-time video communication and save data processing resources. In this approach, the display or imaging sensor hardware has a uniform high resolution, but the resolution of the rendered image decreases as it deviates away from the attended ROI. The third category of work takes a hardware approach, in which various imaging sensors or displays with spatially varying resolution are developed to reduce the requirements for high-resolution detectors and displays or high-quality and complex optical systems. For example, Sandini et al. demonstrated a retina-like image sensor characterized by spatially variant resolution similar to that of the human retina and demonstrated that 35 times fewer pixels were needed in the spatially variant resolution sensor as compared with a constant high-resolution image of 1100×1100 pixels [6]. Wick et al. presented the designs of foveated imaging systems in which a spatial light modulator (SLM) was used to dynamically correct the optical aberrations of a simple wide FOV optics at the region of interest [7]. Hua and Liu demonstrated a dual-sensor foveated imaging system where two separate imaging paths, one for foveal and one for peripheral vision, were integrated to capture foveated images and the high-resolution imaging path was steered by a 2D scanner according to the ROI [8]. Qin and Hua applied the dual-sensor architecture to develop multi-resolution foveated laparoscopes for minimally invasive surgery [9]. Iwamoto et al. demonstrated a bench prototype of a foveated display which dynamically scans a high-resolution inset image over a wide FOV low-resolution background display through 2D opto-mechanical scanners [10]. Rolland et al. reported the conceptual design of a high-resolution inset HMD system, in which a pair of microlens arrays optically duplicates a high-resolution inset image over a background display and a liquid crystal shutter is used to select one of the copies corresponding to the gazed ROI [11]. More recently, Tan et al. demonstrated a dual-resolution HMD design with two display panels of different optical magnifications as the image sources and a switchable Pancharatnam-Berry phase deflector for shifting the position of the foveated view [12]. Boris Greenberg reported a foveated HMD design based on a direct retinal projection method integrated with eyetracking, two dual-axis microelectro-mechanical system scanners, and two laser sources offering different scanline densities [13].

Among the prior works that attempted to apply a foveation method to the hardware design of an HMD system [10–13], the common method for implementing a foveated HMD is a dynamic discrete foveation approach where a foveated region offering a high image resolution is dynamically steered in response to a user's gaze direction and a relatively low-resolution region offers peripheral awareness. Such dynamic foveation method typically utilizes a dual-display architecture in which two displays of different pixel resolutions or two different optical paths of different optical magnifications are utilized to render the foveated and peripheral areas, respectively. The foveated area with a higher resolution typically covers a small FOV while the peripheral area with a substantially lower resolution covers a large portion of the entire FOV. In a

dynamically foveated display, an eye tracking is typically required to track the line of sight of a viewer and thus determine the instantaneous ROI toward which the display of higher resolution is aimed. Finally, a dynamically foveated display requires a scanning method to mechanically [10,13] or optically [11,12] steer and align the high-resolution foveated display approximately with the viewer's line of sight to achieve the goal of foveated rendering. Consequently, such dynamically foveated display is inevitably complex, high cost, large volume, and heavy weight because multiple displays and imaging paths are necessary to render multi-level resolution displays, an eye tracking device is required to track ROI, and a 2D steering mechanism, either mechanical or optical, is required for steering the foveated region. Finally, the multi-resolution approach provides multiple discrete samples of resolution and thus discontinuous perception of image quality as eye moves, leading to visual artifacts.

In this paper, we explore a new perceptual-driven approach to the design of statically foveated HMDs with the goal of offering a wide FOV across which the degradation of the perceived image resolution may be minimal during the course of eye movement and the perceivable image artifacts and image resolution discontinuity are minimized. Compared to the multi-level discrete and dynamic foveation approach in the prior art, the static foveation approach will not only maintain resolution continuity, but also eliminate the need for an eyetracker or scanning mechanism and therefore minimize hardware complexity. The rest of the paper is organized as follows. Section 2 presents the perceptual-driven approach, Section 3 describes the methods for evaluating the data sampling efficiency and perceived image resolution and quality as a function of eye gaze direction, Section 4 demonstrates the process of optimizing foveation schemes to meet the requirements of different applications and hardware constraints, Section 5 presents the assessment of an optimized foveation scheme by applying the proposed performance metrics, and finally Section 6 experimentally demonstrates the validation and assessments of the static foveation scheme through a testbed.

2. Perceptual-driven design of statically foveated displays

In the human visual system (HVS), only a narrow region around the fovea offers exceptional resolution, contrast, and color sensitivities, while these properties fall off rapidly with an increasing retinal eccentricity which is defined as the angular distance of a field point from the fovea center. The object field along a viewer's line of sight (LoS) is imaged at the fovea center and the HVS adapts its LoS to be centered with the attended ROI through eye or head movements. Due to such inherent capability of dynamic gazing, we often anticipate that a foveated display is able to allocate its finite number of pixels in such a fashion that its angular pixel density follows the same distribution function as that of the photoreceptors on a human retina and is able to dynamically steer its high pixel density region, referred to as the foveated region of the display, such that it is always centered at the fovea of the retina within the limits of eye movements. As summarized in the previous section, a few examples of dynamically foveation display schemes have been demonstrated based on a dual-display architecture accompanied by either 2D opto-mechanical or optical scanners [10–13]. Such dynamic foveation scheme, however, takes too much toll on the hardware complexity and may yield perceivable artifacts of resolution discontinuity.

Motivated by the fact that an HMD is generally attached to a user's head with a relatively fixed viewing position, we propose a perceptual-driven static foveation approach where the characteristics of eye and head motions and the perceived visual effects are taken into account such that the degradation of the perceived quality of a statically foveated display may be imperceptible or minimal during the course of eye movements. Figure 1(a) shows a schematic illustration of a statically foveated display where the display plane is the conjugate virtual image of a display source seen by a viewer through the optics in an HMD system. Figure 1(b) plots an example of the resolution distribution for such a display as a function of field angles. For convenience, a

reference coordinate system, OXYZ, is defined in the visual space as shown in Fig. 1(a). The origin O is located at the center of the entrance pupil of the right eye; the Z axis coincides with the corresponding LoS when the eye gaze direction is parallel to the head pose direction (in other words, no eye movements are engaged in both horizontal and vertical directions and the eye is gazing naturally straight forward); the OXY plane is perpendicular to the Z-axis, and the Y axis is pointing upward. For simplicity, the virtual display plane is assumed to be perpendicular to the Z-axis and a display reference coordinate system, IX'Y'Z', is defined where the origin I is the intersection of the Z-axis of the OXYZ reference with the display plane, and the X', Y', and Z' axes are parallel to the X-, Y, and Z-axes, respectively. The display plane is displaced from the OXY plane by a distance L along the Z-axis, where L corresponds to the virtual display distance in an HMD system. A pixel position, P, on the virtual display plane can be uniquely defined by its corresponding field angle, θ , to the reference center I or equivalently the angular deviation of the pixel from the Z-axis of the OXYZ reference system. θ_x and θ_y correspond to the X-component and Y-component of the field angle θ in the horizontal and vertical directions, respectively.

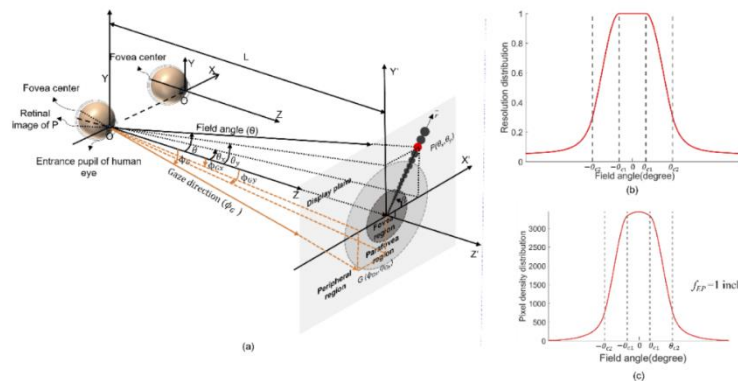


Fig. 1. (a) The schematic illustration of a continuously foveated display where its angular resolution varies as a function of the field angle θ and symmetric about the display center I; (b) Example of an angular resolution distribution function along a given direction crossing the display center I as a function of the field angle; (c) Example of a pixel density distribution function on a microdisplay as a function of the field angle with an eyepiece optics of 1-inch focal length.

Unlike a display based on a rectilinear sampling method, the virtual pixel pitch, p , on the display plane increases as the distance of the pixel from the display center, I, increases. Along a given radial direction, as the pixel position, P, deviates away from the center I, the pixel density of the display monotonically decreases and the angular resolution degrades. Here the pixel density is defined as the number of pixels per unit distance, while the angular resolution is defined as the visual angle subtended by a single pixel to the eye.

As illustrated in Fig. 1(a), the display plane may be divided into three functional regions, a fovea region, a parafovea region, and a peripheral region. Without loss of generality, we assume all three regions are rotationally symmetrical and centered with the display center I. Similar to the fovea of the retina, the fovea region of the display is statically fixed at the center region of the display and offers the highest pixel resolution. It shall offer a small and uniform or nearly uniform pixel pitch to ensure high angular resolution when the eye gaze direction falls within this region. The fovea region is bounded by a critical field angle, θ_{c1} , which is considered as the visual and

musculoskeletal balance point and defines a central region for frequent and comfortable eye movements. Based on the physiological characteristics of eye movements, a preferred choice for θ_{c1} , is between 5 and 20. For instance, Burgess-Limerick et al. reported that comfortable eye movements occur within a field angle of $\pm 15^\circ$ for a good compromise between visual and musculoskeletal needs [14]. The parafovea region of the display is immediately adjacent to the fovea region and offers a medium rate of degradation in resolution. The parafovea region is the annular zone bounded by two critical field angles, θ_{c1} and θ_{c2} , which are considered as the balance points between eye movements and head motion. Within the angular range of $\pm(\theta_{c1}, \theta_{c2})$, eye movements are expected to be gradually less preferred than an alternative choice of head motion due to muscular strain and discomfort [14]. A preferred choice for θ_{c2} is between 20 and 40. Cook and Stark reported that head motion instead of eye movements likely occurs when the field angle is greater than 30° [15]. The virtual pixel pitch within the angular range of $\pm(\theta_{c1}, \theta_{c2})$ is expected to increase monotonically at a rate such that the angular resolution is still relatively high when the eye is gazed within this region. The peripheral region of the display is immediately next to the parafoveal region for field angles greater than $\pm\theta_{c2}$. It offers a rapid rate of degradation in resolution and mainly serves the purpose of peripheral vision and the sense of immersion. Within this region, we anticipate that comfortable eye movements unlikely occur and head or body motion is preferred. In an HMD system, a head tracker can be utilized for updating the scene rendering according to head motion without change of the relative position of the eye gaze to the display field. Therefore, eye gaze direction much less likely falls within the peripheral region. More control points may be added to further divide the peripheral region as needed by specific applications of the proposed scheme.

The pixel distribution of a foveated display can be characterized by the angular resolution distribution function, denoted as $F_{FD}(\theta_x, \theta_y)$, which is defined as the reciprocal of the angular resolution of the display in minutes of arc, where θ_x and θ_y correspond to the X-component and Y-component of the field angle θ in the horizontal and vertical directions, respectively. Based on the division of the functional regions described above, the angular resolution distribution of a statically-foveated display may be expressed as

$$F_{FD}(\theta_x, \theta_y) = \begin{cases} f_1(\theta_x, \theta_y) & |\theta| \leq \theta_{C1} \\ f_2(\theta_x, \theta_y) & \theta_{C1} < |\theta| \leq \theta_{C2} \\ f_3(\theta_x, \theta_y) & \theta_{C2} < |\theta| \leq \theta_{\max} \end{cases}, \quad (1)$$

where f_1 , f_2 , and f_3 are the segmented functions that characterize the resolution distribution within each corresponding region, and θ_{\max} is the maximum field angle in a radial direction. Figure 1(b) schematically illustrated the resolution distribution function (angular pixel density), F_{FD} , along a radial direction \vec{r} as a function of the field angle, θ . In this example, the rate of resolution degradation, which is characterized by the slope of the resolution distribution curve, vary with the field position. One of the distinct features of the proposed scheme compared to the prior dual-resolution foveation scheme is its ability to ensure continuous change of resolution distribution. To ensure resolution continuity and image smoothness along the boundaries of a foveated display, the function values and the derivatives at the first and second critical balance points, θ_{C1} and θ_{C2} , need to be equal. In other words, the following conditions shall be satisfied:

$$\begin{aligned} f_1(|\theta_{C1}|) &= f_2(|\theta_{C1}|) & \text{and} & & f_2(|\theta_{C2}|) &= f_3(|\theta_{C2}|) \\ f_1'(|\theta_{C1}|) &= f_2'(|\theta_{C1}|) & & & f_2'(|\theta_{C2}|) &= f_3'(|\theta_{C2}|) \end{aligned} \quad (2)$$

The angular resolution distribution in Eq. (1) is independent of the virtual display distance to a viewer and characterizes a viewer's visual experiences. The pixel density, characterized by the number of pixels per unit distance, is commonly used as an engineering parameter for measuring

the spatial resolution of a 2D display and provides direct guidance on hardware requirements. The virtual pixel pitch, p , measured in millimeters on the virtual display plane for a given field angle θ can be obtained from the resolution distribution in Eq. (1) as

$$p_{VD}(\theta_x, \theta_y) = \frac{L \cdot \tan\left(\frac{1}{60 \cdot F_{FD}(\theta_x, \theta_y)}\right)}{\cos^2 \theta}, \quad (3)$$

where L is the distance between the virtual display plane and the eye. The corresponding pixel density distribution per inch (PPI) on the virtual display plane is described as

$$PPI_{VD}(\theta_x, \theta_y) = \frac{25.4 \cos^2 \theta}{L \cdot \tan\left(\frac{1}{60 \cdot F_{FD}(\theta_x, \theta_y)}\right)}. \quad (4)$$

To guide the optical design, it is preferable to convert the PPI measurement on the virtual display to the PPI on a microdisplay panel to be optically magnified by an eyepiece. Let us consider an eyepiece with a constant optical power with a focal length of f_{EP} , the pixel density distribution per inch on the microdisplay plane can be obtained as

$$PPI_{MD}(\theta_x, \theta_y) = \frac{25.4 \cos^2 \theta}{f_{EP} \cdot \tan\left(\frac{1}{60 \cdot F_{FD}(\theta_x, \theta_y)}\right)}. \quad (5)$$

The pixel pitch for at the center field is $f_{EP} \cdot \tan\left(\frac{1}{60 \cdot F_{FD}(0,0)}\right)$. As an example, Fig. 1(c) plots the microdisplay pixel density distribution for the resolution distribution function illustrated in Fig. 1(b), where the eyepiece focal length is assumed to be 1 inch. Practically, instead of requiring a microdisplay panel with spatially varying pixel density distribution characterized by Eq. (5), we can adopt microdisplay panels with uniform pixel pitch, p_0 , and carefully design an eyepiece with spatially varying optical power, Φ_{EP} , characterized as

$$\Phi_{EP}(\theta_x, \theta_y) = \frac{1}{f_{EP}(\theta_x, \theta_y)} = \frac{\tan\left(\frac{1}{60 \cdot F_{FD}(\theta_x, \theta_y)}\right)}{p_0 \cos^2 \theta}. \quad (6)$$

3. Performance metrics for evaluating a foveated display

In general, many forms of resolution distribution functions may be utilized for implementing the proposed static-foveation method, but carefully optimized functions can lead to minimally perceivable quality degradation or more data saving or ease of implementation. One of the key aspects of optimization is to develop adequate quality metrics that can be utilized to evaluate the performance and artifacts of different resolution distribution functions and to establish meaningful merit values functions to obtain optimal function forms that meet the requirements of different applications. This section will present two types of the proposed performance metrics, one focusing on evaluating perceived image quality variations, and the other focusing on data saving efficiency.

3.1. Perceived visual acuity of a foveated display

The key hypothesis of a statically-foveated display is that we anticipate that eye movements occur frequently in the fovea region and much less frequently in the parafovea region. Therefore, evaluating the visual quality of such a display needs to account for the dynamics of eye movements and the visual acuity (VA) characteristics of the human visual system. A perception-driven quality metric is to find an optimal resolution distribution for a statically-foveated display scheme such that the resulted display offers nearly imperceptible resolution degradation within the fovea region and small degradation within the parafovea region when a viewer's eye is gazing at the

corresponding regions. To achieve this goal, we characterize the perceived visual acuity of a display, also known as the perceived resolution, as a function of its field angle and eye gaze direction by factoring the visual acuity of a 20/20 standard observer and the resolution distribution of the display.

As illustrated in Fig. 1(a), let us consider the eye is gazing at a point G on the display plane. The gaze direction ϕ_G is the angle of eye rotation with respect to the Z-axis, and ϕ_G may be decomposed into two orthogonal components, (ϕ_{Gx}, ϕ_{Gy}) , corresponding to the X-component and Y-component eye rotations in the horizontal and vertical directions, respectively. The relative visual acuity (VA) of the HVS, denoted as VA_{HVS} , describes the resolution distribution as a function of the eccentricity angle of a given visual field from the eye gaze direction, and is defined as the normalized reciprocal of the angular resolution in minutes of arc and may be modeled as [16,17]

$$VA_{HVS}(\theta_x, \theta_y, \phi_{Gx}, \phi_{Gy}) = e_2 / (e_2 + \sqrt{(\theta_x - \phi_{Gx})^2 + (\theta_y - \phi_{Gy})^2}), \quad (7)$$

where $e_2 \cong 2.3^\circ$. The eccentricity angles, (e_x, e_y) , of the given field from the fovea center are given as $e_x = \theta_x - \phi_{Gx}$ and $e_y = \theta_y - \phi_{Gy}$ in the horizontal and vertical directions, respectively.

The perceived visual acuity of a foveated display, denoted as, VA_{FD} , for a given field angle θ varies with the eye gaze direction, ϕ_G , and is determined by obtaining the smaller one between the values of the display resolution distribution and the VA curve of a 20/20 standard observer depicted by Eq. (7). Generally, it can be expressed as

$$VA_{FD}(\theta_x, \theta_y, \phi_{Gx}, \phi_{Gy}) = \min[F_{FD}(\theta_x, \theta_y), VA_{HVS}(\theta_x, \theta_y, \phi_{Gx}, \phi_{Gy})]. \quad (8)$$

For a conventional single-resolution display offering a uniform pixel sampling across its entire FOV, its perceived visual acuity is a constant, independent of eye gaze direction. For instance, for a display that matches the fovea resolution of a 20/20 standard observer (i.e. 1 arcmin per pixel), its perceived VA for a 20/20 standard observer can be characterized as $VA_{FD}(\theta_x, \theta_y, \phi_{Gx}, \phi_{Gy}) \equiv 1$. For a foveated display, however, its perceived VA varies with gaze direction. Figure 2 illustrates an example of modeling the perceived VA of a foveated display in which the resolution distribution (in solid red line) is a simple Gaussian function, $F_{FD}(\theta) = e^{-0.001 \times \theta^2}$, to describe a rotationally symmetric foveated scheme with its peak centered on the field angle of 0 (i.e. the Z-axis). In this example, the eye is gazed at a 40° angle away from the center and the VA of the HVS given by Eq. (7) is plotted in black solid line. The perceived VA of the display under this gaze condition is obtained by applying Eq. (8) and is plotted by the yellow line with "*" markers. The yellow-shaded area under the yellow curve indicates the region where the perceived image quality is as high as the VA of the observer and the black-shaded area illustrates the region where the perceived image quality is limited by the display resolution rather than by the VA of the observer. In this example, at a 40° eye gaze angle, the maximum perceived VA value is about 0.31, occurring at the 34° field angle. The display outperforms on the left side of the 34° peak and underperforms on the right side.

Further analytical metrics can be computed from the perceived resolution in Eq. (8) to evaluate the perceived performance and make comparison among different distribution functions for foveated displays. For instance, the perceived maximum resolution of a display, denoted as $VA_{FD}|_{\max}$, is defined as the perceived maximum resolution across the overall FOV at different eye gaze directions to evaluate the perceived peak performance with respect to eye motion. It is expressed as

$$VA_{FD}|_{\max}(\phi_{Gx}, \phi_{Gy}) = \max[VA_{FD}(\theta_x, \theta_y, \phi_{Gx}, \phi_{Gy})]. \quad (9)$$

Clearly, an ideal foveated display with $VA_{FD}|_{\max}(\phi_{Gx}, \phi_{Gy})$ equal to or approaching to 1 is highly desirable for the region with active eye movements. Similarly, we can also define a summative metric, denoted as VR_{FD} , to assess whether the perceived resolution of a display is below the perceptible limit of the HVS by computing the ratio of the volume enclosed by the

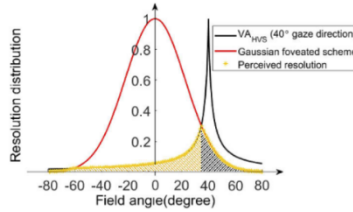


Fig. 2. Illustration of the perceived resolution of a foveated display with its resolution distribution function in the form of a simple Gaussian function while the eye is gazed in the direction of 40° away from the display center.

perceived resolution curve of a display to the volume enclosed by the VA curve of the HVS across the display FOV for different eye gaze directions. The volume ratio is defined as

$$VR_{FD}(\phi_{G_x}, \phi_{G_y}) = \frac{\int_{-\theta_{Xmax}}^{\theta_{Xmax}} \int_{-\theta_{Ymax}}^{\theta_{Ymax}} VA_{FD}^2(\theta_x, \theta_y, \phi_{G_x}, \phi_{G_y}) d\theta_x d\theta_y}{\int_{-\theta_{Xmax}}^{\theta_{Xmax}} \int_{-\theta_{Ymax}}^{\theta_{Ymax}} VA_{HVS}^2(\theta_x, \theta_y, \phi_{G_x}, \phi_{G_y}) d\theta_x d\theta_y}, \quad (10)$$

where θ_{Xmax} and θ_{Ymax} are the maximum half FOVs of the display system in the horizontal and vertical directions, respectively. This metric effectively evaluates the ratio between the whole volumes below the yellow curve and the black curve in Fig. 2. For a given eye gaze direction, a ratio of 1 indicates that the display performs to the limit of the HVS across its entire FOV and a ratio less than 1 indicates the display underperforms to the HVS limit at some field angles. The metrics defined in Eqs. (8) through (10) characterize the perceived resolution performance provided by a display as a function of its field angles and gaze directions.

3.2. Bandwidth and data sampling efficiency

One of the major objectives for a foveated display is to improve the sampling efficiency by allocating finite hardware sources such as limited display pixels or data bandwidth differently between the attended ROI of the peripheral area outside the ROI. By adopting the analytical method described by Hua and Liu in [8], the total amount of raw data rendered by a system can be calculated by integrating its resolution distribution across all fields, and can be expressed as

$$B = \int_{-\theta_{Xmax}}^{\theta_{Xmax}} \int_{-\theta_{Ymax}}^{\theta_{Ymax}} F_{FD}^2(\theta_x, \theta_y) d\theta_x d\theta_y. \quad (11)$$

The metric in Eq. (11) measures the bandwidth requirement of a system. To evaluate and compare the relative data sampling efficiency of different foveation schemes, we consider a uniformly sampled, single-resolution display (SRD) as a reference where the SRD offers the same resolution across its entire FOV as the peak resolution of a foveated system, i.e. $F_{SRD}(\theta_x, \theta_y) = F_{FD}(0, 0)$. The data sampling efficiency of a foveated display (FD) is given as:

$$S_{FD} = \frac{B_{SRD} - B_{FD}}{B_{SRD}}. \quad (12)$$

Alternatively, as adopted in [8], the effective information throughput of a display may be evaluated against a reference system whose spatial resolution distribution represents the just-adequate resolvability required for its users. For instance, the visual acuity response of a standard observer with 20/20 vision can be utilized as the reference resolution distribution for evaluating

the efficiency of a display system. Displays with the same or better resolvability than that of a standard observer are considered to be perceptually equivalent. Compared against the reference system providing the same FOV and same peak resolution, the information throughput, E , of a given display scheme can be defined as:

$$E = \frac{\int_{-\theta_{x\max}}^{\theta_{x\max}} \int_{-\theta_{y\max}}^{\theta_{y\max}} F_{HVS}^2(\theta_x, \theta_y) d\theta_x d\theta_y}{\int_{-\theta_{x\max}}^{\theta_{x\max}} \int_{-\theta_{y\max}}^{\theta_{y\max}} F_{FD}^2(\theta_x, \theta_y) d\theta_x d\theta_y} = \frac{B_{HVS}}{B_{FD}}. \quad (13)$$

Hereby it is assumed that the center field of the display is aligned with the center of the reference system. Figure 3 plots the information throughputs of a SRD and a foveated display as a function of the overall FOV in logarithmic scale. In this example, a circular field of view is assumed. The foveated display assumes the same resolution distribution as the Gaussian distribution exemplified used in Fig. 2 with a peak resolution of 1 arc minute at the center field, while the SRD assume a uniform resolution of 1 arc minute across its entire FOV. Although the effective information throughputs for both the SRD and FD monotonically decrease with an increasing FOV, the ratio of throughput of the FD scheme to SRD increases rapidly. The throughput of a SRD is as low as $\sim 2\%$ for a system of 60° FOV and less than 1% for a 100° FOV, which suggest that the amount of redundant information produced by a 60° -FOV is nearly 47 times more than that of the perceptually equivalent system. On the other hand, the throughputs of a FD scheme with a Gaussian distribution are 4.4% and 4.9% for the same FOVs, respectively.

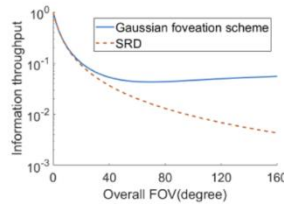


Fig. 3. Illustration of information throughputs of a SRD and a foveated display as a function of the overall FOV.

4. Optimization of a statically-foveated display scheme

The key for implementing the proposed method described in Sec. 2 is to optimize the choices of the critical balance points, θ_{C1} and θ_{C2} , as well as the resolution distribution functions for the different functional regions as defined in Eq. (1) by accounting for the statistic characteristics of eye and head motion, the perceived performance of a display as a function of eye motion and field angle characterized by Eqs. (8) through (10), and the relative data saving efficiency by Eq. (12). By considering the various factors and using the metrics and constraints described in Sec. 3, we adjusted the general forms of the segmented functions defined in Eq. (1) to obtain resolution distribution functions that offer a good balance among the factors such as maximum perceived resolution, the volume ratio, data saving efficiency, and overall FOV.

The optimization process starts with an initialization step, which consists of three key aspects, the initialization of the resolution distribution functions, target display specifications, and threshold performance metrics. The initialization of the resolution distribution functions requires choosing the general form of functions and the associated critical balance points and specifying the parametric space and range for optimization. It involves in several critical considerations for a statically-foveated display and will be detailed below. Target display specification provides not only

the performance requirements of a target display such as spatial resolution and field of view, but also hardware constraints such as total pixel counts and data bandwidth available. The threshold performance metrics specify the thresholds to determine if a given parametric combination yields a solution that satisfies target display specifications. Following the initialization step, each set of the parametric combinations within the specified range is evaluated by computing the performance metrics defined by Eq. (8) through (10) and its performance is compared against the corresponding threshold values to determine if it yields a viable solution. In the final step, the performance metrics for all the parametric combinations that yield satisfying solutions are compared against each other and an optimal resolution distribution is determined by selecting the parametric combination that offers both minimally perceptible VA degradation and maximal data saving efficiency within a given set of display hardware constraints and performance requirements.

The optimal solution to the resolution distribution of a statically-foveated display depends on the requirements of different applications. Hereby we demonstrate the optimization process outlined above through an example we implemented. The process began with choosing the function forms for the resolution distribution function defined in Eq. (1) for a foveated display. Though the function may take many different forms, our choice is based on considerations of perceived visual effects, generalization capability of results, simplicity of parametric space for optimization, and ease of implementation. First of all, a uniform or nearly uniform resolution is desired in the fovea region ($|\theta| \leq \theta_{C1}$) to ensure nearly imperceptible image quality degradation when the eye gaze is fixated within this region. Secondly, a segment of a Gaussian function is chosen to describe the resolution distribution within the parafovea region ($\theta_{C1} \leq |\theta| \leq \theta_{C2}$). Besides its simplicity, a Gaussian function provides not only an elegant approximation of the visual acuity degradation of the HVS given by Eq. (7), but also a statistical estimation of the eye motion probability within this region. More specifically, due to the increasing torque imposed to the eye muscles as the eye gaze angle increases, the possibility of eye fixation at large field angles decreases. Consequently, the resolution distribution of the parafovea region is expected to decrease as the field angle increases, and a lower rate of resolution degradation is expected for fields closer to the fovea region than that for fields further away. The rate of degradation with increasing field angles can be adjusted by optimizing the standard deviation of the Gaussian function. To ensure smooth transition across the boundary of the fovea and parafovea regions, the peak value of the selected Gaussian function shall match with the resolution of the threshold field angle of the fovea region. Finally, the resolution distribution for the peripheral region ($|\theta| > \theta_{C2}$) is modeled by the VA curve of the HVS at a large eccentricity angle with a polynomial correction function to make the curve continuous at the θ_{C2} . In summary, in our optimization process the general form of the resolution distribution function defined in Eq. (1) is modeled with rotational symmetry as

$$F_{FD}(\theta) = \begin{cases} F_0 & |\theta| \leq \theta_{C1} \\ F_0 e^{-\frac{(\theta-\theta_{C1})^2}{2\sigma^2}} & \theta_{C1} < |\theta| \leq \theta_{C2} \\ \frac{2.3F_0}{2.3+(\theta-\phi_{th})} + \Delta(\theta) & |\theta| > \theta_{C2} \end{cases}, \quad (14)$$

where F_0 is the reciprocal of the angular resolution at the display center, σ is the standard deviation of the Gaussian function, affecting the rate of resolution degradation within the parafovea region, and ϕ_{th} is a threshold eye gaze angle that determines the eccentricity of a field angle in the peripheral region and the rate of resolution degradation. $\Delta(\theta)$ is the polynomial correction function to make the third and the second segments of the resolution distribution function continuous at the θ_{C2} , where the specific order of the $\Delta(\theta)$ is determined by the value of σ , θ_{C1} , and θ_{C2} . It is worth noting that the third segment contributes little for the perceived performance and data sampling efficiency, so usually we can use as simple as a third-order polynomial function to express the $\Delta(\theta)$.

Although the σ value in Eq. (14) explicitly defines the rate of resolution degradation within the parafovea region, it does not intuitively quantify the relative image quality between the fovea and parafovea regions. Instead, the ratio, η ($0 < \eta \leq 1$), of the resolution corresponding to the parafovea critical field angle, θ_{C2} , to the resolution corresponding to the fovea critical angle θ_{C1} , is defined to quantify the relative image quality variation across the display. Its relationship with the standard deviation σ is expressed as:

$$\sigma = \frac{\theta_{C2} - \theta_{C1}}{\sqrt{-2 \ln \eta}}. \quad (15)$$

For instance, when σ equals to the angular size of the parafovea region (i.e. $\sigma = \theta_{C2} - \theta_{C1}$), the resolution ratio η equals to $1/\sqrt{e}$ and the resolution corresponding to the field angle θ_{C2} is about 60% of the resolution for the field angle θ_{C1} . Similarly, if σ is increased to twice as large, η equals to $1/e^2$ and the resolution for the field angle θ_{C2} is about 13.5% of the resolution for the field angle θ_{C1} . The higher the ratio η , the less quality degradation across the display, but the less data saving is expected.

To ensure resolution continuity at the boundary of the parafovea and peripheral regions, the threshold gaze angle defining the resolution distribution for the peripheral region, ϕ_{th} , is determined by matching the function values of the corresponding resolution distribution functions when $\theta = \theta_{C2}$, and the threshold gaze angle, ϕ_{th} , is obtained as

$$\phi_{th} = \theta_{C2} + 2.3(1 - \frac{1}{\eta}). \quad (16)$$

Based on Eq. (14), the key factors to optimize a statically foveated display include the two critical field angles, θ_{C1} and θ_{C2} , as well as the resolution ratio η . For simplicity, we assume F_0 equals to 1, matching the peak VA of 1 arcminute for a 20/20 observer. During the optimization, the searching ranges for θ_{C1} and θ_{C2} are set to be $[5, 20^\circ]$ and $[20^\circ, 40^\circ]$, respectively, at an increment of one degrees, while the searching range for η was set to be $[0.1, 0.9]$ at an increment of 0.05. These variable configurations and increments yield a total of 5712 sets of parametric combinations and thus 5712 different foveation schemes. For each foveation scheme, the performance metrics defined by Eqs. (8) through (12) are applied. The performance metrics defined in Sec.3.1 depend on the eye gaze direction and full FOV of a target display. The gaze direction was varied from 0 up to 40° at a 5° increment. The full FOV, corresponding to twice of the maximum field angle θ_{max} measured from the display center, was varied from 0° up to 160° at an increment of 2° , or equivalently with the maximum field angle θ_{max} varied from 0 up to 80° at an increment of 1° .

Figure 4(a) plotted 6 different resolution distribution schemes as a function of the field angle θ selected from the 5712 foveation schemes, where η is chosen among 0.3, 0.5, and 0.7, θ_{C1} is fixed at 10° , θ_{C2} is chosen between 20° and 40° , and the maximum field angle is set at 80° . We can observe that the resolution ratio, η , between the fovea and parafovea boundaries and the choice of the θ_{C2} value have significant impacts not only on the rate of resolution degradation across the parafovea region but also on the resulted resolution distribution across the FOV. Consider the curves with the same θ_{C2} value (the lines of the same color), which correspond to the same division between the parafovea and peripheral regions. In this case, a higher η value leads to a slower resolution degradation and overall higher resolution across the FOV than a lower ratio, but potentially yield less data savings. On the other hand, consider the curves with the same η value (the lines of same line style), which correspond to different division between the parafovea and peripheral regions. In this case, a higher θ_{C2} value suggests a larger parafovea region with relative high resolution and a narrower peripheral region. To maintain the same η value, however, a larger θ_{C2} value implies a larger standard deviation σ and slower resolution degradation within the parafovea region and also a higher resolution in the peripheral region, while it may yield less data saving efficiency.

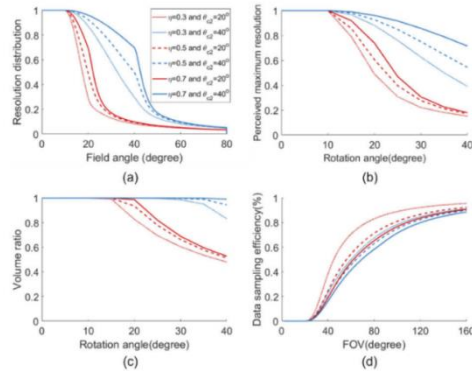


Fig. 4. Comparison of six different foveation schemes with different ratio η and critical balance point θ_{C2} : (a) The resolution distribution as function of field angle; (b) Perceived maximum resolution as function of eye rotation angle; (c) Volume ratio of perceived resolution distribution as function of eye rotation angle; and (d) Relative data sampling efficiency as function of full FOV.

By applying the VA metrics defined in Eqs. (8) through (12), we computed and compared the perceived visual acuity of the six different foveation schemes. Based on Eqs. (9) and (10), Figs. 4(b) and (c) plotted the perceived maximum resolution and volume ratio of the six foveation schemes as a function of eye gaze angle varied from 0 up to 40° at an increment of 5°. The larger values of θ_{C2} and η will lead to higher values of the perceived maximum resolution and volume ratio. For example, for a fixed θ_{C2} value of 40°, the perceived maximum resolution values at 30° eye gaze angle are 0.63, 0.75, and 0.86, for η value of 0.3, 0.5, and 0.7, respectively. The volume ratio remains nearly a constant of 1 for up to 30° eye gaze angle and maintains a ratio above 80% for gaze angles between 30° and 40°. In comparison, for θ_{C2} value of 20°, both the perceived maximum resolution values and volume ratio values are substantially lower than those with a larger θ_{C2} value of 40°. The effect of η value is similar to the effect of θ_{C2} . For example, for the same 30° eye gaze angle and the same θ_{C2} value of 40°, the perceived maximum resolution values are 0.86 and 0.61 for η value of 0.7 and 0.3, respectively.

By applying the metrics defined in Eqs. (11) and (12), we further compared the bandwidth and data sampling efficiency of the six foveation schemes for displays of different full FOVs ranging from 0° up to 160°. Figure 4(d) plotted the sampling efficiency of the six foveation schemes as a function of the total FOV. As expected, when the full FOV is equal to or smaller than the corresponding $2\theta_{C1}$ angle, only the fovea region is utilized and thus no gain in data sampling efficiency over a single-resolution display. When the full FOV is greater than $2\theta_{C1}$, the sampling efficiency increases rapidly as the parafovea region increases and the rate of efficiency improvements reaches its peak when the full FOV is equal to $2\theta_{C2}$. When the full FOV is beyond $2\theta_{C2}$, the sampling efficiency continues to rise but at a reduced rate. In general, a higher η value leads to a lower data sampling efficiency and a slower increase in efficiency improvement rate. With the same η value, a smaller θ_{C2} value yields a higher sampling efficiency. For example, for a display with a 120° FOV and 20° of θ_{C2} , the relative data sampling efficiency is 0.92, 0.87 and 0.84, for a η value of 0.3, 0.5 and 0.7, respectively. For a display with a 120° FOV and η value of 0.5, the relative sampling efficiency is 0.87 and 0.82, for θ_{C2} equal to 20° and 40°, respectively. However, a higher sampling efficiency may be achieved at the cost of perceived

display performance as shown in Figs. 4(b) and (c) and a good balance between these two sets of performance metrics need to be considered.

Choosing an optimal foveation scheme requires considering many factors, such as target display performance requirements, hardware constraints, and application demands. For the purpose of developing a proof-of-concept prototype, we aim to demonstrate the usability of statically-foveated display with a commercially available 4 K monitor. In terms of the threshold performance specifications, the target display shall be able to yield a field angle at least 80° , an angular resolution of 1 arc minute per pixel minimally in the center of the display, and a data sampling efficiency of at least 50%. When the eye is gazed at a 30° angle from the display center, the perceived maximum resolution shall be better than 4 arc minutes and the volume ratio shall be no less than 0.5. Among the 5712 foveation schemes compared, 133 of the schemes satisfied the threshold performance specifications. After further comparison of the 133 schemes, we chose the foveation scheme with $\theta_{C1} = 10^\circ$, $\theta_{C2} = 30^\circ$, and $\eta = 0.3$ for a target display prototype. Based on Eqs. (15) and (16), the standard deviation σ defining the rate of resolution degradation within the parafovea region is $\sigma = 12.89^\circ$, while the threshold gaze angle defining the resolution distribution for the peripheral region is $\phi_{th} = 24.63^\circ$ to make sure the entire function is smooth and continuous without the need for a polynomial correction function $\Delta(\theta)$. The resolution distribution for the selected foveation scheme is expressed as

$$F_{FD}(\theta) = \begin{cases} 1 & |\theta| \leq 10^\circ \\ e^{-\frac{1}{2} \left(\frac{\theta-10}{12.89} \right)^2} & 10^\circ < |\theta| \leq 30^\circ \\ \frac{2.3}{2.3 + (\theta - 24.63)} & |\theta| > 30^\circ \end{cases} \quad (17)$$

5. Performance assessment of the proposed foveated display scheme

Based on the performance metrics described in Section 3, this section will present a thorough assessment of the proposed continuous foveation scheme defined in Eq. (17) and offer a comparison against well-known dual-resolution schemes [8]. As we aim to apply the proposed scheme to the design of a statically foveated display, we therefore assume the end system will not have an optical or mechanical scanning mechanism to dynamically adjust the position of the fovea region relative to eye gaze direction. The fovea region for all the foveation schemes is assumed to be fixed at the display center, regardless of eye gaze.

As discussed in Sec.1, a dual-resolution scheme typically divides the full field into a fovea region with a uniformly high resolution and a peripheral region with a uniform but significantly reduced resolution. To provide meaningful comparison and insightful guidance, we choose two different dual-resolution schemes, one with a narrow $\pm 10^\circ$ fovea region and the other with a wider $\pm 30^\circ$ fovea region. The fovea region of the first dual-resolution scheme offers the same uniformly high resolution of 1 arc minute across the same region as that of the proposed continuous scheme, while the peripheral resolution is set to 0.187 to match the corresponding VA of the HVS at the eccentric angle of 10° . The fovea region of the second dual-resolution offers the same uniformly high resolution of 1 arc minute across $\pm 30^\circ$, as wide as the combined fovea and parafovea regions of the proposed continuous scheme, while the resolution of its peripheral region is set to 0.07 matching with the corresponding VA of the HVS at the eccentric angle of 30° . Figure 5 plots the resolution distribution functions of the three different foveation schemes, the proposed three-segment continuous foveation scheme defined by Eq. (17) (red solid curve with asterisk marks), the 10° dual-resolution scheme (green dashed curve with diamond marks), the 30° dual-resolution scheme (blue dotted curve with pentagram marks), along with the VA curve of HVS for eye gaze angle of 0° (black solid curve) as a reference. We expect the perceived resolution of the 10° dual-resolution scheme will suffer without dynamic foveation while the 30° dual-resolution scheme do not necessarily need dynamic foveation. Furthermore, the optimal perceived resolution of the 10° dual-resolution scheme with dynamic foveation is

expected to match the visual acuity of the HVS within the range of tracked eye movements. Because the $\pm 30^\circ$ is considered as the typical range of eye movements, the perceived resolution of the 30° dual-resolution scheme approximately simulates the anticipated performance of a 10° dynamically foveated dual-resolution system.

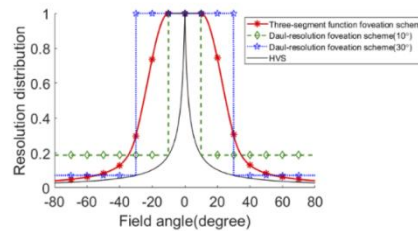


Fig. 5. Resolution distribution for three different foveation schemes: proposed three-segment continuous foveation scheme defined by Eq. (17), a 10° dual-resolution scheme, and a 30° dual-resolution scheme.

5.1. Perceived visual acuity assessment

The perceived resolution of the three different foveation schemes shown in Fig. 5 were analyzed and compared by applying the metrics defined by Eqs. (8) through (10) in Sec. 3.1. Based on Eq. (8), we computed the perceived visual acuity of the three different foveation schemes as a function of field angles for different eye gaze angles, from 0 to 40 at an interval of 5. Figures 6(a) through 6(d) plot the results for 4 different eye gaze angles of 10, 20, 30 and 40, respectively. Due to rotational symmetry, only half of the display FOV from 0 to 80 is plotted. The perceived VA curves of three schemes are plotted by a red solid line, green dash line, and blue dotted line for the continuous, 10° dual-resolution, and 30° dual-resolution schemes, respectively. In each of the sub-figures, we applied different shading schemes to the areas under the perceived VA curves to represent regions where the perceived VA for one or multiple foveation schemes are as high as the relative VA of a 20/20 standard observer at the corresponding eye gaze direction. For instance, the red, green, or blue-shaded areas represent the regions where only the continuous foveation, 10° dual-resolution, or 30° dual-resolution scheme yields a perceived VA as high as a 20/20 standard observer, respectively, the gray-shaded areas represent the regions where the perceived VA of all three schemes are as high as the relative VA of a 20/20 standard observer. The yellow-shaded areas represent the combined regions of the continuous foveation and the 10° dual-resolution schemes which yield as high as the VA of a standard observer, while the magenta-shaded or cyan-shaded areas are for the combined regions of the continuous and 30° dual-resolution schemes or the combined regions of 10° and 30° dual-resolution schemes, respectively. The unshaded area under the HVS curve represents the region where none of the foveation schemes yields image quality as high as the VA of a 20/20 standard observer. The perceived VA values of all three foveation schemes across the entire FOV are nearly as high as the relative VA of a 20/20 standard observer for eye gaze angle less than 10° .

Based on the perceived VA described above, we can observe that the perceived resolution of the continuous foveation scheme can almost match the limiting resolution of the HVS across the entire FOV for eye rotation angles up to $\pm 15^\circ$. As shown by Fig. 6(a), at a 10° eye rotation angle, the perceived VA across the entire field is better or equivalent to the VA of a 20/20 standard observer. At a 15° eye rotation angle, the perceived VA at the fovea center of the eye is about 0.95, which is only slightly below the peak VA value of a 20/20 standard observer. While the 30° dual-resolution scheme yields similar performance, the 10° dual-resolution scheme shows

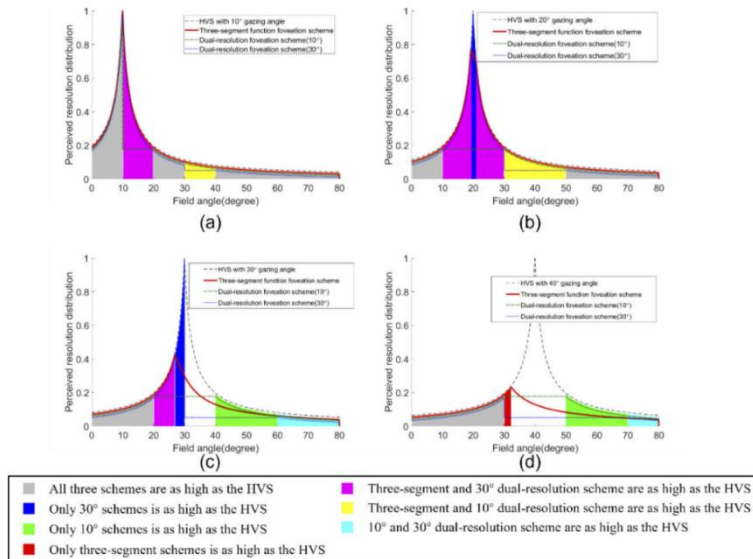


Fig. 6. The perceived visual acuity of three different foveation schemes shown in Fig. 5 as a function of field angles for the eye gaze angle of (a) 10°, (b) 20°, (c) 30°, and (d) 40°, respectively.

significant performance drop for field angles between 10 and 30, for example the magenta-shaded areas in Figs. 6(a) and (b). When the eye rotates within the region of $15^\circ \leq |\phi_G| \leq 30^\circ$, as shown by the examples in Figs. 6(b) and 6(c), the perceived resolution of the continuous foveation scheme degrades gradually as expected for field angles near the fovea center of the eye, with peak values decreasing from about 0.95 to 0.45 for 15° to 30° eye gazing angle, respectively. In comparison, the 30 dual-resolution scheme yields slightly better performance for field angles less than 30, as shown by the blue-shaded areas in Figs. 6(b) and (c), than the continuous foveation scheme, but worse performance for field angles larger than 30 as shown by the yellow-shaded areas of the same figures. The 10 dual-resolution scheme in general yields the worst performance among the three schemes. When the eye rotates toward the peripheral region ($|\phi_G| > 30^\circ$), as shown in Fig. 6(d) for a 40° eye gaze angle, the perceived resolution of the continuous foveation scheme degrades further, but it is better than the performance of the 30° dual resolution scheme within 70° and also generally better than the 10° dual-resolution scheme except for the field angles region beyond 50°. Therefore, we can conclude that the proposed foveation scheme yields no perceivable resolution degradation across the entire FOV when the eye rotates within the $\pm 15^\circ$ region. When the eye rotates within the parafovea region, it is subject to moderate rate of resolution degradation, but still provides good enough perceived quality even with a 30° eye gaze angle where a peak VA value of 0.45 corresponds to 2.2 arcmins/pixel. It overall provides better resolution performance than the two dual-resolution schemes.

Applying Eqs. (9) and (10), we further computed the perceived maximum resolution and volume ratio of the three foveation schemes as a function of eye gaze angles varied from 0 up to 40° at an increment of 5°, and the results are plotted as Figs. 7(a) and 7(b), respectively. When

the eye gaze angle is within $\pm 15^\circ$ from the display center, the maximally perceived resolution of the proposed continuous foveation scheme maintains a peak value of 0.95 or higher, while the 10 dual-resolution scheme drops down to below 0.3 at the eye gaze angle of 15° . When the eye rotates within the region of $15^\circ \leq |\phi_G| \leq 30^\circ$, the maximally perceived resolution of the proposed continuous foveation scheme gradually drops from 0.95 to 0.45, while the 10 dual-resolution scheme remains a low 0.2 beyond the eye gaze angle of 15° . The maximally perceived resolution of the 30° dual-resolution scheme generally remains its peak until the eye gaze reaches a 30° due to its much wider fovea region and then drops sharply beyond the 30° boundary. Furthermore, the volume ratio shown by Fig. 7(b) suggest that 95% or more of the entire display fields performs to the limit of the HVS for eye gaze angle up to $\pm 25^\circ$ for the continuous foveation scheme, which indicates nearly no perceivable degradation within this range of eye motion. In contrast only about 86% and 78% of the fields performs to the limit of the HVS at a 25° eye gaze angle for the 30 and 10 dual-resolution schemes, respectively. Although the perceived maximum resolution of the 30 dual-resolution scheme is generally higher than the continuous scheme for eye gaze angles less than 30, its volume ratio is substantially lower, suggesting more regions of the display fields have lower perceived resolution. Overall, we can conclude that the perceived resolution performance of the continuous foveation scheme, when properly optimized, is adequate without implementing dynamic foveation, and degrades more gracefully than the traditional dual-resolution foveation schemes, especially within the area with most frequent eye movements.

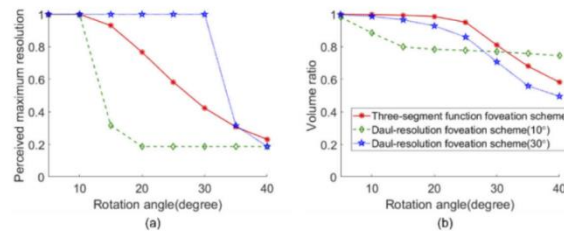


Fig. 7. The comparison of (a) the perceived maximum resolution and (b) volume ratio of the three foveation schemes shown in Fig. 5 as a function of eye gaze angles.

5.2. Data sampling efficiency assessment

By applying Eqs. (11) through (13), the data bandwidth requirement and sampling efficiency for the three foveation schemes shown in Fig. 5 were computed for displays of different full FOVs ranging from 0° up to 160° . Figure 8(a) plotted the relative data sampling efficiency as a function of total FOV. As expected, the sampling efficiency of all three schemes increases as the full FOV increases. The proposed continuous foveation scheme yields a high data saving efficiency of about 81.5% and 92.8% for displays of 100 and 160 FOV, respectively. The amount of redundant raw data produced by a 100° single-resolution display is almost 5 times more than that of the continuous foveation scheme. Considering a display of 100° FOV, the sampling efficiency of the continuous scheme is about 7% lower than the 10° dual-resolution scheme and about 18% higher than the 30° dual-resolution scheme at the same FOVs. As demonstrated in Sec. 5.1, the continuous foveation scheme shows significant advantages in terms of perceived resolution over a 10° dual-resolution scheme.

To further compare foveation schemes in terms of hardware requirement, we computed the total number of required pixels in the diagonal direction of a display as the function of overall diagonal FOV. Four different displays are investigated, three of which are based on the foveation schemes

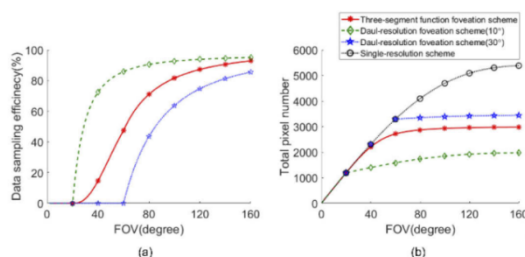


Fig. 8. (a) The comparison of data sampling efficiency as a function of the overall FOV for three different foveation schemes shown in Fig. 5; (b) The comparison of total pixel number required in a diagonal direction as a function of the overall FOV among the three foveation schemes shown in Fig. 5 and (a) single-resolution display.

shown in Fig. 5 and one of which is a single-resolution scheme as a baseline. We further assume the peak resolution of all four display schemes is 1 arc minute per pixel, matching the peak VA of the HVS. It is worth noting that the spatial resolution is defined in angular space rather than based on pixel pitch. Therefore, a uniform angular resolution does not suggest a uniform pixel pitch, but uniform angular sampling of an angular range. When computing the angular resolution of a pixel, two effects should not be neglected especially for large field angles. The first is the projected pixel pitch of a physical pixel on a direction size perpendicular to the corresponding field direction, which is reduced by a factor of $\cos\theta$ and θ is the field angle of the corresponding pixel. The second is the actual distance of a pixel to the viewer, which increases by a factor of $1/\cos\theta$. Combining two factors, the resolution distribution function projected into a uniform pixel-distribution display space needs to multiply a term of square of $\cos\theta$. Figure 8(b) plots the required pixel count in a diagonal direction for the four display schemes. To achieve a 100° FOV in a direction, the continuous foveation scheme requires about 2900 pixels, a commercially available 4 K display is adequate for supporting an FOV over 160° . For the same 100° FOV, 1900 pixels, 3400 pixels, and 6000 pixels are required for the 10° dual-resolution, 30° dual resolution, and single uniform resolution schemes.

6. Experimental validation

6.1. Experimental setup

To experimentally demonstrate and validate the visual effects of a statically foveated display proposed in this paper, we built a test setup with a 27" 4 K monitor with a pixel size of $155.7 \mu\text{m}$ and resolution of 3840 by 2160 pixels. Creating a testbed that can be used to validate the proposed foveation scheme confronts multi-fold challenges and considerations. First of all, to generate ground-truth images for comparison, the display setup should be capable of rendering the original target image for an angular resolution of 0.5 arcminutes per pixel to match the highest VA of the HVS. It shall also cover a large FOV so that the visual effects of peripheral regions can be tested. However, sampling a full FOV of 160° horizontally at an angular resolution of 0.5 arcminutes requires 19200 by 10800 pixels, 25 times more than the pixels available to our 4 K monitor. Secondly, to effectively create an angular resolution of 0.5 arcminutes per pixel, the monitor needs to be placed at a viewing distance of 1070 mm, at which the 27" monitor can only cover an FOV of 31.2° by 17.9° . Mosaicking at least 25 monitors of the same size to cover a full FOV of 160° becomes not only challenging but also subject to alignment errors and artifacts due to monitor bezels. Thirdly, it is further challenging to capture digital images for such wide FOV

and high resolution. To overcome these challenges, we generate high-resolution target images with a horizontal FOV of 80° measured from its top-left corner pixels and with adequate pixels to achieve 0.5 arcminutes per pixel. Effectively, these target images cover a quadrant of a total field up to 160° in the horizontal direction. We then chose to fix the positions of the monitor and the camera to be used for image capture, but virtually pan the rendering viewport of the monitor across the full FOV of the target images as if a virtual pair of monitor and camera was scanned across a large display. More specifically, a 2 K digital camera with a 50-mm focal length lens is centered with the 27" monitor placed at a distance of 1070 mm and the viewing direction of the camera is set to be perpendicular to the monitor surface. The camera offers an angular resolution of about 0.25 arcminutes per pixel. The modulation transfer function (MTF) of the camera was measured with the well-known slanted edge method with Imatest software to ensure the camera yields adequate image contrast and resolution at the Nyquist frequency of 60 cycles/degree of the display.

To render a foveated image, we start with a full-resolution target image and compute a foveated image to be displayed by convolving the original image with the resolution distribution function as a filter. The top-left corner pixel of the target images is assumed to be the center of a foveated display. Because the setup described above is able to yield a peak angular resolution of 0.5 arcminutes per pixel, the resolution distribution function defined by Eq. (17) should be scaled by a factor of 2 expressed as

$$F_{FD}(\theta) = \begin{cases} 2 & |\theta| \leq 10^\circ \\ 2e^{-\frac{1}{2}\left(\frac{\theta-10}{12.89}\right)^2} & 10^\circ < |\theta| \leq 30^\circ \\ \frac{4.6}{2.3+(\theta-24.63)} & |\theta| > 30^\circ \end{cases} \quad (18)$$

A complication for implementing the convolution filter is that the resolution distribution function characterized by Eq. (18) remains constant for the central $\pm 10^\circ$ and then varies with the field angle or pixel location outside the fovea, which requires varying the filter with field angles to realize the different levels of blur matching the resolution distribution function. To account for this effect, the convolution filter is only applied to pixels outside the $\pm 10^\circ$ fields, and the filter applied to the pixels outside the fovea region is implemented by a Gaussian-type filter with a varying standard deviation and a varying convoluted area. The standard deviation of the Gaussian filter at a given field is set to approximate the corresponding angular magnification of the field, which is the ratio of the resolution at the target field angle to the resolution of center field. The convoluted area at a given field is set to be twice as the rounded value of the corresponding angular magnification such that the pixels within the convolution area is sufficient to improve the accurate of blur degree. Figure 9(a) demonstrates four examples of captured zoomed-in images corresponding to the field angles of 10° , 30° , 50° , and 80° with a resolution target, matching with resolution distribution function described by Eq. (18). In this set-up, the pixel pitch of the monitor is $155.7 \mu\text{m}$ or a pixel density of 163 PPI. After applying the convolution filter, the effective pixel density distribution for the foveated display is plotted in Fig. 9(b).

6.2. Objective assessment and validation

To objectively evaluate the image quality rendered by the proposed foveation approach, we generated a 4K-resolution image consisted of a mosaic of 9 by 9 modified Briggs targets. Figure 10(a) shows a captured image of the original 4K-resolution Briggs target pattern displayed on the 4 K monitor by a camera lens of 16 mm focal length. The horizontal and vertical axes were added to the captured image to indicate the field angle on the monitor with the top-left corner pixel as the (0,0) field angle. The resolution target consists of repetitive sub-images of modified Briggs targets periodically arranged in a 9 by 9 regular grid. Each modified Briggs target consists of 16 checkerboards that differ in the number pixels per checker square and the

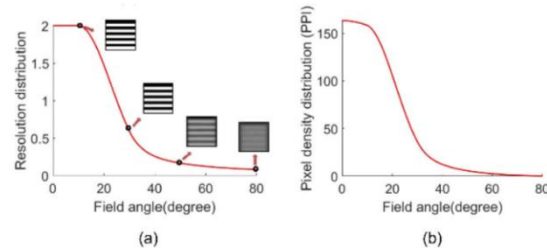


Fig. 9. (a) Examples of four captured zoomed-in images corresponding to 10°, 30°, 50°, and 80° field angles; (b) effective pixel density distribution for the foveated display setup as a function of field angles.

number of checkers. Unlike the original Briggs targets, the light and dark checkers of all the checkerboards have the same contrast of 1. From the smallest to the largest checkers, the number of pixels per square for the first ten checkerboards increases from 1 to 10 pixels at an increment of 1, from 10 to 20 pixels at an increment of 2 pixels for the next five checkerboards, and 25 pixels per checker for the largest checkerboard. The smallest checkerboard, consisting of 5×5 checkers with 1 pixel width per square, is located at the center of each target. Each modified Briggs target is sized to cover an FOV of 8° and 4.5° in the horizontal and vertical directions, respectively. By setting the appropriate spacing between adjacent target sub-images, the centers of the targets along the diagonal direction are precisely located at the positions matching the FOV of a multiple of 10° . In Fig. 10(a), four of the Briggs targets centered at 10° , 30° , 50° , and 80° in the diagonal direction are marked by a red box. Figure 10(b) showed the zoom-in images of these targets captured by a camera lens of 50 mm focal length and the image of the smallest checkerboard with 1-pixel checkers are shown as an inset image on the rightmost side. These captured images demonstrated adequate resolution for the original full-resolution target.

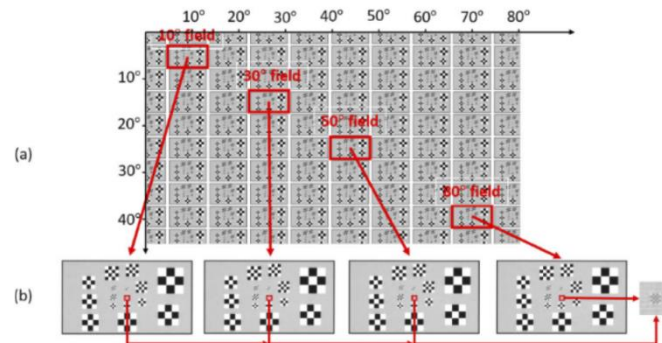


Fig. 10. (a) Captured image of original 4 K Briggs Target pattern by camera; (b) zoomed-in views corresponding the viewing angle of 10, 30, 50, and 80 degrees.

By applying the rendering method described in Sec. 6.1, a foveated image of the Briggs target mosaic shown in Fig. 10(a) is generated and displayed on the 4 K monitor. Figure 11(a) shows the captured foveated image by a 16 mm camera lens for overall effect. Then the zoomed-in images

of the four marked targets centered at the 10° , 30° , 50° , and 80° field angles, respectively, are captured by a 50-mm camera lens with corresponding orientations to emulate the corresponding eye gaze angles, and the results are shown in Fig. 11(b). On each sub-image of Fig. 11(b), we objectively determine the checkerboards as the just distinguishable checkers (JDC) from the captured zoom-in when the contrast of the light-dark checkers falls to approximately 20%. As a result, the just distinguishable checkers corresponding to the 10° , 30° , 50° , and 80° field angles are 1-pixel, 3-pixel, 12-pixel, and 18-pixel checkers, respectively. Magnified views of these JDCs are shown on the right side of each sub-image. As a comparison, using the captured zoom-in images of the same areas with the original full-resolution 4 K images as shown in Fig. 10(b), we simulated the perceived image a 20/20 standard observer with the eye rotated at the angles of 10° , 30° , 30° and 30° , respectively. The perceived images were simulated by convolving the corresponding images in Fig. 10(b) with the filter corresponding to the VA of HVS defined by Eq. (7), by following the same rendering method described in Sec. 6.1. The filter applied to the zoom-in image for the 80° field angle assumes an eye gaze angle of a 30° , rather than 80° , from the 30° field due to frequent and comfortable eye rotation limits. Figure 11(c) shows the simulated perceived images corresponding to the same local areas as those in Fig. 11(b). Similarly, we objectively determined the JDC for each of the targets from the perceived images and the resulted JDC are 1-pixel, 1-pixel, 10-pixel, and 25-pixel checkers for 10° , 30° , 50° , and 80° field angles, respectively. Magnified views of the corresponding JDCs are shown on the right side of each sub-image in Fig. 11(c). By comparing Figs. 11(b) and 11(c), we can conclude that the statically foveated rendering method yields visually comparable image quality to the perceived images rendered from the original full-resolution image, which is a strong evidence that the proposed foveation method may render visually imperceptible quality degradation.

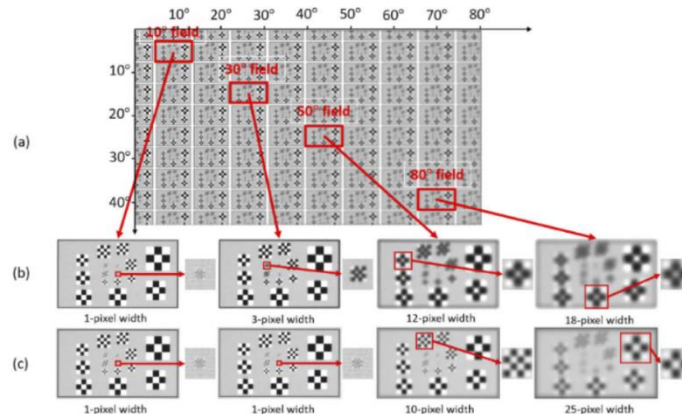


Fig. 11. (a) Captured image of processed Briggs Target pattern by camera; (b) zoomed in views corresponding the viewing angle of 10, 30, 50, and 80 degrees; (c) 4 rendered images of the same local areas perceived by a standard observer with the eye rotated at the angles of 15, 30, 30, and 30 degrees.

Besides objective assessment with a Briggs target mosaic, we repeated the same procedure described above to a 4 K resolution image captured from a real-scene image. The captured foveated image of the entire scene is shown in Fig. 12(a), on which four sub-regions corresponding to 10° , 30° , 50° , and 80° field angles are marked by red boxes. Figures 12(b) and 12(c) shows

the captured zoom-in images of these regions with the original full-resolution image and the rendered foveated image displayed on the monitor, respectively. For the purpose of comparison, Figs. 12(d), (e), and (f) show the perceived images of the four sub-regions of a 20/20 standard observer when the eye is rotated at 0° , 15° and 30° , respectively. These images are simulated from the captured zoom-in full-resolution images shown in Fig. 12(b) by applying the VA filter defined by Eq. (7). It is evident that the statically foveated display in Fig. 12(c) yields visually comparable or better image quality to the perceived images of a full-resolution display for most of the eye gaze angles except that the perceived image of the 50° sub-region for the 30° eye gaze angle appears to be slightly sharper than the captured foveated image of the same region.

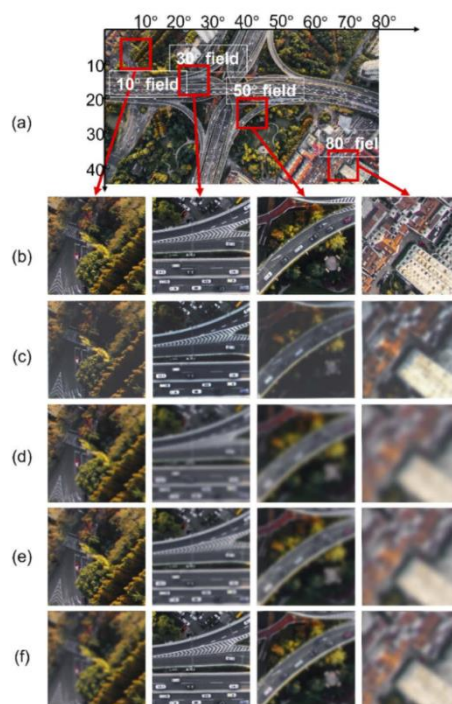


Fig. 12. (a) Captured image of a foveated scene with four marked regions of interests, corresponding to 10° , 30° , 50° , and 80° fields; (b) zoomed-in images of the four marked regions captured with the original full-resolution image displayed on the monitor; (c) zoomed-in images of the four marked regions captured with the statically foveated image displayed on the monitor; (d)-(f) perceived images of the four marked regions by a 20/20 standard observer, simulated from the captured zoom-in full-resolution image for the eye gaze angle of 0° , 15° , and 30° , respectively.

6.3. Quantitative assessment and validation

We further performed experiments to quantitatively evaluate the resulted image quality of the proposed foveation scheme. Two experiments were performed—one to measure the resolution

distribution function of the foveated display to validate the proposed foveation scheme characterized by Eq. (18), the second experiment to measure the perceived display resolution as a function of eye gaze angle. Both experiments utilized two sets of bar targets, one in vertical and one in horizontal directions, respectively. Instead of rendering full-size foveated images, small full-resolution targets covering about 10° field angles were utilized, from which the foveated images corresponding to selected field positions were rendered. Both experiments utilized the same camera with a 50-mm focal length lens to capture the zoomed-in views of foveated targets rendered on the 4 K monitor for various field angles. Examples of captured images corresponding to 10° , 30° , 50° , and 80° field angles were shown in Fig. 9.

To evaluate the resolution distribution of the foveated display, we utilized the standard slanted-edge method to measure the MTFs of a test target. To minimize aliasing effects, we rendered horizontal or vertical bar targets on the monitor, rather than slanted edges, but rotated the monitor to create slanted edge effects. We sampled 22 fields along the diagonal direction of the display, ranging from 5° up to 80° at an increment of 5° within the fovea and peripheral regions and 2° within the parafovea region to account for the different rates of resolution degradation. The foveated images corresponding to the sampled field positions are rendered from the small full-resolution bar targets by applying Gaussian-type convolution filters determined by the angular magnifications corresponding to the field positions.

At each of the sampled field positions, we displayed the corresponding foveated image of a bar target and captured a zoom-in image with the test camera. To measure the inherent resolution distribution of the foveated display, which should be independent of camera viewing angle, we need to ensure that the camera captured the image in a viewing direction perpendicular to the display and centered with the sampled field position. We repeated the process for both horizontal and vertical bars across all of the sampled fields and captured a total of 46 images. The MTFs in horizontal and vertical directions for each of the field positions were analyzed from all the captured slanted edge images. These MTF measurements, which combined the sampling effects of the foveated display scheme and the test camera, need to be corrected by accounting for the MTF of the test camera which was measured with a slanted edge target. Furthermore, the MTF measurements were obtained in terms of the camera sensor sampling frequency. To recover the MTFs of the foveated display, we need to apply a sampling frequency conversion by determining the optical magnification between the camera and monitor pixels and thus converting the sampling frequencies in the sensor space to the angular frequencies in the display space. Figure 13(a) plotted the corrected MTF curves of the foveated display in the horizontal direction corresponding to 13 of the sampled fields. Results for the vertical direction are very similar. As expected, the MTF curves for the 5° and 10° fields remain high, reflecting the native resolution of the fovea region, while the MTF curves outside the fovea region drop as the field angles increase.

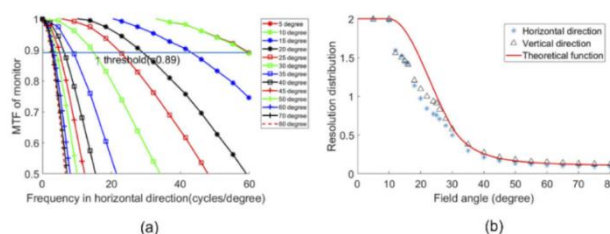


Fig. 13. (a) MTF curves of foveated display in horizontal direction as a function of spatial frequencies in cycles/degree for 13 different field angles; (b) The resolution distribution of the foveated display measured in the horizontal and vertical directions.

To recover the resolution distribution function from the corrected MTF curves, we used the MTF value of 0.89 at 60 cycles/degree, which corresponds to the Nyquist frequency of the monitor, obtained from the 5° zoomed-in view as the threshold value to determine the limiting resolutions for other field angles. The MTF value at 60 cycles/degree for the 5° and 10° fields is the inherent resolution limit of the monitor and the MTF degradation from this threshold value is owing to the foveation scheme. Figure 13(b) plotted the resolution distributions of the foveated display measured in horizontal and vertical directions, marked by * and Δ, respectively, which demonstrate excellent agreement with the theoretical foveation scheme described by Eq. (18).

To quantitatively measure the perceived resolution of the display as a function of eye gaze angle, we adapted the procedure above for the first experiment of measuring the resolution distribution to account for two critical differences. Unlike the first experiment which measures the inherent resolution distribution independent of viewing angles and independent of observer or sensor limit, this experiment aims to measure the perceived resolution distribution as a function of eye gaze angle by a standard observer of 20/20 vision. To account for these differences, the measurement for each sampled field position needs to be repeated at different camera viewing directions with respect to a foveated target image to mimic different gazing directions of a human eye. Furthermore, the captured images need to be convolved with a foveation filter mimicking the relative VA of a 20/20 standard observer characterized by Eq. (7) for MTF analysis to mimic the sampling effects by a human eye. Across the display, we sampled a total of 23 field positions, same as the first experiment. The corresponding foveated images for these fields were rendered in the same way as the last experiment. For each field position, we captured images in 8 different camera viewing angles, from 5° to 40° at a 5° increment. Instead of adjusting camera orientation for each test, which could introduce errors, we adjusted the center positions of the target image on the monitor to yield equivalent viewing angles from the camera's perspective. We repeated the process for both horizontal and vertical bars across all of the sampled fields and viewing directions, yielding a total of 368 images. The process of capture and analysis are repeated as above for each gazing direction. After applying convolution filters to each image to simulate the sampling effects of a standard observer, the same data analysis was applied to these images to obtain the perceived resolution distributions for different viewing angles. Figure 14 plotted the perceived resolution distributions as a function of field angles for 4 different eye gaze angles, 10°, 20°, 30° and 40°, marked by *, Δ, +, and O, respectively. As comparison, the figure also plotted the theoretical resolution distribution of the foveation scheme in red dashed lines and the theoretical perceived resolution distributions obtained by applying Eq. (8) for the four eye gaze angles. The perceived resolution distributions measured experimentally match well with the theoretical results.

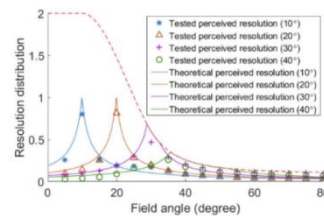


Fig. 14. Quantitative assessment of the perceived resolution distributions as a function of field angles for four different viewing angles, 10°, 20°, 30° and 40°.

7. Conclusion

A foveated display is a promising technique that can potentially address the inherent trade-off between field of view and resolution in conventional displays based on the well-established rectilinear sampling method. Although several prior works have attempted to apply a foveation method to the design of a head-mounted display system, the common method is a dynamic discrete foveation approach where a foveated region offering a high image resolution is dynamically steered in response to a user's gaze direction and a relatively low-resolution region offers peripheral awareness. In this paper, we explored a new perceptual-driven approach to the design of statically foveated HMDs with the goal of offering a wide-FOV across which the degradation of the perceived image resolution may be imperceptible or minimal during the course of eye movement and the perceivable image artifacts and image resolution discontinuity are minimized. In contrast to the multi-level discrete and dynamic foveation approach in the prior art, the static foveation approach will not only maintain resolution continuity, but also eliminate the need for an eyetracker or scanning mechanism and therefore minimize hardware complexity. More specifically, this paper detailed the perceptual-driven approach to optimize the resolution distribution function of a statically foveated display, developed performance metrics to evaluate the perceived image quality and data sampling efficiency, demonstrate the process of applying the performance metrics to obtain optimal foveation schemes to meet the requirements of different applications, experimentally demonstrated and validate the proposed foveation scheme using a bench prototype implemented with a 4 K monitor. In the future work, we will perform perception-based studies to validate the perceived acceptance of this approach and iteratively optimize the foveation scheme for minimal perceptual artifacts. In terms of the implementation of the proposed static foveation approach in an HMD system, it is most desirable to use microdisplay panels offering spatially varying pixel density matching with the resolution distribution of a foveated scheme. Practically, however, due to the easy access to display panels with uniform pixel density, a statically foveated scheme can be achieved by carefully controlling the optical magnification of the viewing optics such that the angular resolution of the virtual image viewed through the optics appear to have a spatially varying resolution distribution that closely matches with a specific foveation scheme. We are in the process of designing and building such an HMD prototype system.

Disclosures. Dr. Hong Hua has a disclosed financial interest in Magic Leap Inc. The terms of this arrangement have been properly disclosed to The University of Arizona and reviewed by the Institutional Review Committee in accordance with its conflict of interest policies.

Data availability. Data underlying the results presented in this paper are not publicly available at this time but may be obtained from the authors upon reasonable request.

References

1. L. C. Loschky and G. W. McConkie, "Investigating spatial vision and dynamic attentional selection using a gaze contingent multiresolutional display," *Q. J. Exp. Psychol. A* **8**(2), 99–117 (2002).
2. W. Zhou and A. C. Bovik, "Embedded foveation image coding," *IEEE Trans. Image Process.* **10**(10), 1397–1410 (2001).
3. A. T. Duchowski and A. Çöltekin, "Foveated gaze-contingent displays for peripheral LOD management, 3D visualization, and stereo imaging," *ACM Trans. Multimedia Comput. Commun. Appl.* **3**(4), 1–18 (2007).
4. B. Bastani, E. Turner, C. Vieri, H. Jiang, B. Funt, and N. Balram, "Foveated pipeline for AR/VR head-mounted displays," *Inf. Disp.* **33**(6), 14–35 (2017).
5. A. Patney, M. Salvi, J. Kim, A. Kaplanyan, C. Wyman, N. Benty, D. Luebke, and A. Lefohn, "Towards foveated rendering for gaze-tracked virtual reality," *ACM Trans. Graph.* **35**(6), 1–12 (2016).
6. G. Sandini, P. Questa, D. Scheffer, B. Diericks, and A. Mannucci, "A retinalike CMOS sensor and its applications," in *Proceedings of IEEE Workshop on Sensor Array and Multichannel Signal Processing (IEEE)*, pp. 514–519 (2000).
7. D. V. Wick, T. Martinez, S. R. Restaino, and B. R. Stone, "Foveated imaging demonstration," *Opt. Express* **10**(1), 60–65 (2002).
8. H. Hua and S. Liu, "Dual-sensor foveated imaging system," *Appl. Opt.* **47**(3), 317–327 (2008).
9. Y. Qin and H. Hua, "Continuously zoom imaging probe for the multi-resolution foveated laparoscope," *Biomed. Opt. Express* **7**(4), 1175–1182 (2016).

10. K. Iwamoto, S. Katsumata, and K. Tanie, "An eye movement tracking type head mounted display for virtual reality system: -evaluation experiments of a prototype system," *Proceedings of 1994 IEEE International Conference on Systems, Man, and Cybernetics. Humans, Information and Technology (Cat. No.94CH3571-5)*, vol. 1, pp.13–18, (1994).
11. J. P. Rolland, A. Yoshida, L. D. Davis, and J. H. Reif, "High resolution inset head-mounted display," *Appl. Opt.* **37**(19), 4183–4193 (1998).
12. G. Tan, Y. H. Lee, T. Zhan, J. Yang, S. Liu, D. Zhao, and S. T. Wu, "Foveated imaging for near-eye displays," *Opt. Express* **26**(19), 25076–25085 (2018).
13. B. Greenberg, "EyeWay Vision: Highly Efficient Immersive AR Glasses Using Gaze-locked Exit Pupil Steering," *SPIE AVR21 Industry Talks II*, Vol. 11764, International Society for Optics and Photonics, (2021).
14. R. Burgess-Limerick, M. Mon-William, and V. L. Coppard, "Visual display height," *Human Factors*, **42**(1), 140–150 (2000).
15. G. Cook and L. Stark, "Derivation of a model for the human eye-positioning mechanism," *The bulletin of mathematical biophysics*, **29**(1), 153–174 (1967).
16. W. S. Geisler and J. S. Perry, "Real-time foveated multiresolution system for low-bandwidth video communication," *Proc. SPIE* **3299**, 294–305 (1998).
17. L. C. Loschky, G. W. McConkie, H. Yang, and M. E. Miller, "The limits of visual resolution in natural scene viewing," *Visual Cognition* **12**(6), 1057–1092 (2005).

APPENDIX B: DESIGN OF A STATICALLY FOVEATED DISPLAY
BASED ON PERCEPTUAL-DRIVEN APPROACH

Pengyinjie Lyu, and Hong Hua

This paper was published in Optics Express, Vol. 31, No. 2, pp. 2088- 2101 (2023)



Design of a statically foveated display based on a perceptual-driven approach

PENGYINJIE LYU AND HONG HUA* 

3D Visualization and Imaging Systems Laboratory, College of Optical Sciences, University of Arizona,
1630 East University Boulevard, Tucson 85721, Arizona, USA
[*hhua@optics.arizona.edu](mailto:hhua@optics.arizona.edu)

Abstract: Foveated display technology has the potential to offer both a large field of view (FOV) and high spatial resolution for head-mounted display (HMD) systems, through allocating the limited resources differently between the region of interest (ROI) and the peripheral region. However, the common method used in the prior studies is based on a dual-resolution dynamic foveation scheme, which is inevitably complex and high cost due to the requirements for multiple display sources, a 2D steering mechanism, and an eye tracking device. We recently proposed a new perceptual-driven approach to design a statically foveated HMD with the goal of offering a wide FOV with nearly imperceptible or minimal degradation of the perceived image resolution within regions where frequent eye movement occurs. Compared to a dynamical dual-resolution foveation approach, it not only minimizes the hardware complexity by eliminating the need for an eyetracker, a scanning mechanism, and multiple display sources, but also offer continuous degradation in resolution to avoid visual artifacts. In this paper, a statically foveated display is designed by carefully controlling the spatial variation of optical magnification of the eyepiece optics, which covers an 80° FOV and achieves a peak resolution of 1.5 arcminutes per pixel. The angular resolution distribution of the prototype design closely matches the theoretical statically foveated scheme described in our previous work with excellent perceived performance. Finally, a foveated display prototype based on the design was experimentally demonstrated with excellent perceived performance matching the designed resolution distribution.

© 2023 Optica Publishing Group under the terms of the [Optica Open Access Publishing Agreement](#)

1. Introduction

The technological development for head-mounted displays (HMD) has been applied to a variety of fields such as medical training, education, and entertainment. Most of the commercially available HMDs, however, only offer a limited angular resolution around 3 arcminutes per pixel, much lower than the 1-arcminute visual acuity (VA) of 20/20 standard observers. One of the main obstacles for achieving high angular resolution in HMD designs is the assumption of the well-established rectilinear sampling method for 2D display and imaging systems in which a finite number of pixels are spread evenly across an entire field of view (FOV), leading to an inherent trade-off between spatial resolution and FOV. For a given number of available pixels, the larger is the FOV, the lower the angular resolution. Consider an HMD design with a typical high-definition (HD) display device of 1920 × 1200 pixels. The angular resolution is about 3.75 arc minutes per pixel for a design spreading the 1920 pixels evenly across an FOV of 120° in the horizontal direction. Based on the same sampling method, achieving an angular resolution of 1 arc minutes per pixel for the same FOV would require a display device of 7200 × 4500 pixels and require a data bandwidth 14 times that of a typical HD device. Although microdisplays with pixel resolution as high as 4 K (3840 × 2160 pixels) are becoming feasible for mass production, they are still not enough to support a large FOV with high uniform resolution. Additionally, such high-resolution displays are not only very challenging to produce, but also computationally challenging to process, transfer, and store such high-resolution images. Besides these technical challenges, the rectilinear sampling scheme is very inefficient. It leads to a large amount of

redundant data for the human visual system to process because the visual acuity of the human eye drops drastically beyond the fovea region on retina. For example, a 4 K microdisplay can cover across only 64° FOV in horizontal direction with a uniform angular resolution of 1 arcminute per pixel. Approximately over 88% of the rendered data cannot be perceived by human visual system (HVS) instantaneously because of rapid degradation of resolution beyond the fovea on the human retina.

Inspired by the foveation properties of HVS, various foveation schemes are explored to mitigate the trade-off between high resolution and large FOV, in which a user's region of interest (ROI) is identified and the limited resources, such as a finite number of pixels or data bandwidth, are allocated differently between the ROI and the peripheral region beyond the ROI. Several dynamically foveated display systems were proposed [1–8], which typically consist of a high-resolution foveated region with a narrow FOV and a low-resolution peripheral region with a relatively wider FOV. An eye tracker or other equivalent devices is typically required to track a viewer's gaze direction and thus determine the instantaneous ROI. The high-resolution foveated region as the ROI is dynamically steered to align itself with a user's gaze direction by a mechanical or optical scanning mechanism [5–8]. Such dynamically foveated displays are inevitably complex, high cost, large volume, and heavy weight because multiple displays and imaging paths are necessary to render multi-level resolution displays, an eye tracking device is required to track ROI, and a 2D steering mechanism, either mechanical or optical, is required for steering the foveated region. Recently, dual-resolution foveated displays were demonstrated with a single display panel by temporal polarization-multiplexing a geometric phase lens which offers two different polarization-dependent optical power [9,10]. Those systems, however, only create two static levels of resolution without dynamic foveation capability. Finally, the multi-resolution approach provides multiple discrete samples of resolution and thus discontinuous perception of image quality as eye moves, leading to potential visual artifacts.

To overcome those drawbacks of the dynamically foveated method for HMDs, we recently proposed a new perceptual-driven static foveation approach to HMD designs [11]. Motivated by the fact that an HMD is generally attached to a user's head with a relatively fixed viewing position, the characteristics of eye and head motions and the perceived visual effects are explored in the process of design a static foveation display which offers a spatially varying angular resolution distribution through a single display path without requiring a gaze tracker and a 2D steering mechanism. By utilizing microdisplays with a limited pixel resolution such as commonly available 2 K pixels, a statically foveated display aims to offer a wide FOV across which the perceived image resolution appears high with imperceptible or minimal degradation and resolution discontinuity during eye movements. Compared to the multi-level discrete and dynamic foveation approach in the prior art, the static foveation approach will not only maintain resolution continuity, but also eliminate the need for an eyetracker or scanning mechanism and therefore minimize hardware complexity. Section 2 will provide an overview of the perceptual-driven approach.

In this paper, based on the perceptual-driven approach detailed in [11], we designed and experimental demonstrated a statically foveated display by combining a custom-made eyepiece with a spatially varying optical power and a commodity microdisplay with a uniform pixel density. Section 2 reviews the perceptual-driven approach; Section 3 presents the optical specifications of the statically foveated display, methods of designing the eyepiece with spatially varying optical power, and the optical performance analysis, and finally Section 4 experimentally validates the performance of the statically foveated display prototype.

2. Perceptual-driven approach to statically foveated HMDs

Figure 1 (a) shows a schematic illustration of a statically foveated display where the display plane is the conjugate virtual image of a display source seen by a viewer through the optics in an HMD system and the optics is omitted for simplicity [11]. Figure 1(b) plots an example of the resolution

the regions, σ is the standard deviation of a Gaussian function, affecting the rate of resolution degradation within the parafovea region, and ϕ_{th} is a threshold eye gaze angle that determines the eccentricity of a field angle in the peripheral region and the rate of resolution degradation. $\Delta(\theta)$ is a polynomial correction function to make the third and the second segments of the resolution distribution function continuous at the θ_{C2} , where the specific order of the $\Delta(\theta)$ is determined by the value of σ , θ_{C1} , and θ_{C2} .

The parameters for the resolution distribution functions in Eq. (1) may be carefully optimized for minimally perceivable quality degradation or more data saving or ease of implementation. A set of performance metrics for perceived image quality and data sampling efficiency were detailed in our prior work by fully accounting for the characteristics of eye movement and head motion, target display specifications, and perceived performance as a function of eye motion and field angle [8]. For instance, the metrics for perceived image quality include the perceived visual acuity, the perceived maximum resolution, and volume ratio. The perceived visual acuity of a foveated display, VA_{FD} , is used to quantify the perceived performance as the function of the field angle and eye gaze direction, the perceived maximum resolution is to characterize the peak resolution across the overall FOV at different gaze directions, and the volume ratio is a summative metric to evaluate the proportion of perceived resolution of a display below the perceptible limit of the HVS and it is calculated by the ratio of the integral volume enclosed by the perceived resolution curve of a display to the volume enclosed by the VA curve of the HVS across the display's FOV for different eye gaze directions. The metrics for data sampling efficiency include the total raw data bandwidth, relative data sampling efficiency, and effective information throughput. The total raw data bandwidth is obtained by integrating its resolution distribution across all fields, the relative data sampling efficiency compares the sampling efficiency against a single-resolution uniformly sampled display which offers the same resolution across its entire FOV as the peak resolution of a foveated system, and the relative information throughput calculates the data bandwidth ratio between the HVS and a display scheme.

Based on those metrics, the resolution distribution example in Fig. 1(b) is expressed as:

$$F_{FD}(\theta) = \begin{cases} F_{peak} & |\theta| \leq 10^\circ \\ F_{peak} \times e^{-\frac{1}{2} \left(\frac{\theta-10}{12.89} \right)^2} & 10^\circ < |\theta| \leq 30^\circ \\ F_{peak} \times \frac{2.3}{2.3 + (\theta - 24.63)} & |\theta| > 30^\circ \end{cases}, \quad (2)$$

where F_{peak} is the peak resolution value of the foveated display. The two critical balance field angles are 10° and 30° , respectively. The foveation scheme in Eq. (2) was optimized for a foveated display offering a field angle of at least 80° and data sampling efficiency of at least 50%. The detailed optimization process has been described in our previous work [10]. By setting the peak angular resolution to be 1 arcminute per pixel, Figs. 2(a) and 2(b) plotted the perceived maximum resolution and volume ratio of the foveation scheme as a function of eye rotation angles varied from 0 up to 40° at an interval of 5° . The perceived maximum resolution is larger than 45% of peak resolution within the parafovea region. The volume ratio in Fig. 2(b) suggests that 95% or more of the entire display fields performs to the limit of the HVS for eye gaze angle up to $\pm 25^\circ$, which indicates nearly no perceivable degradation within this range of eye motion. Figures 2(c) and (d) plotted the relative data sampling efficiency and the total number of required pixels in the diagonal direction as a function of the overall FOV, respectively. The foveation scheme offers a high data sampling efficiency of 92.8% for displays of 160° FOV, and such a statically foveated scheme can be adequately implemented with a 4 K display covering over 160° full FOV.

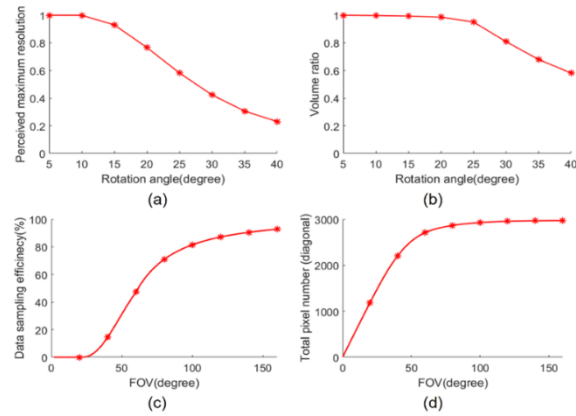


Fig. 2. (a) the perceived maximum resolution and (b) volume ratio of the foveation scheme as a function of eye rotation angles; (c) the data sampling efficiency as a function of the overall FOV for the foveation scheme; (d) the total pixel number required in a diagonal direction as a function of the overall FOV.

3. Optical design of a statically foveated HMD system

To design a statically foveated HMD system offering spatially varying angular resolution distribution, a straight-forward method is to utilize a display offering spatially varying pixel density that matches with the angular resolution distribution of a foveated scheme. Practically, however, it is challenging to manufacture displays with spatially varying pixel density. Instead, a statically foveated display can be realized by adopting display panels with uniform pixel density and carefully designing an eyepiece offering spatially varying optical power such that the angular resolution distribution of the virtual display seen through the eyepiece corresponds to a desired foveated scheme. The spatially varying optical power of an eyepiece, Φ_{EP} (i.e., the reciprocal of the eyepiece focal length f_{EP}), can be calculated from the resolution distribution function as

$$\Phi_{EP}(\theta_x, \theta_y) = \frac{1}{f_{EP}(\theta_x, \theta_y)} = \frac{\tan\left(\frac{1}{60 \cdot F_{FD}(\theta_x, \theta_y)}\right)}{p_0 \cos^2 \theta}, \quad (3)$$

where the p_0 is the pixel pitch of a uniform-resolution display.

We custom-designed an immersive HMD prototype to validate the above approach. The system mainly consists of a custom eyepiece design with spatially varying optical power and a commercially available microdisplay. The specification of the system is summarized in Table 1. One of the key parameters to determine in the design process is to choose a display panel with adequate pixels for a wide-FOV foveated system. The choice for a display panel is limited by availability and cost. In general, displays with total pixel counts lower than 3000 in its longer side are preferred for data efficiency. Based on the resolution distribution functions in Eq. (2), Fig. 3 shows the number of required pixels as a function of the FOV in a radial direction for three different peak resolutions of 1, 1.5, and 2 arcminutes per pixel, respectively. The results suggest that a commonly available full HD display can potentially realize a foveated display with a FOV of over 200° with a peak angular resolution of 2 arcminutes per pixel, a 2 K (QHD) display can potentially realize a FOV of over 200° with a peak angular resolution of 1.5 arcminutes per pixel, and a minimum of 3260 pixels is required to support a 100° FOV with a peak resolution of 1

arcminute per pixel. Based on these considerations, a smartphone (Sony Xperia XZ2 Premium) was chosen as the display panel because of its small pixel pitch and enough pixel number. Though the display panel with a diagonal size of 147 mm and a total of 3840×2160 pixels, the active display area being used is about 60 mm horizontally and 60 mm vertically, with 1820 by 1820 pixels, respectively, due to the limit of the interpupillary distance of human eyes. It allows to support a foveated display with a diagonal FOV of 80° and peak angular resolution of 1.5 arcminutes per pixel.

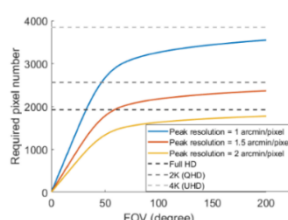


Fig. 3. The required pixel number of a foveated display as a function of the overall FOV in a given direction for three different peak resolution of 1, 1.5, and 2 arcminutes per pixel, respectively.

Table 1. The specification of the foveated display.

	Parameters	Specifications
Display	Active panel size	< 3.33 in. diagonally (60 mm horizontally and 60 mm vertically)
	Active pixel resolution	1820×1820 pixels
	Pixel pitch	0.033 mm
Optical system	Exit pupil diameter	8 mm
	Eye relief	≥ 18 mm
	Number of elements	≤ 5
	Wavelength	480-625 nm
	FOV	80° diagonally, $\sim 56.5^\circ$ (H) * $\sim 56.5^\circ$ (V)
	Vignetting	< 0.3 for the edge fields ($\pm 40^\circ$)
	Image quality	MTF $> 10\%$ at 15 cycle/mm

In terms of the optical specifications, the exit pupil diameter of the eyepiece is set as 8 mm, considering the limited eye movement range for the 2~4 mm eye pupil size; the eye relief is set to be at least 18 mm allowing the standard eyeglass wearing, and diagonal FOV target is set to be 80° . We further limit the total number of optical elements of the eyepiece to no more than 5, most of which are preferred to be stock lenses to limit fabrication cost. We anticipate at least one of the elements is an aspherical lens varying optical power as a function of fields.

The optical design was carried out with CODE V® software. We started an eyepiece design with all spherical lenses and an initial design was found with three spherical lenses based on the first order calculation to ensure an angular resolution of 1.5 arcminutes per pixel near the center region of the fields. Then an aspherical lens was inserted close to the display panel as a field lens to provide spatially varying optical power control. The reason why the aspherical lens was inserted between the display and original lens group is because the interaction of the ray bundles from adjacent fields was minimal and the optical power and aberration control were more effective.

During the design process, one of the challenges was to establish proper relationships and constraints between field-dependent optical power, target angular resolution distribution, and ray tracing data output by optical design software. To calculate the resolution distribution in optical design software, we traced the chief ray heights intersected at the display panel for different field angles. When the field sampling is sufficiently dense to ensure the difference between two adjacent fields is small enough, the resolution distribution at a field angle of θ can be characterized as:

$$F(\theta) = \frac{h_c(\theta + \Delta\theta) - h_c(\theta)}{p_0 \times \Delta\theta} \quad (4)$$

where the $h_c(\theta)$ is the chief ray height at the display panel for θ° field, and $\Delta\theta$ is sampling interval of field angle. $\Delta\theta$ was set to 0.1% of the full FOV, so one million rays were traced to cover the overall 2D field map. By plugging the Eq. (4) into Eq. (3), the field-dependent optical power of the eyepiece can be obtained and controlled.

In the design software, the ray-tracing data obtained through Eq. (4) were used to create user-defined constraints for lens optimization. It is unrealistic to constrain the optical power distribution with large samples. Instead, the optimization was performed by progression. The optimization started with the optical power constraints at two critical field angles, 10 and 30 degrees. These two constraints were controlled loosely at first when low-order polynomials were used to define the aspheric surfaces. As the high-order parameters of the aspherical surfaces were introduced up to 8th order, those two constraints were gradually tightened up to match their target values. Several weak constraints of the optical power were added at other intermediate fields, such as 18 degrees, 26 degrees or others, which corresponded to fields with relatively large slope changes in the resolution distribution curve. The regions of these weak constraints and the specific field angles were determined by the current resolution distribution curve of the optics obtained using Eq. (4) during the optimization.

Another major challenge is to achieve a large range of optical power variation through a single eyepiece and rigorously match the angular resolution distribution in Eq. (2) which suggests a very large optical power difference between the center and edge fields. For example, for a statically foveated display with 40° half FOV, Eq. (2) suggests an optical power ratio between the center and edge fields of over 7.5 times. However, with only one aspherical field lens, it is only feasible for an optical power ratio of about 3 times to ensure the high perceived performance within fovea and parafovea regions. Correspondingly, additional pixels on the display panel are needed to relax the requirement for optical power range while maintaining the same FOV and peak angular resolution of 1.5 arc minutes per pixel. Although the utilization of additional display panel region leads to a slight reduction of the data sampling efficiency, the perceived performance within the parafovea and peripheral regions is expected to improve.

After reaching good performance, we replaced the customized spherical lenses with the three stock lenses. The 2D layout of the final eyepiece design is shown in Fig. 4. Limited by the clear aperture of the stock doublet (the third lens from the left), 30% vignetting for edge field was introduced.

The image performance of conventional HMD designs based on rectilinear sampling method is commonly evaluated by examining the modulation transfer functions (MTF) in the microdisplay space across the FOV for spatial frequencies up to Nyquist frequency set by the display pixel pitch. Due to the nature of spatially varying optical power of the eyepiece in the foveated eyepiece design, it is no longer valid to adopt this common practice. Instead, to analyze the perceived performance of the foveated eyepiece design in the visual space, we flipped over the optical system in Fig. 4, traced rays from display toward the exit pupil and inserted the Arizona eye model at the exit pupil. The reversed layout is illustrated in Fig. 5, where the display panel is set to be the object with uniform spatial sampling and the retina of the eye model is treated as the image plane. The entrance pupil of the eye model, 3.05 mm away from cornea, is located at the

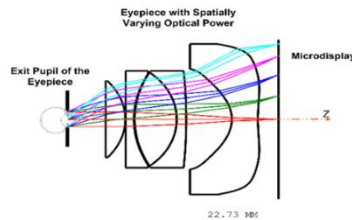


Fig. 4. The layout of eyepiece for the statically foveated display.

exit pupil position of the foveated eyepiece. To simulate the effects of eye movement, the Arizona eye model is set to rotate around its rotation center, which is 13 mm behind the corneal vertex. Figures 5(a) and 5(b) show two examples of the system setup corresponding to the eye model rotated by 0° and 30° , respectively. For each eye-rotation position, the vignetting factors for all fields need to be reset to aim the chief ray centered at the stop and the rays fully fill the aperture.

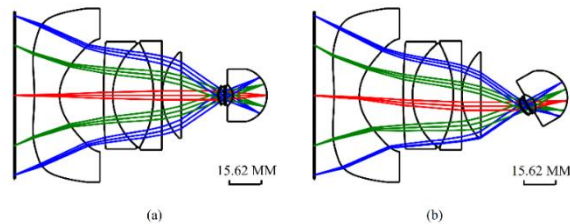


Fig. 5. The layout of the reserved system with Arizona eye model: (a) eye gaze at 0° ; and (b) eye gaze at 30° .

The perceived performance of the static foveated display was evaluated when the Arizona eye model was rotated from 0° to 30° with a 5° interval. To compare with HVS, the spatial frequency was converted into cycle per degree measured in the visual space, and the field type was converted from the object height at the display panel to the field angle incident upon the eye pupil based on the real ray trace data. The designed peak angular resolution was 1.5 arcminutes per pixel, corresponds to an effective pixel size of $7.2 \mu\text{m}$ on the human retina, which sets the MTF cut-off frequency as 20 cycles per degree in the visual space or equivalently about 69.5 cycles per millimeter on the retina. Figures 6(a) through 6(d) plot the MTF curves for selected fields with the Arizona eye model rotated at 0° , 10° , 20° , and 30° , respectively. On each of the plots, five fields, 0° , $\pm 20^\circ$, and $\pm 35^\circ$, across the FOV of the display were sampled and these fields represent the central zones of the fovea, parafovea, and peripheral regions, respectively. With the eye gaze of 0° , the MTF values for both the fovea and parafovea regions are above 20% for frequencies up to 20 cycles per degree. It is worth noting that the negative angles are moving toward the line of sight (LoS) while the positive fields are away from the LoS as the eye gaze angle increases. For instance, with an eye gaze angle of 20° , the -20° field is centered with the fovea of the HVS while the $+20^\circ$ field is 40° away from the fovea. As shown in Figs. 6(b) and 6(c), with an eye gaze angle up to 20° , the MTF values of the negative field angles shown in dashed lines are approximately the same as those of the 0° field. Even with a 30° eye movement (Fig. 6(d)), the MTF values for the negative fields are above 20% for frequencies up to 15 cycles

per degree. These observations suggest that the foveated display can yield high image contrast for eye movements as high as 30° . Though the MTF values of the positive field angles shown in solid lines are noticeably lower than the 0° field, these fields fall within the peripheral region of the HVS.

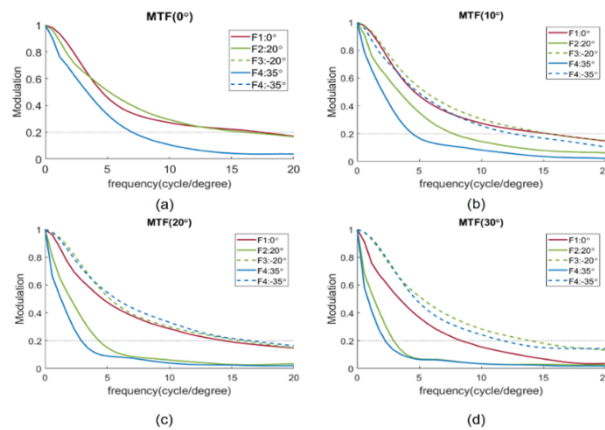


Fig. 6. MTF plots for various fields with the rotation angle of Arizona eye model part: (a) 0° ; (b) 10° ; (c) 20° ; (d) 30° .

To determine the perceived limiting resolution distribution of the foveated display at different eye rotation angles, the average MTF values in the tangential and radial directions were computed as a function of angular frequencies for each of sampled field angles across the display. At a given eye rotation angle, the perceived limiting resolution for a given field angle of the foveated display was then obtained from its corresponding MTF curve by locating the maximum angular frequency at which the MTF value is equal to a contrast modulation threshold of 20%. The choice of modulation threshold is based on the contrast sensitivity function of the HVS adequate for detecting fine details with cut-off frequencies as high as 20 cycles per degree. Figures 7(a) through 7(d) graphed the perceived limiting resolution distributions of the foveated display as a function of the display field angle with 0° , 10° , 20° , and 30° eye rotation angles, respectively. On each graph, the visual acuity of a 20/20 standard observer was overlaid for reference and the peak of the VA curve is aligned with the corresponding gaze direction. As shown in Figs. 7(a) through 7(c), for eye movements no more than 20° , the perceived peak resolution of the foveated display is about 60% of the peak VA of a standard observer, corresponding to an angular resolution of about 1.5 arcminutes per pixel which is in agreement with the target resolution of the fovea region. The perceived limiting resolution of the foveated display exceeds the VA of a standard observer across the entire FOV except for a small area around the gaze direction. As shown in Fig. 7(d), when the eye is gazed at around 30° , the peak resolution of foveated display is reduced to around 40% of the peak resolution of a standard observer, and its location is deviated by around 10° from the gaze direction. However, the perceived limiting resolution of the foveated display still exceeds the VA of a standard observer within the field region from -25° to 40° . Overall, we can conclude that the perceived performance of the static foveated display is adequate without the equipment of dynamic tracking and scanning device, especially within the $\pm 20^\circ$ region where frequency eye movements occur.

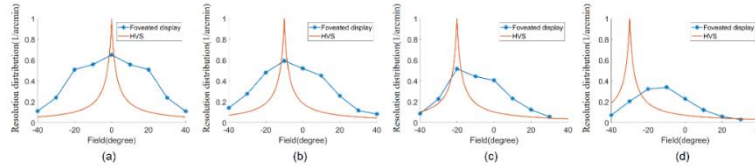


Fig. 7. The resolution distributions of the foveated display as the function of the field angle with the eye rotation angle of (a) 0°; (b) 10°; (c) 20°; (d) 30°, respectively.

Figure 8 (a) illustrates the distortion grid of the foveated display at display plane. Figure 8 (b) plots the resolution distribution map across the virtual display plane. The map was obtained by tracing the chief ray heights for each sampled field angle and computing the corresponding resolution distribution using Eq. (4). The optical system was sampled with an 0.8-degree interval across 80-degree square FOV. Figure 8 (c) further demonstrates the resolution distribution as the function of the field angle along the diagonal direction and the target resolution distribution is plotted in dash line for comparison. The rate of resolution degradation reached our design target. It remains nearly constant within foveated region and drops from slow to fast speed as the field angle increases. Figure 8 (d) plots the pixel number in diagonal direction as a function of the FOV for designed foveated display, which is derived from the resolution distribution function curve. For 80-degree FOV in diagonal direction, the total required pixel number is approximately

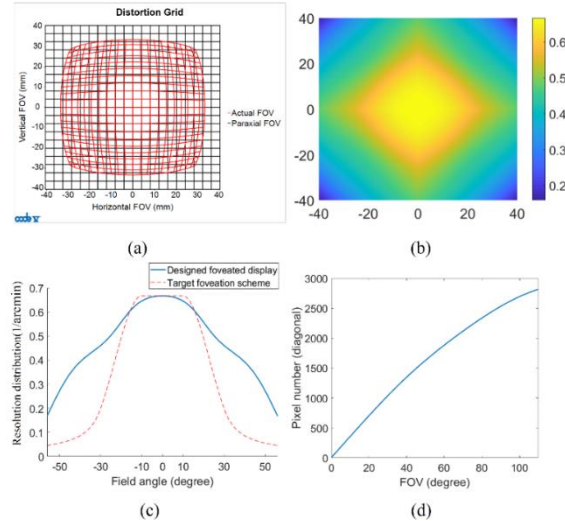


Fig. 8. (a) The distortion grid of designed foveated display; (b) The resolution distribution in field map; (c) the resolution distribution of designed foveated display and a target foveation scheme as the function of the field along the diagonal direction; (d) the pixel number in diagonal direction as a function of the FOV for designed foveated display.

2340, which significantly reduces the requirement of display panel compared to a rectilinear sampling display.

4. Prototype and experimental results

To experimentally validate the performance of the static foveated display, we fabricated the custom aspherical lens in Fig. 4 and built a testing prototype with a photograph shown in Fig. 9(a). In this setup, a 2 K camera was placed at the anticipated viewing position to mimic the human eye and capture images through optics, and the Sony cellphone was utilized as the display panel, where captured images generate an 80-degree circular FOV.

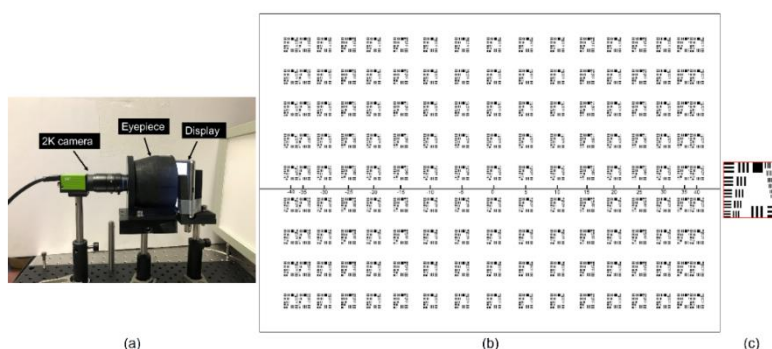


Fig. 9. (a) Prototype of the static foveated display with cellphone display panel; (b) The input image displayed on the cellphone screen; (c) Zoomed sub-image for the modified USAF target.

We generate a 4K-resolution image composed of 17 by 9 modified USAF 1951 targets, as illustrated in Fig. 9 (b). Each sub-image consists of the elements from Groups 2 and 3, as shown in Fig. 9 (c). The line width of Group 2 Element 1 was set as $125\ \mu\text{m}$ and the line width of the Group 3 Element 6 is 1 pixel. Each sub-image covers 2.5° by 2.5° FOV and is aligned with the intervals of 5 degrees in horizontal and vertical directions. The placements of these sub-images with respect to the display FOV in the horizontal direction are marked by the axis in Fig. 9(b). Because the optical power of the eyepiece varies with field angles, the sub-images on the display panel were arranged with non-uniform displacements based on the ray trace data from the eyepiece design. The 4 K image covers a total FOV of 80° by 40° in horizontal and vertical directions, respectively. Figure 10 (a) shows an image captured by the 2 K camera with an 8-mm focal length lens. Considering the non-uniform arrangement of the sub-images, the spatially varying optical magnification of the eyepiece is clearly observed. To demonstrate the optical performance of different field positions, the 8-mm camera lens was replaced with a 50-mm lens. Figures 10(b) through 10(d) show the captured images when the camera was adjusted to point towards 0° , -20° , and -35° of the display fields, respectively in the horizontal direction. As demonstrated by Figs. 10(b) and 10(c), the display yields excellent optical performance within the region of $\pm 15^\circ$, in which frequent eye movements are likely to occur. It is worth noting that the Sony cellphone display was unable to show a native 4 K resolution image. With Android Debug Bridge method, the display was forced to emulate 4 K resolution, but it would scale a 4 K image down to 1080p before enlarging to 4 K, which causes extra blur or misalignment.

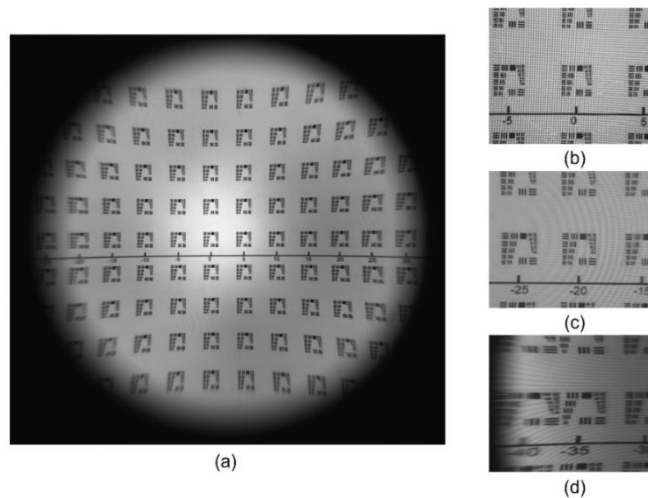


Fig. 10. (a) Captured image by 2 K camera with 8-mm focal length camera lens; Captured image by 2 K camera with 50-mm focal length camera lens when the camera was towards (b) 0°, (c) -20°, and (d) -35° of the field angle of display, respectively.

To accurately quantify the performance of the optics, we measured the system MTF curves with the slanted edge method using Imatest® software. Instead of displaying a target with the Sony display panel, a large bar on a transparent high-resolution target (USAF 1951 Target) illuminated by a LED backlight was used as the slanted edge target to avoid pixilation effects of the display panel, shown in Fig. 11(a). Figure 11(b) shows an example of a captured image where the slanted edge target is aligned with the center of the eyepiece FOV, where the zoomed-in image surrounded by the red rectangle is the slanted edge used to measure the MTF. For this part of testing, a 2 K camera with a 25-mm focal length lens was used to offer 0.69 arcminutes per pixel in angular resolution which is over twice as high as the peak resolution provided by the foveated display to ensure the camera yields adequate image contrast and resolution at Nyquist frequency of 20 cycles/degree of the display. During the test, the camera was rotated horizontally to mimic the eye movement, and the target was moved along the horizontal direction with the same height to ensure the measured edge is always located at the same position in camera's view. Both camera direction and resolution target position were aligned with a printed transparent field coordinate reference label, which is placed in front of the high-resolution target, as shown in Fig. 11(b).

Nine fields were captured in the image space from 0° to 40° with the interval of 5°. Because the MTF results measured with the Imatest® software were based on the sampling frequency of the camera sensor, we needed to convert the sampling frequencies from the camera sensor space to angular frequencies in the display space by applying the factor of the optical magnification between the pixel sizes of camera sensor and designed display. Figure 12(a) shows the MTF plots as the function of the converted frequency in display space. These MTF results match well with the simulated MTF of the eyepiece design in CODEV, and as expected, the MTF curves drop as the field angle increases.

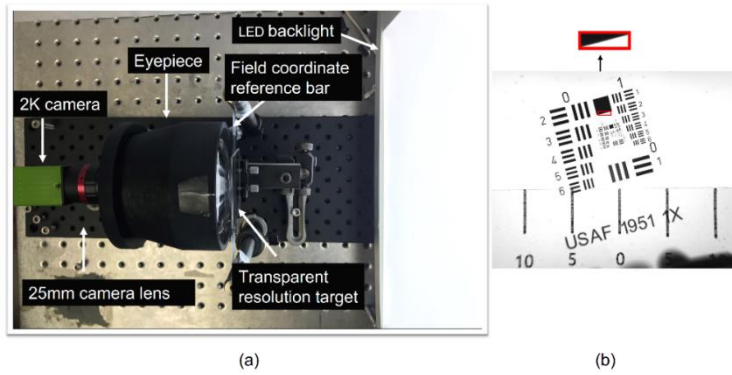


Fig. 11. (a) Prototype of the static foveated display with transparent high-resolution target; (b) The captured image of high-resolution target for straight view direction.

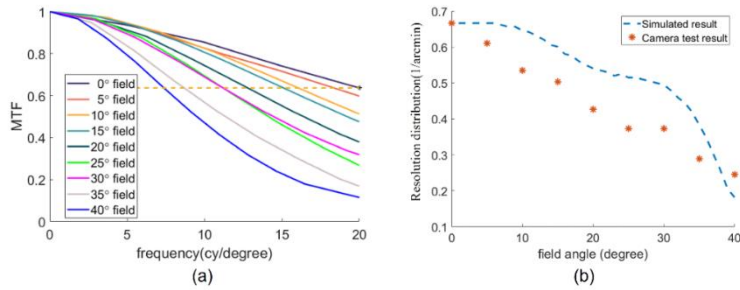


Fig. 12. (a) MTF curves of foveated display in horizontal direction as a function of spatial frequencies in cycles/degree for 9 different field angles; (b) The resolution distribution of the foveated display measured in the horizontal direction.

To build the resolution distribution based on the MTF curves in Fig. 12(a), we used the MTF value of 0.64 at 20 cycles/degree obtained from the 0° MTF plot as a threshold value to obtain the limiting resolutions for other 8 MTF plots with non-zero field angles. This threshold represents the combined modulation of the resolution target due to eyepiece and camera sampling effects at the Nyquist frequency, and it is the inherent resolution limit of the testing system. Figure 12 (b) shows the graph of the limiting resolution distribution function as a function of field angles, which resembles the simulated distribution obtained in CODEV.

5. Conclusion

Although a dynamic foveated display design for HMDs is potentially optimal to address the inherent trade-off between FOV and resolution in the rectilinear sampling displays, its structure is complicated due to the requirements for multiple display paths, an eyetracker, and a scanning mechanism. In this paper, based on our previous work of a new perceptual-driven approach to the design of statically foveated HMDs, we presented a prototype design and prototype demonstration by carefully controlling the optical magnification of the optics to achieve a spatially varying resolution distribution closely matching a target foveation scheme. The designed statically foveated display not only eliminates the requirements for eye-tracking device and scanning mechanism, but also provides nearly imperceptible resolution degradation. The prototype system achieved a foveate display with an 80-degree FOV and an angular resolution of 1.5 arcminutes per pixel in the foveated region, using three stock lenses and a custom aspherical lens. Both the simulated results and the experimental tests validated outstanding image quality within the region in which the eye frequently moves.

Disclosures. Dr. Hong Hua has a disclosed financial interest in Magic Leap Inc. The terms of this arrangement have been properly disclosed to The University of Arizona and reviewed by the Institutional Review Committee in accordance with its conflict of interest policies.

Data availability. Data underlying the results presented in this paper are not publicly available at this time but may be obtained from the authors upon reasonable request.

References

1. J. Spjut and B. Boudaoud, "Foveated displays: Toward classification of the emerging field," In ACM SIGGRAPH 2019 Talks (pp. 1–2), (2019).
2. G. Sandini, P. Questa, D. Scheffer, B. Diericks, and A. Mannucci, "A retinalike CMOS sensor and its applications," in *Proceedings of IEEE Workshop on Sensor Array and Multichannel Signal Processing (IEEE)*, 514–519 (2000).
3. D. V. Wick, T. Martinez, S. R. Restaino, and B. R. Stone, "Foveated imaging demonstration," *Opt. Express* **10**(1), 60–65 (2002).
4. H. Hua and S. Liu, "Dual-sensor foveated imaging system," *Appl. Opt.* **47**(3), 1 (2007).
5. Y. Qin and H. Hua, "Continuously zoom imaging probe for the multi-resolution foveated laparoscope," *Biomed. Opt. Express* **7**(4), 1175–1182 (2016).
6. K. Iwamoto, S. Katsumata, and K. Tanie, "An eye movement tracking type head mounted display for virtual reality system: -evaluation experiments of a prototype system," *Proceedings of 1994 IEEE International Conference on Systems, Man, and Cybernetics*. Humans, Information and Technology (Cat. No.94CH3571-5). vol. 1, pp.13–18 (1994).
7. J. P. Rolland, A. Yoshida, L. D. Davis, and J. H. Reif, "High resolution inset head-mounted display," *Appl. Opt.* **37**(19), 4183–4193 (1998).
8. G. Tan, Y. H. Lee, T. Zhan, J. Yang, S. Liu, D. Zhao, and S. T. Wu, "Foveated imaging for near-eye displays," *Opt. Express* **26**(19), 25076–25085 (2018).
9. C. Yoo, J. Xiong, S. Moon, D. Yoo, C. K. Lee, S. T. Wu, and B. Lee, "Foveated display system based on a doublet geometric phase lens," *Opt. Express* **28**(16), 23690–23702 (2020).
10. K. Yin, Z. He, Y. Li, and S. T. Wu, "Foveated imaging by polarization multiplexing for compact near-eye displays," *J. Soc. Inf. Disp.* **30**(5), 381–386 (2022).
11. P. Lyu and H. Hua, "Perceptual-driven approach to statically foveated head-mounted displays," *Opt. Express* **29**(21), 33890–33914 (2021).
12. R. Burgess-Limerick, M. Mon-William, and V. L. Coppard, "Visual display height," *Human Factors* **42**(1), 140 (2000).
13. G. Cook and L. Stark, "Derivation of a model for the human eye-positioning mechanism," *Bull. Math. Biophys.* **29**(1), 153 (1967).

APPENDIX C: MATLAB© CODE FOR GENERATING THE FOVEATED
IMAGE BY GAUSSIAN-TYPE FILTER

```

% Generating the foveated image by gaussian-type filter
clear all; % Clear all variables
close all; % Close all open figures
clc;      % Clear command window
% Read image named 'xxxx.bmp or other type of picture'
I = im2double(imread('Original image.bmp'));
%Number of pixels for vertical and horizontal directions and number of color channel
[Ny,Nx,Ncolor] = size(I);
% Aspect ratio of the image
ratio = Nx/Ny;
% Definition of resolution distribution VAM and optical magnification m
VAM = [];
m = [];
%% Visual acuity of Human eye sampled with 0.1-degree interval
for i=1:1:1000
    VAM(i) = 2.3/(2.3+i/10);
    m(i) = 1/VAM(i);
end

% The parameter determined process of the statically foveated scheme.
eta = 0.3;
theta_c1 = 10;
theta_c2 = 30;
theta_max = 80;

sigm = (theta_c2-theta_c1)/sqrt(-2*log(eta));
theta_ih = theta_c2+2.3*(1-1/eta);
e1 = theta_c2; e2 = theta_c2+20; e3 = theta_c2+40; e4 = theta_max;
a1 = 2.3/(2.3+(e1-theta_ih));
a2 = -1/sigm^2*(e1-theta_c1(1))*exp(-(e1-theta_c1(1))^2/(2*sigm^2));
a3 = 2.3/(2.3+(e2-theta_ih));
a4 = 2.3/(2.3+(e3-theta_ih));
a5 = 2.3/(2.3+(e4-theta_ih));

```

```

A = [1,1/e1,1/(e1^2),1/(e1^3),1/(e1^4);0,-1/(e1^2),-2/(e1^3),-3/(e1^4),-
4/(e1^5);1,1/e2,1/(e2^2),1/(e2^3),1/(e2^4);1,1/e3,1/(e3^2),1/(e3^3),1/(e3^4);1,1/e4,1
/(e4^2),1/(e4^3),1/(e4^4)];
B = [a1;a2;a3;a4;a5];
X = inv(A)*B;
%%% Resolution distribution function of foveated display sampled with 0.1-degree
%%%interval.
for i=1:1:100
    VAM(i) = 1;
end
for i=101:1:301
    VAM(i) = exp(-0.003*(i/10-10).^2);
end
for i=301:1:801
    VAM(i) =X(1)+X(2)/(i/10)+X(3)/((i/10)^2)+X(4)/((i/10)^3)+X(5)/((i/10)^4);
end

% Pixel number per 0.1 degrees
angle_desity = Nx/800;
% Applied Gaussian-type filter into original image
for i = 1:1:Nx
    for j = 1:1:Ny
        for m1 = 1:1:Ncolor
% Determined the responding resolution distribution at the picture's position of
[I,j,m1]
            index = round(sqrt((i/angle_desity-
300*Nx/sqrt(Nx^2+Ny^2))^2+(j/angle_desity-300*Ny/sqrt(Nx^2+Ny^2))^2))+1;
% Determined the convolution area based on the magnification
            a = 2*floor(m(index));
% Definition of foveated image' value for target pixel
            Reim(j,i,m1) = 0;
% Definition of weight matrix of the convolution for target pixel
            WeightMatrix = zeros();
% Calculation of weight matrix of the convolution for target pixel

```

```

    if m(index)==1
        Reim(j,i,m1) = I(j,i,m1);
    end
    if m(index) > 1
        for x = 1:1:a
            for y = 1:1:a
                WeightMatrix(x,y)=exp(-((x-(a)/2)^2+(y-
(a)/2)^2)/(2*(m(index)/2.355)^2))/(2*pi*(m(index)/2.355)^2);
            end
        end
        WeightMatrix = WeightMatrix./sum(sum(WeightMatrix));
% Do convolution for target pixel and considering edge position of the picture
        for x = 1:a
            for y = 1:a
% When the target pixel located at the left-top side
                if j+x-(a)/2 <= 0 && i+(y-(a)/2) <= 0
                    Reim(j,i,m1) = Reim(j,i,m1)+I(Ny+j+x-(a)/2,Nx+i+(y-
(a)/2),m1)*WeightMatrix(x,y);
                End
% When the target pixel located at the right-top side
                if j+x-(a)/2 <= 0 && i+(y-(a)/2) > Nx
                    Reim(j,i,m1) = Reim(j,i,m1)+I(Ny+j+x-(a)/2,-Nx+i+(y-
(a)/2),m1)*WeightMatrix(x,y);
                End
% When the target pixel located at the left-bottom side
                if j+x-(a)/2 > Ny && i+(y-(a)/2) <= 0
                    Reim(j,i,m1) = Reim(j,i,m1)+I(-Ny+j+x-(a)/2,Nx+i+(y-
(a)/2),m1)*WeightMatrix(x,y);
                End
% When the target pixel located at the right-bottom side
                if j+x-(a)/2 > Ny && i+(y-(a)/2) > Nx
                    Reim(j,i,m1) = Reim(j,i,m1)+I(-Ny+j+x-(a)/2,-Nx+i+(y-
(a)/2),m1)*WeightMatrix(x,y);
                end
            end
        end
    end

```


APPENDIX D: CODEV MACRO USED FOR OPTIMIZATION OF THE
FOVEATED OST-HMD

```
!!!!!!!!!!!!!!!!!!!! OPTIMIZATION MACRO for FREEFORM PRISMS
```

```
AUT
```

```
!!!!!!!!!!!!!!!!!!!! Prism Structure control
```

```
@Ypa1_Ypa == (Y S6 F21 W2 G2 R3 Z1)-(Y S5 F21 W2 G2 R3 Z1)
```

```
@Ypa2_Ypa == (Y S7 F21 W2 G2 R3 Z1)-(Y S6 F21 W2 G2 R3 Z1)
```

```
@Zpa1_Zpa == (Z S6 F21 W2 G2 R3 Z1)-(Z S5 F21 W2 G2 R3 Z1)
```

```
@Ypb1_Ypb == (Y S8 F21 W2 G2 R3 Z1)-(Y S6 F1 W2 G2 R2 Z2)
```

```
@Ypb1_Ypb_edge_field == (Y S8 F21 W2 G2 R3 Z2)-(Y S6 F14 W2 G2 R2 Z2)
```

```
@Zpb1_Zpb == (Z S8 F21 W2 G2 R3 Z1)-(Z S6 F1 W2 G2 R2 Z2)
```

```
@Ypc1_Ypc == (Y S7 F1 W2 G2 R2 Z2)-(Y S8 F1 W2 G2 R2 Z2)
```

```
@Zpc1_Zpc == (Z S7 F1 W2 G2 R3 Z2)-(Z S8 F1 W2 G2 R2 Z2)
```

```
@thick == (Z S6 F5 W2 G2 R2 Z2)-(Z S7 F1 W2 G2 R2 Z2)
```

```
!!!!!!!!!!!!!!!!!!!! Display size control
```

```
@SizeX == ABSF((X SI F10 W2 R1 Z2)-(X SI F25 W2 R1 Z1))
```

```
@SizeY == ABSF((Y SI F1 W2 R1 Z2)-(Y SI F25 W2 R1 Z1))
```

```
!!!!!!!!!!!!!!!!!!!! resolution distribution control
```

```
!!!!!!!!!!!!!!!!!!!! 4-degree field resolution distribution control
```

```
@Z1_f1 == ABSF(SQRT(((X SI F1 W2 R1 Z1)-(X SI F25 W2 R1 Z1))**2+((Y SI F1 W2 R1 Z1)-(Y SI F25 W2 R1 Z1))**2))
```

```
@Z1_f2 == ABSF(SQRT(((X SI F2 W2 R1 Z1)-(X SI F25 W2 R1 Z1))**2+((Y SI F2 W2 R1 Z1)-(Y SI F25 W2 R1 Z1))**2))
```

```
@Z1_f3 == ABSF(SQRT(((X SI F3 W2 R1 Z1)-(X SI F25 W2 R1 Z1))**2+((Y SI F3 W2 R1 Z1)-(Y SI F25 W2 R1 Z1))**2))
```

```
@Z1_f4 == ABSF(SQRT(((X SI F4 W2 R1 Z1)-(X SI F25 W2 R1 Z1))**2+((Y SI F4 W2 R1 Z1)-(Y SI F25 W2 R1 Z1))**2))
```

```
@Z1_f5 == ABSF(SQRT(((X SI F5 W2 R1 Z1)-(X SI F25 W2 R1 Z1))**2+((Y SI F5 W2 R1 Z1)-(Y SI F25 W2 R1 Z1))**2))
```

```
@Z1_f6 == ABSF(SQRT(((X SI F6 W2 R1 Z1)-(X SI F25 W2 R1 Z1))**2+((Y SI F6 W2 R1 Z1)-(Y SI F25 W2 R1 Z1))**2))
```

```
@Z1_f7 == ABSF(SQRT(((X SI F7 W2 R1 Z1)-(X SI F25 W2 R1 Z1))**2+((Y SI F7 W2 R1 Z1)-(Y SI F25 W2 R1 Z1))**2))
```

```
!!!!!!!!!!!!!!!!!!!! Average of 4-degree field resolution distribution
```

```
@avr_Z1 == ABSF((@Z1_f1+@Z1_f2+@Z1_f3+@Z1_f4+@Z1_f5+@Z1_f6+@Z1_f7)/7)
```

```
!!!!!!!!!!!!!!!!!!!! Control the value of Average of resolution distribution
```

```

@avr_Z1_dis == ABSF((@Z1_f1+@Z1_f2+@Z1_f3+@Z1_f4+@Z1_f5+@Z1_f6+@Z1_f7)/7-2.28)
@Variance_4 == ((@Z1_f1-@avr_Z1)**2+(@Z1_f2-@avr_Z1)**2+(@Z1_f3-@avr_Z1)**2+(@Z1_f4-
@avr_Z1)**2+(@Z1_f5-@avr_Z1)**2+(@Z1_f6-@avr_Z1)**2+(@Z1_f7-@avr_Z1)**2)/7

!!!!!!!!!!!!!!!!!!!! 8-degree field resolution distribution control
@Z1_f8 == ABSF(SQRT(((X SI F8 W2 R1 Z1)-(X SI F25 W2 R1 Z1))**2+((Y SI F8 W2 R1 Z1)-
(Y SI F25 W2 R1 Z1))**2))
@Z1_f9 == ABSF(SQRT(((X SI F9 W2 R1 Z1)-(X SI F25 W2 R1 Z1))**2+((Y SI F9 W2 R1 Z1)-
(Y SI F25 W2 R1 Z1))**2))
@Z1_f10 == ABSF(SQRT(((X SI F10 W2 R1 Z1)-(X SI F25 W2 R1 Z1))**2+((Y SI F10 W2 R1
Z1)-(Y SI F25 W2 R1 Z1))**2))
@Z1_f11 == ABSF(SQRT(((X SI F11 W2 R1 Z1)-(X SI F25 W2 R1 Z1))**2+((Y SI F11 W2 R1
Z1)-(Y SI F25 W2 R1 Z1))**2))
@Z1_f12 == ABSF(SQRT(((X SI F12 W2 R1 Z1)-(X SI F25 W2 R1 Z1))**2+((Y SI F12 W2 R1
Z1)-(Y SI F25 W2 R1 Z1))**2))
@Z1_f13 == ABSF(SQRT(((X SI F13 W2 R1 Z1)-(X SI F25 W2 R1 Z1))**2+((Y SI F13 W2 R1
Z1)-(Y SI F25 W2 R1 Z1))**2))
@Z1_f14 == ABSF(SQRT(((X SI F14 W2 R1 Z1)-(X SI F25 W2 R1 Z1))**2+((Y SI F14 W2 R1
Z1)-(Y SI F25 W2 R1 Z1))**2))
@avr_Z1_2 == ABSF((@Z1_f8+@Z1_f9+@Z1_f10+@Z1_f11+@Z1_f12+@Z1_f13+@Z1_f14)/7)
@avr_Z1_2_dis == ABSF((@Z1_f8+@Z1_f9+@Z1_f10+@Z1_f11+@Z1_f12+@Z1_f13+@Z1_f14)/7-
4.56)
@Variance_8 == 100*((@Z1_f8-@avr_Z1_2)**2+(@Z1_f9-@avr_Z1_2)**2+(@Z1_f10-
@avr_Z1_2)**2+(@Z1_f11-@avr_Z1_2)**2+(@Z1_f12-@avr_Z1_2)**2+(@Z1_f13-
@avr_Z1_2)**2+(@Z1_f14-@avr_Z1_2)**2)/7

!!!!!!!!!!!!!!!!!!!! 15-degree field resolution distribution control
@Z1_f20 == ABSF(SQRT(((X SI F20 W2 R1 Z1)-(X SI F25 W2 R1 Z1))**2+((Y SI F20 W2 R1
Z1)-(Y SI F25 W2 R1 Z1))**2))
@Z1_f21 == ABSF(SQRT(((X SI F21 W2 R1 Z1)-(X SI F25 W2 R1 Z1))**2+((Y SI F21 W2 R1
Z1)-(Y SI F25 W2 R1 Z1))**2))
@Z1_f22 == ABSF(SQRT(((X SI F22 W2 R1 Z1)-(X SI F25 W2 R1 Z1))**2+((Y SI F22 W2 R1
Z1)-(Y SI F25 W2 R1 Z1))**2))

```

```
@Z1_f23 == ABSF(SQRT(((X SI F23 W2 R1 Z1)-(X SI F25 W2 R1 Z1))**2+((Y SI F23 W2 R1 Z1)-(Y SI F25 W2 R1 Z1))**2))
```

```
@Z1_f24 == ABSF(SQRT(((X SI F24 W2 R1 Z1)-(X SI F25 W2 R1 Z1))**2+((Y SI F24 W2 R1 Z1)-(Y SI F25 W2 R1 Z1))**2))
```

```
@avr_Z1_3 == ABSF((@Z1_f20+@Z1_f21+@Z1_f22+@Z1_f23+@Z1_f24)/5)
```

```
@avr_Z1_3_dis == ABSF((@Z1_f20+@Z1_f21+@Z1_f22+@Z1_f23+@Z1_f24)/5-11.31/2*1.5)
```

```
@Variance_16 == 100*((@Z1_f20-@avr_Z1_3)**2+(@Z1_f21-@avr_Z1_3)**2+(@Z1_f22-@avr_Z1_3)**2+(@Z1_f23-@avr_Z1_3)**2+(@Z1_f24-@avr_Z1_3)**2)/5
```

```
!!!!!!!!!!!!!!!!!!!! 20-degree field resolution distribution control
```

```
@Z2_f1 == ABSF(SQRT(((X SI F1 W2 R1 Z2)-(X SI F25 W2 R1 Z1))**2+((Y SI F1 W2 R1 Z2)-(Y SI F25 W2 R1 Z1))**2))
```

```
@Z2_f2 == ABSF(SQRT(((X SI F2 W2 R1 Z2)-(X SI F25 W2 R1 Z1))**2+((Y SI F2 W2 R1 Z2)-(Y SI F25 W2 R1 Z1))**2))
```

```
@Z2_f3 == ABSF(SQRT(((X SI F3 W2 R1 Z2)-(X SI F25 W2 R1 Z1))**2+((Y SI F3 W2 R1 Z2)-(Y SI F25 W2 R1 Z1))**2))
```

```
@Z2_f4 == ABSF(SQRT(((X SI F4 W2 R1 Z2)-(X SI F25 W2 R1 Z1))**2+((Y SI F4 W2 R1 Z2)-(Y SI F25 W2 R1 Z1))**2))
```

```
@avr_Z2_1 == ABSF((@Z2_f1+@Z2_f2+@Z2_f3+@Z2_f4)/4)
```

```
@avr_Z2_1_dis == ABSF((@Z2_f1+@Z2_f2+@Z2_f3+@Z2_f4)/4-16.9/2*1.5)
```

```
@Variance_20 == 100*((@Z2_f1-@avr_Z2_1)**2+(@Z2_f2-@avr_Z2_1)**2+(@Z2_f3-@avr_Z2_1)**2+(@Z2_f4-@avr_Z2_1)**2)/4
```

```
!!!!!!!!!!!!!!!!!!!! 25-degree field resolution distribution control
```

```
@Z2_f5 == ABSF(SQRT(((X SI F5 W2 R1 Z2)-(X SI F25 W2 R1 Z1))**2+((Y SI F5 W2 R1 Z2)-(Y SI F25 W2 R1 Z1))**2))
```

```
@Z2_f6 == ABSF(SQRT(((X SI F6 W2 R1 Z2)-(X SI F25 W2 R1 Z1))**2+((Y SI F6 W2 R1 Z2)-(Y SI F25 W2 R1 Z1))**2))
```

```
@Z2_f7 == ABSF(SQRT(((X SI F7 W2 R1 Z2)-(X SI F25 W2 R1 Z1))**2+((Y SI F7 W2 R1 Z2)-(Y SI F25 W2 R1 Z1))**2))
```

```
@Z2_f8 == ABSF(SQRT(((X SI F8 W2 R1 Z2)-(X SI F25 W2 R1 Z1))**2+((Y SI F8 W2 R1 Z2)-(Y SI F25 W2 R1 Z1))**2))
```

```
@avr_Z2_2 == ABSF((@Z2_f5+@Z2_f6+@Z2_f7+@Z2_f8)/4)
```

```
@avr_Z2_2_dis == ABSF((@Z2_f5+@Z2_f6+@Z2_f7+@Z2_f8)/4-18.4/2*1.5)
```

```

@Variance_25 == 100*((@Z2_f5-@avr_Z2_2)**2+(@Z2_f6-@avr_Z2_2)**2+(@Z2_f7-
@avr_Z2_2)**2+(@Z2_f8-@avr_Z2_2)**2)/4

!!!!!!!!!!!!!!!!!!!! 30-degree field resolution distribution control
@Z2_f9 == ABSF(SQRT(((X SI F9 W2 R1 Z2)-(X SI F25 W2 R1 Z1))**2+((Y SI F9 W2 R1 Z2)-
(Y SI F25 W2 R1 Z1))**2))
@Z2_f10 == ABSF(SQRT(((X SI F10 W2 R1 Z2)-(X SI F25 W2 R1 Z1))**2+((Y SI F10 W2 R1
Z2)-(Y SI F25 W2 R1 Z1))**2))
@Z2_f11 == ABSF(SQRT(((X SI F11 W2 R1 Z2)-(X SI F25 W2 R1 Z1))**2+((Y SI F11 W2 R1
Z2)-(Y SI F25 W2 R1 Z1))**2))
@Z2_f12 == ABSF(SQRT(((X SI F12 W2 R1 Z2)-(X SI F25 W2 R1 Z1))**2+((Y SI F12 W2 R1
Z2)-(Y SI F25 W2 R1 Z1))**2))
@avr_Z2_2 == ABSF((@Z2_f9+@Z2_f10+@Z2_f11+@Z2_f12)/4)
@avr_Z2_2_dis == ABSF((@Z2_f9+@Z2_f10+@Z2_f11+@Z2_f12)/4-18.4/2*1.5)
@Variance_25 == 100*((@Z2_f9-@avr_Z2_2)**2+(@Z2_f10-@avr_Z2_2)**2+(@Z2_f11-
@avr_Z2_2)**2+(@Z2_f12-@avr_Z2_2)**2)/4

!!!!!!!!!!!!!!!!!!!! keystone control through the difference of the chief ray height
!!!!!!!!!!!!!!!!!!!! along Y-axis for center field and x-edge field
@DIS_ANGLE == (Y SI F10 W2 R1 Z2)-(Y SI F25 W2 R1 Z1)
!!!!!!!!!!!!!!!!!!!! keystone control through control the distortion gird shape
@keystone_control == (X SI F22 W2 R1 Z2)-(X SI F10 W2 R1 Z2)
@keystone_control2 == (Y SI F1 W2 R1 Z2)-(Y SI F21 W2 R1 Z2)
!!!!!!!!!!!!!!!!!!!! TIR Condition control
AOI R2 S7 W2 F1 Z2 > 41
AOI R2 S7 W2 F21 Z1 > 41
AOI R2 S7 W2 F21 Z2 > 41
AOI R3 S7 W2 F1 Z2 > 41
AOI R3 S7 W2 F21 Z1 > 41
AOI R3 S7 W2 F21 Z2 > 41
!!!!!!!!!!!!!!!!!!!! Surface conic value
K S5 Z1 > -99
K S6 Z1 > -99
K S8 Z1 > -99

```

```

K S5 Z1 < 99
K S6 Z1 < 99
K S8 Z1 < 99
!!!!!!!!!!!!!!!!!!!! Prism structure control
@Zpa1_Zpa > 0.0
!@Zpa1_Zpa <8
@Ypb1_Ypb > 1
!@Ypb1_Ypb_edge_field > 1
@Zpb1_Zpb < -0.5
@Zpb1_Zpb > -5.0
@Ypc1_Ypc > -5.0
@Ypc1_Ypc < -0.2
@Zpc1_Zpc > -6.0
@Zpc1_Zpc < 2.0
OP R2 S7..8 W2 F21 Z2 > 0.5
OP R3 S5..6 W2 F21 Z1 > 0.1
OP R3 S5..6 W2 F22 Z2 > 0.1
!!!!!!!!!!!!!!!!!!!! Prism maximum thickness
@thick < 26
!!!!!!!!!!!!!!!!!!!! clearance between display and prism
OP R1 S8..9 W2 F1 Z2 > 2
OP R1 S8..9 W2 F21 Z2 > 2
OP R1 S8..9 W2 F10 Z2 > 2
OP R1 S8..9 W2 F21 Z1 > 2
OP R1 S8..9 W2 F8 Z1 > 2
OP R1 S8..9 W2 F9 Z1 > 2
OP R1 S8..9 W2 F1 Z1 > 2
OP R1 S8..9 W2 F2 Z1 > 2
OP R1 S8..9 W2 F15 Z1 > 2
OP R1 S8..9 W2 F16 Z1 > 2
OP R1 S8..9 W2 F25 Z1 > 2
!!!!!!!!!!!!!!!!!!!! eye clearance control
Z S5 F25 W2 G2 R1 Z1 > 15
Z S7 F1 W2 G2 R2 Z2 > 15

```

```

Z S5 F21 W2 G2 R3 Z2 > 15
!!!!!!!!!!!!!!!!!!!! resolution distribution and symmetry control for three regions
!!!!!!!!!!!!!!!!!!!! 4-degree
@avr_Z1_dis < 0.019
@Variance_4 < 1
!!!!!!!!!!!!!!!!!!!! 15-degree
@avr_Z1_3_dis < 0.019*8
@Variance_15 < 5
!!!!!!!!!!!!!!!!!!!! 25-degree
@avr_Z2_2_dis < 0.019*50
@Variance_25 < 6
!!!!!!!!!!!!!!!!!!!! Display size control and keystone control
@SizeX < 18.5
DSP @SizeY
@DIS_ANGLE < 0.5
@DIS_ANGLE > -0.5
@keystone_control < 0
@keystone_control2 > 0.1
!!!!!!!!!!!!!!!!!!!! Global optimization
GS 2
TAR 0 700
MNC 2
IMP 0.05
DRA S1..12 YES!
EFP ALL Y
!!!!!!!!!!!!!!!!!!!! local optimization
!MNC 2
!IMP 0.05
!DRA S1..12 YES
!EFP ALL Y

GO

```

APPENDIX E: SURFACES' GLOBAL COORDINATE DATA AND
PARAMETERS FOR FOVEATED FREEFORM OST-HMD

Surface global coordinate data for main freeform prism and display panel

Definition of the local surface references in the global coordinate system OXYZ.				
	Origin of surface reference			Orientation of the surface
	X (mm)	Y (mm)	Z (mm)	Rotation about X-axis θ (°)
Surface 5 & 7				
Origin: $O_1(x_1, y_1, z_1)$	0	-8.584	27.249	40.535
Orientation: θ_1				
Surface 6				
Origin: $O_2(x_2, y_2, z_2)$	0	-26.361	68.442	-29.208
Orientation: θ_2				
Surface 8				
Origin: $O_3(x_3, y_3, z_3)$	0	22.410	-7.221	81.437
Orientation: θ_3				
Microdisplay				
Origin: $O_{Im}(x_{Im}, y_{Im}, z_{Im})$	0	32.06227	34.71714	77.471
Orientation: θ_{Im}				

The parameters of three freeform surface with Zernike surface type

Coefficients	comment	Surface $S_2, S_3, \& S'_3$	Surface $S_4, \& S'_4$	Surface S_5
Y Radius	R	-117.4370384731	-85.2090530247876	-115.234511667086
C69	Normalization Radius	100	100	100
C1	k	-1.36515814490312	1.2171746688979	1.99346959613328
C2	1 (piston)	0	0	0
C3	$R\cos\theta$	0	0	0
C4	$R\sin\theta$	0	0	0
C5	$R^2\cos(2\theta)$	-16.5774862327263	39.8807446839406	37.2269452450524
C6	$2R^2-1$	-11.5078328629417	69.6377858885028	13.0873317915867
C7	$R^2\sin(2\theta)$	0	0	0
C8	$R^3\cos(3\theta)$	0	0	0
C9	$(3R^3-2R)\cos\theta$	0	0	0
C10	$(3R^3-2R)\sin\theta$	-29.5209693142432	9.37018625756946	52.571231092239
C11	$R^3\sin(3\theta)$	64.4426067748386	-13.3880989186106	-82.3370466962103
C12	$R^4\cos(4\theta)$	-30.14846152253	29.8005694801582	77.2709362219925
C13	$(4R^4-3R^2)\cos(2\theta)$	-4.55206191181011	7.07014379837453	18.9324289910254
C14	$6R^4-6R^2+1$	-5.87157634342453	46.8556156661628	-21.3334192151897
C15	$(4R^4-3R^2)\sin(2\theta)$	0	0	0
C16	$R^4\sin(4\theta)$	0	0	0
C17	$R^5\cos(5\theta)$	0	0	0
C18	$(5R^5-4R^3)\cos(3\theta)$	0	0	0
C19	$(10R^5-12R^3+3R)\cos\theta$	0	0	0
C20	$(10R^5-12R^3+3R)\sin\theta$	-9.47229517570933	-0.20779991451017	-25.289876352918
C21	$(5R^5-4R^3)\sin(3\theta)$	14.0539904483067	-2.01820056836617	-64.5917818221494
C22	$R^5\sin(5\theta)$	-28.4815624578547	-29.3314703571434	-92
C23	$R^6\cos(6\theta)$	21.4339942207105	-34.2275921880354	92
C24	$(6R^6-5R^4)\cos(4\theta)$	-8.42661690375713	6.24328406715904	40.6148950716777
C25	$(15R^6-20R^4+6R^2)\cos(2\theta)$	0.053736942498536	-2.05480336882794	35.3998896025369
C26	$20R^6-30R^4+12R^2-1$	0.030145919028660	10.7136736713839	-16.8373303370225
C27	$(15R^6-20R^4+6R^2)\sin(2\theta)$	0	0	0
C28	$(6R^6-5R^4)\sin(4\theta)$	0	0	0
C29	$R^6\sin(6\theta)$	0	0	0